

The University of Jordan

Authorization Form

I, *Aziz A. Al-Muhktaseb* , authorize the University of Jordan to supply copies of my Thesis/ Dissertation to libraries or establishments or individuals on request, according to the University of Jordan regulations.

Signature:



Date: *16th, Dec, 2010*

التاريخ: / /

نموذج رقم (16)
اقرار والتزام بالمعايير الأخلاقية والأمانة العلمية
وقوانين الجامعة الأردنية وأنظمتها وتعليماتها لطلبة
الدكتوراة

أنا الطالب: عزيز عبد الحافظ شاهين المحتسب
الرقم الجامعي: (9050121)
تخصص: الميكانيك
الكلية: الهندسة

عنوان الأطروحة:

Numerical Simulation and Experimental Investigation of Shear
Driven Micropumps for Biomedical Applications.

اعلن بأبني قد التزمت بقوانين الجامعة الأردنية وأنظمتها وتعليماتها وقراراتها السارية
المفعول المتعلقة بأعداد أطروحات الدكتوراه عندما قمت شخصياً بأعداد أطروحتي وذلك بما
ينسجم مع الأمانة العلمية وكافة المعايير الأخلاقية المتعارف عليها في كتابة الأطروحات
العلمية. كما أنني أعلن بأن أطروحتي هذه غير منقولة أو مستلة من أطاريح أو كتب أو
أبحاث أو أي منشورات علمية تم نشرها أو تخزينها في أي وسيلة اعلامية، وتأسيساً على
ما تقدم فإني أتحمل المسؤولية بأنواعها كافة فيما لو تبين غير ذلك بما فيه حق مجلس
العمداء في الجامعة الأردنية بالغاء قرار منحي الدرجة العلمية التي حصلت عليها وسحب
شهادة التخرج مني بعد صدورها دون أن يكون لي أي حق في التظلم أو الاعتراض أو الطعن
بأي صورة كانت في القرار الصادر عن مجلس العمداء بهذا الصدد.

التاريخ: 2010/12 / 16

توقيع الطالب:

تعتمد كلية الدراسات العليا
هذه النسخة من الرسالة
التوقيع: التاريخ: 2010/12/16

**NUMERICAL SIMULATION AND EXPERIMENTAL
INVESTIGATION OF SHEAR DRIVEN MICROPUMPS FOR
BIOMEDICAL APPLICATIONS**

By
Aziz Abdulhafez Shaheen Al-Muhtaseb

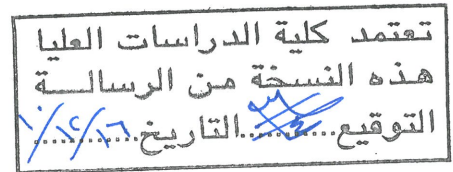
Supervisor
Dr. Ahmed Al-Salaymeh

Co-Supervisor
Dr. Ala'aldeen Al-Halhoul

**This Dissertation was submitted in Partial Fulfillment of the Requirements for the
Doctor of Philosophy Degree in Mechanical Engineering**

Faculty of Graduate Studies

The University of Jordan



Dec, 2010

COMMITTEE DECISION

This Dissertation (**Numerical Simulation and experimental investigation of shear driven micropumps for biomedical applications**) was successfully defended and approved on

Examination Committee

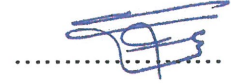
Signature

Dr. Ahmed Al-Salaymeh



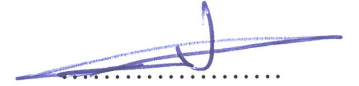
Associate Prof. of Mechanical Engineering

Dr. Ala'aldeen Al-Halhouli



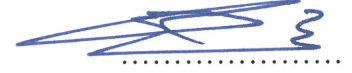
Associate Researcher of Microtechnology

Prof. Ahmad A. Al-Qaisia



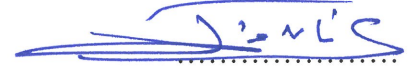
Prof. of Mechanical Engineering

Prof. Mohammed Ahmed Hamdan



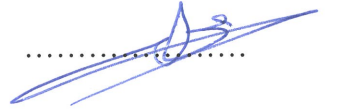
Prof. of Mechanical Engineering

Dr. Adnan W. Jaradat



Associate Prof. of Mechanical Engineering

Dr. Mohmmad Sami Al-Ashhab



Associate Prof. of Mechanical Engineering (External Examiner)

تعتمد كلية الدراسات العليا
هذه النسخة من الرسالة
التوقيع: ١٦/١٤٠٤
١٤٠٤

DEDICATION

To my devoted parents who have been saving no effort to help, encourage and pray for me day and night without getting bored or even feel tired of me, to my brothers and sisters. To my current fiancé and future wife “Alaa”. To my supervisor and co-advisor. To my work colleagues. And to my friends I dedicate this work.

Acknowledgments

First of all, all praise and thanks are due to Almighty Allah, subhana-wa-taala, the most Merciful; the most Benevolent, for bestowing me with the health, knowledge, opportunity, courage and patience to complete this work.

I would like to express my deep gratitude and appreciation to Prof. Ahmed Al-Salaymeh, Dr. Ala'aldeen Al-Halhouli and Prof. Stephanus Büttgenbach for their endless help, support, encouragement, hospitality especially when I was in Germany doing the experimental part of my dissertation and their valuable guidance and advice.

Also, I would also like to thank all of the ladies and gentlemen in the Institute for Microtechnology, Braunschweig for their friendship and amazing time I spent with them.

All thanks are extended to the staff in the Mechanical Engineering Department at the University of Jordan for their support and help.

I also wish to thank the German Academic Exchange Service (DAAD) for their invaluable scholarship they had offered me.

To my work colleagues who has supported me and helped me during my Ph.D. study.

Finally, I highly appreciate the support and encouragement of my parents, parents in law, my brothers and sisters, my fiancé "Alaa", and to all of friends, of my friends who always kept supporting and encouraging me.

Table of Content

Committee Decision	ii
Dedication	iii
Acknowledgements	iv
Table of Contents	v
List of Tables	ix
List of Figures	xi
Nomenclature	xvii
Abstract	xix

Chapter 1

Introduction and Objectives

1.1 Introduction.....	1
1.2 Dissertation Objective	2
1.3 Dissertation Outline.....	5

Chapter 2

Literature Survey

2.1 Micropumps	7
2.1.1 Eccentric micropumps	7
2.1.2 Single and double disk micropumps	12
2.1.3 Spiral Channel micropumps	14
2.2 Rheological investigation of blood as a non-Newtonian fluid	16

Chapter 3

Theoretical and Numerical Backgrounds

3.1	Introduction	21
3.2	Micropumps	21
3.3	Blood properties	23
3.4	Governing equations	25
3.5	Non-Newtonian fluids	27
3.5.1	Non-Newtonian power law model	28
3.5.2	The Carreau model	29
3.5.3	The Careau Yasuda model	31
3.5.4	Herschel Bulkley model for Bingham Plastics	33
3.5.5	Cross model	34
3.6	Laminar, transitional and turbulent fluid flow	34
3.7	Compressible and Incompressible fluid flows	35
3.8	Fully developed flow and entrance length	36
3.9	Slip and no slip boundary conditions	36
3.10	Friction factor	37
3.11	CFD simulation methods	38
3.12	Introduction to FLUENT package	40
3.13	SIMPLE algorithm	41
3.14	The staggered grid	43
3.15	Grid dependency and numerical stability	44
3.16	Residuals reported by FLUENT	46

Chapter 4

Mathematical Modeling

4.1	Introduction	48
4.2	Continuity and Navier Stokes equation	49
4.3	Mathematical formulation	55
4.3.1	Single disk micropumps	55
4.3.2	Double disk micropumps	57
4.3.3	Spiral channel micropumps	58

Chapter 5

Experimental Investigations, Operations and Results: Spiral

Micropump

5.1	Introduction	60
5.2	Spiral micropump manufacturing process (SU-8 UV Lithography)	60
5.3	Spiral micropump configuration and operation	62
5.4	Spiral micropump setup and testing	63
5.5	Blood mimicking fluid	69
5.6	Flow rate experimental results.....	70
5.7	Experimental uncertainty analysis.....	77

Chapter 6

Results and Discussion

6.1	Introduction	80
6.2	Validation of the present work, grid optimization and Convergence criteria	80
6.3	Effect of Power law index, n , on the fluid flow inside the micropumps	89
6.4	Effect of aspect ratio on the flow performance of the single disk, double	94

	disk and spiral channel micropumps	
6.5	Single disk, double disk and spiral channel micropumps performance curves	106
6.6	Shear stress analysis	112

Chapter 7

Conclusions and recommendations

7.1	Conclusions	116
7.2	Recommendations	120
	References	121
	Appendix	126
	Abstract in Arabic	132

List of Tables

Table 1.1	Summary of the micropumps investigations performed in this study ..	4
Table 2.1	The modeling parameters and the performance relations of the approximate spiral pump model	16
Table 3.1	Non-Newtonian Power-Law model parameters	29
Table 3.2	Carreau model parameters	30
Table 3.3	Carreau-Yasuda model parameters	32
Table 3.4	Flow regimes and their flow model based on Knudsen number	37
Table 5.1	The constituents of the used blood mimicking fluid	69
Table 5.2	The dimensions of the two tested spiral channel pumps	70
Table 5.3	Measured mass flow rates with their uncertainties .vs. the pump rotational speed	79
Table 5.4	Measured mass flow rates with their uncertainties .vs. the outlet head for the distilled water as a working fluid	79
Table 5.5	Measured mass flow rates with their uncertainties .vs. the outlet head for the blood mimicking fluid	79
Table 6.1	Effect of channel aspect ratio on drag and pressure shape factors ...	81
Table 6.2	A Comparison of both mathematical and numerical Newtonian results to the analytical solution [8] at $\alpha=1$, $m=3.5 \times 10^{-3}$ [Pa.Sec], $P_o=0.0$ [Pa], $n=1$ and $\tau_o=0.0$ [Pa]	82
Table 6.3	Optimum step size for each aspect ratio used with the Matlab code	86

	obtaining the non-dimensional solution of the current problem	
Table 6.4	The average dimensionless axial velocity for the three types of the micropumps at different power law index values	93
Table 6.5	Herschel Bulkley blood constants	94
Table 6.6	Numerical values of the dimensionless mass flow rates .vs. generalized reduced Reynolds Euler number	111
Table 6.7	Wall shear stress for the currently studied micropumps at different aspect ratios, with the time needed for the fluid particle to travel through the micropump	112

List of Figures

Figure 2.1	The principle of the eccentric pump is based on generating axial fluid motion in micro channel through the rotation of a cylinder placed asymmetrically in a viscous fluid medium	8
Figure 2.2	An illustration of the (a.) single and (b.) double disk viscous micropumps	13
Figure 2.3	A spiral-channel viscous pump components	15
Figure 3.1	Classification of rotating viscous micropumps and a survey of references	23
Figure 3.2	Variation of Viscosity with Rate of Strain According to the Non-Newtonian Power	29
Figure 3.3	Variation of Viscosity with Rate of Strain According to the Carreau Model	31
Figure 3.4	Variation of Viscosity with Rate of Strain According to the Carreau-Yasuda Model	32
Figure 3.5	Shear stress (τ) varies with shear rate ($\dot{\gamma}$) for the Herschel-Bulkley model	34
Figure 3.6	Schematic diagram of the sequence of operations of the SIMPLE algorithm.....	43
Figure 4.1	The considered geometry for the present work in the unfolding approximation.....	49

Figure 5.1	Fabrication procedure of SU-8 using UV depth lithography	62
Figure 5.2	The final shape of the spiral channel silicon disk	62
Figure 5.3	The used variable power source in the present experiment	64
Figure 5.4	The used analogue oscilloscope in the present experiment	64
Figure 5.5	The used digital scale in the present experiment	65
Figure 5.6	Setup adopted for the current spiral micropump	67
Figure 5.7	Comparison between the analytical and experimental results for distilled water flow in the first spiral channel pump	71
Figure 5.8	Comparison between the analytical and experimental results for second spiral channel pump	71
Figure 5.9	Pump water flow rate .vs. rotational speed of first spiral micropump ..	72
Figure 5.10	Pump head vs. water mass flow rate for the first spiral micropump ...	73
Figure 5.11	Pump water flow rate .vs. rotational speed of second spiral micropump	74
Figure 5.12	Pump head vs. water mass flow rate for the second spiral micropump	74
Figure 5.13	Mass flow rate .vs. rotational speed of the micropump for the blood mimicking fluid operated in the first spiral micropump	75
Figure 5.14	Pump head .vs. mass flow rate of the micropump for the blood mimicking fluid operated in the first spiral micropump	76
Figure 5.15	Mass flow rate .vs. rotational speed of the micropump for the blood mimicking fluid operated in the second spiral micropump	76
Figure 5.16	Pump head .vs. mass flow rate of the micropump for the blood mimicking fluid operated in the second spiral micropump	77

Figure 6.1	Mass flow rate .vs. outlet pressure for single disk micropump with Newtonian blood properties. $\alpha=1.0$, $m=3.5 \times 10^{-3}$ Ps.Sec, $n=1$ and $\tau_o=0.0$ [Pa]	83
Figure 6.2	Mass flow rate .vs. outlet pressure for double disk micropump with Newtonian blood properties. $\alpha=1.0$, $m=3.5 \times 10^{-3}$ Ps.Sec, $n=1$ and $\tau_o=0.0$ [Pa].....	83
Figure 6.3	Mass flow rate .vs. outlet pressure for spiral micropump with Newtonian blood properties. $\alpha=1.0$, $m=3.5 \times 10^{-3}$ Ps.Sec, $n=1$ and $\tau_o=0.0$ [Pa]	84
Figure 6.4	Mass flow rate .vs. outlet pressure for single disk micropump with Newtonian blood properties. $\alpha=0.2$, $m=3.5 \times 10^{-3}$ Ps.Sec, $n=1$ and $\tau_o=0.0$ [Pa].....	84
Figure 6.5	Mass flow rate .vs. outlet pressure for double disk micropump with Newtonian blood properties. $\alpha=0.2$, $m=3.5 \times 10^{-3}$ Ps.Sec, $n=1$ and $\tau_o=0.0$ [Pa].....	85
Figure 6.6	Mass flow rate .vs. outlet pressure for spiral micropump with Newtonian blood properties. $\alpha=0.2$, $m=3.5 \times 10^{-3}$ Ps.Sec, $n=1$ and $\tau_o=0.0$ [Pa]	85
Figure 6.7	Procedure for finding the optimum step size for the Matlab code. $\alpha=1$, $m=3.5 \times 10^{-3}$, $\tau_o=0.0$, $P_{in}=P_{out}=0.0$ and $n=1$	87
Figure 6.8	Meshed double disk micropump. $L=30 \times 10^{-6}$ m, $\alpha=1$, $R_{ave}=1010 \times 10^{-6}$ m and $\theta=270^\circ$	88
Figure 6.9	Convergence criteria in FLUENT	89
Figure 6.10	The effect of power law index on the performance of single disk	91

	micropump. $\alpha=1$, $P_{in}=1000$ Pa, $P_{out}=0.0$, $\theta=270^\circ$, $\tau_0=3.15 \times 10^{-3}$ Pa, $m=7.95 \times 10^{-3}$ Pa.Sec ⁿ	
Figure 6.11	The effect of power law index on the performance of double disk micropump. $\alpha=1$, $P_{in}=1000$ Pa, $P_{out}=0.0$, $\theta=270^\circ$, $\tau_0=3.15 \times 10^{-3}$ Pa, $m=7.95 \times 10^{-3}$ Pa.Sec ⁿ	92
Figure 6.12	The effect of power law index on the performance of spiral micropump. $\alpha=1$, $P_{in}=1000$ Pa, $P_{out}=0.0$, $\theta=270^\circ$, $\tau_0=3.15 \times 10^{-3}$ Pa, $m=7.95 \times 10^{-3}$ Pa.Sec ⁿ	93
Figure 6.13	The effect of changing the aspect ratio on the dimensionless axial velocity in a single disk micropump, W^* at the three-fourth of the dimensionless channel height. $\theta=270^\circ$, $P_{in}=P_{out}=0.0$ Pa, $\omega=1000$ rpm..	94
Figure 6.14	The effect of changing the aspect ratio on the dimensionless axial velocity in a single disk micropump, W^* at the one half of the dimensionless channel height. $\theta=270^\circ$, $P_{in}=P_{out}=0.0$ Pa, $\omega=1000$ rpm..	95
Figure 6.15	The effect of changing the aspect ratio on the dimensionless axial velocity in a double disk micropump, W^* at the three fourth of the dimensionless channel height. $\theta=270^\circ$, $P_{in}=P_{out}=0.0$ Pa, $\omega=1000$ rpm..	96
Figure 6.16	The effect of changing the aspect ratio on the dimensionless axial velocity in a double disk micropump, W^* at the one half of the dimensionless channel height. $\theta=270^\circ$, $P_{in}=P_{out}=0.0$ Pa, $\omega=1000$ rpm..	96
Figure 6.17	The effect of changing the aspect ratio on the dimensionless axial velocity in spiral micropump, W^* at the one half of the dimensionless channel height. $\theta=270^\circ$, $P_{in}=P_{out}=0.0$ Pa, $\omega=1000$ rpm	97
Figure 6.18	The effect of changing the aspect ratio on the dimensionless axial	98

velocity in spiral micropump, W^* at the one three-fourth of the dimensionless channel height. $\theta=270^\circ$, $P_{in}=P_{out}=0.0$ Pa, $\omega=1000$ rpm..

Figure 6.19	The mass flow rate [kg/Sec] at different aspect ratios for the three types of micro pumps. $L=30 \times 10^{-6}$ m, $P_{in}=P_{out}=0$	99
Figure 6.20	Dimensionless axial velocity at $\alpha=2$ for single disk micropump, $\Delta P=0$ [Pa]	100
Figure 6.21	Dimensionless axial velocity at $\alpha=2$ for double disk micropump, $\Delta P=0$ Pa	101
Figure 6.22	Dimensionless axial velocity at $\alpha=2$ for spiral channel micropump, $\Delta P=0$ Pa	
Figure 6.23	The dimensionless axial velocity in the dimensionless X and Y axes for a single disk micropump. $\alpha=1.0$, $P_{in}=P_{out}=0.0$ Pa, $\omega=1000$ rpm, $\theta=270=270^\circ$	101
Figure 6.24	The dimensionless axial velocity in the dimensionless X and Y axes for a double disk micropump. $\alpha=1.0$, $P_{in}=P_{out}=0.0$ Pa, $\omega=1000$ rpm, $\theta=270=270^\circ$	102
Figure 6.25	The dimensionless axial velocity in the dimensionless X and Y axes for a spiral micropump. $\alpha=1.0$, $P_{in}=P_{out}=0.0$ Pa, $\omega=1000$ rpm, $\theta=270=270^\circ$	104
Figure 6.26	The dimensionless velocity in X direction in the dimensionless X and Y axes for a spiral micropump. $\alpha=1.0$, $P_{in}=P_{out}=0.0$ Pa, $\omega=1000$ rpm, $\theta=270=270^\circ$	105
Figure 6.27	The dimensionless velocity in Y direction in the dimensionless X and Y axes for a spiral micropump. $\alpha=1.0$, $P_{in}=P_{out}=0.0$ Pa, $\omega=1000$ rpm,	105

	$\theta=270=270^\circ$	
Figure 6.28	Performance curves of the single disk, double disk and spiral micropumps represented by plotting the dimensionless flow rate .vs. the reduced Reynolds Euler number at an aspect ratio of ten	107
Figure 6.29	Performance curves of the three types of micropumps .vs. the reduced Reynolds Euler number at $\alpha=5$	107
Figure 6.30	Performance curves of the three types of micropumps .vs. the reduced Reynolds Euler number at $\alpha=2$	108
Figure 6.31	Performance curves of the three types of micropumps .vs. the reduced Reynolds Euler number at $\alpha=1$	108
Figure 6.32	Performance curves of the three types of micropumps .vs. the reduced Reynolds Euler number at $\alpha=0.5$	109
Figure 6.33	Performance curves of the three types of micropumps .vs. the reduced Reynolds Euler number at $\alpha=0.2$	109
Figure 6.34	Performance curves of the three types of micropumps .vs. the reduced Reynolds Euler number at $\alpha=0.1$	110
Figure 6.35	Dimensionless shear stress in double disk micropump through the channel cross sectional area, $\alpha=1$, $\Delta P=500$ Pa, $R=1000 \times 10^{-6}$ m, $\theta=3\pi$..	113
Figure 6.36	Dimensionless shear stress in single disk micropump through the channel cross sectional area, $\alpha=1$, $\Delta P=500$ Pa, $R=1000 \times 10^{-6}$ m, $\theta=3\pi$..	114
Figure 6.37	Dimensionless shear stress in spiral disk micropump through the channel cross sectional area, $\alpha=1$, $\Delta P=500$ Pa, $R=1000 \times 10^{-6}$ m, $\theta=3\pi$..	114

Nomenclature

Eu	Euler number
D_h	Hydraulic diameter
f	Fanning friction factor
F_D	Drag shape factor
F_P	Pressure shape factor
g	Gravitational acceleration
h	height
K_n	Knudsen number
L	Channel width
L_o	Channel length
m	Consistency index
n	Power law index
P	In-plan perturbation pressure
P_m	Cross sectional mean pressure
q	Volume flow rate
r	Channel radius
Re	Reynolds number
t	Time
u	Velocity component in x-direction
v	Velocity component in y-direction
w	Velocity component in z-direction

x,y,z Cartesian coordinates

Greek Symbols

Δ Difference operator

∇ Differential operator

α Aspect ratio

δ_{ij} Kronecker delta

λ Mean free path

η Apparent dynamic viscosity

μ Dimensionless apparent dynamic viscosity

ρ Mass density

τ_{ij} Shear stress tensor

Subscripts

i,j,k Coordinates direction indices

ch Channel

D Drag

av Average

o Initial

Superscripts

$()'$ First derivative

$()^*$

$(\overline{\quad})$ Average/ Reduced

**NUMERICAL SIMULATION AND EXPERIMENTAL
INVESTIGATION OF SHEAR DRIVEN MICROPUMPS FOR
BIOMEDICAL APPLICATIONS**

By

Aziz Abdulhafez Shaheen Al-Muhtaseb

Supervisor

Dr. Ahmed Al-Salaymeh

Co-Supervisor

Dr. Ala'aldeen Al-Halhouli

ABSTRACT

This study presents a comparison of the operation of three types of indirectly driven micropumps to be used for biomedical application. The three adopted of the micropumps are: the single disk micropump, the double disk micropump and the spiral channel micropump. Mathematical modeling and numerical simulation were applied to investigate the difference between the behaviors of the blood flow when considered as Newtonian fluid or adopting a non-Newtonian fluid flow that exactly presents the non-Newtonian nature of blood.

The governing equations that will control the flow of the fluid inside each type of the adopted pumps were derived with their boundary conditions, then these equations were

transformed to the dimensionless domain using several dimensionless parameters and after several mathematical manipulations; the final mathematical model was found. This mathematical model had been solved using the finite difference method, (FDM) and adopting the penalty method in order to overcome issue of the pressure-velocity coupling.

Then, the entire problem was investigated using the finite volume already programmed in the FLUENT software and using SIMPLE algorithm. Both results -that were obtained by the either mathematical modeling or the numerical simulations- were compared with the analytical solution of a Newtonian fluid flow of blood and results showed good agreement with analytical solution as a special case for code verification purposes.

During the study, the importance of adopting the exact model that describes the behavior of the considered fluid is illustrated along with the illustration of several parameters effect had been illustrated. One of the most important parameters was the wall shear stress; a big concern in this study is to use these micropumps without reaching the threshold shear stress in order to avoid the occurrence of the blood cells damage.

Finally, several experimental investigations have been carried out using two types of fluids: the first is distilled water which is considered as a Newtonian fluid while the other one is the blood mimicking fluid to simulate the non-Newtonian behavior of the blood.

CHAPTER 1

INTRODUCTION AND OBJECTIVES

1.1 Introduction

Micropumps are one of the key components in Bio Micro and Nano- Electro Mechanical systems (MEMS/NEMS) and micro-fluidic systems where the transportation of fluid is indispensable. Even with all the progresses and advancement in structural and material evolvement, the conventional macroscale pump technologies still have limitations in scaling size, operation voltage and power consumption to be applied to most recent MEMS/NEMS systems. In order to address these limitations, MEMS or micromachining-based micropumps have been studied since the early years of MEMS development [1].

Fluid flow mechanics is governed by a set of equations that cannot be solved analytically without imposing assumptions and boundary conditions. Further, reducing the dimensions of the devices into microscale results in dominant physical phenomena that are neglected in macro dimensions and are too significant to be neglected in microscales[2]. Nowadays there is growing interest in research on microfluidic systems, e.g. chemical analysis systems and microdosage systems [3]. One of the basic components in microfluidic systems is micropumps. Research on micropumps was initiated in 1980 and numerous different pumps have since been developed [3]. They can be manufactured in different materials, but mostly silicon and glass have been used as bulk materials. Silicon and glass have the advantage of being resistive to aggressive media. The pumps do not have any valves whereby the risk of fatigue is reduced [4].

During recent years several different micropumps have been presented based on different pump principles and using different actuation principles. Also, there is a growing interest in using the different components to build microliquid handling systems. Examples of microliquid handling systems are chemical analysis systems, e.g. fluid injection analysis and electrophoresis systems, microdosage systems and systems for counting red blood cells [4]. Micropumps are also used for ink jet printing, environmental testing and electronic cooling. Potential medical applications for small pumps include controlled delivery and monitoring of minute amount of medication, manufacturing of nanoliters of chemicals and development of artificial pancreas [5].

The rapid progress in fabricating and utilizing MEMS systems during the last decade has not been matched by corresponding advances in our understanding of the unconventional physics involved in the operation and manufacture of small devices. Providing such understanding is crucial to designing, optimizing, fabricating and operating improved MEMS devices.[5]

A numerical simulation using a commercial CFD program which together with a theoretical expression for the pump system can help in optimizing the complete pump and through optimization it will be possible to further increase pumping performance.

1.2 Dissertation Objectives

This study aims at developing numerical and experimental investigations of the fluid flow performance in shear driven single disk, double disk and spiral channel micropumps for biomedical applications. This will include studying the influence of different geometrical design parameters (i.e., channel heights) and boundary conditions

(i.e., moving boundary, and pressures at the inlet and outlet) on the flow performance of these micropumps.

Since biomedical fluids are normally carrying particles sensitive to shear stresses (e.g., blood with red cells), the effect of Newtonian viscosity of plasma and the non-Newtonian shear-thinning viscosity of blood on the particle will be simulated to optimize the pumps performance. This model will apply to single disk, double disk, and spiral-channel micropumps.

On the other hand, this study will present the fundamentals of microfluidics in biomedical applications by introducing the general fluid flow equations in indicial notations, differentiating between the micro and macro dominating physical phenomena, discussing the physics of microfluidics, and the importance of these phenomena in developing biomedical microdevices. A numerical model allows the detailed study of the effect of important parameters in the single disk, double disk, and spiral channel micropumps including Reynolds number, spiral angle, channel height, channel width, and the gap between the spiral wall and the fixed plate. Results will be verified experimentally (the experiments will be carried out for a special case of the current proposed work for verification purposes) on a microscale model that consider optimized geometrical design parameters and running speeds.

Current state of the art showed that computational fluid dynamics (CFD) commercial packages allow for detailed simulation of target parameters for simple as well as complex geometries with high accurate results. The software (FLUENT) uses finite volume method and allows building both 2D and 3D models of the flow geometry with high flexibility in defining the fluid physical parameters. The accuracy of the

solution that depends on a number of parameters including the element size and shape, integration coefficients and model complexity and flow type is an important part in this study.

In this work, mathematical modeling, numerical simulation and experimental investigation has been carried out for the three types of the adopted indirectly driven micropumps in this study. Table (1.1) below summarizes the three type of the adopted micropumps and the investigation performed for each type in this study:

Table 1.1: Summary of the micropumps investigations performed in this study.

Micropump Type	Working Fluid	Mathematical Modeling	Numerical Simulation	Experimental Investigation
Single disk micropump	Newtonian	×	√	×
	Non-Newtonian	√	√	×
Double disk micropump	Newtonian	×	√	×
	Non-Newtonian	√	√	×
Spiral channel micropump	Newtonian	×	√	√
	Non-Newtonian	√	√	√

Noting that the mathematical modeling carried out for the three adopted types of micropumps will work for the Newtonian working fluids after adopting several presetting constants that will be mentioned later on in this work.

1.3 Dissertation Outline

A brief introduction that discusses the differences between Newtonian and non-Newtonian fluids and the need of dealing with the fluids as non-Newtonian will be discussed in the second chapter. The second chapter will handle, also, a brief presentation for both the blood properties and the blood rheology, a brief discussion showing the classifications and several types of micropumps, and then concentrating on the operation and specifications of the micropumps handled in the current study. Last but not least, the second chapter will present a review for both the new trends and analysis used to simulate computational fluid flow and a review for blood micropumps in the literature review section.

In the fourth chapter of the present work, the flow behavior of the blood will be shown by set of equations based on several assumptions imposed on Navier-Stokes equation to simulate the steady, fully developed, and incompressible blood microfluidic flow, while the Herschel-Bulkley model will be adopted to encounter the non-Newtonian behavior of the blood. The entire set of the above equations will be linearized using the “simple iterative update of coefficients” method. After that, the above set of equations will be written in the central finite difference formulation. At the end of third chapter the set of governing equations and boundary conditions that for each type of micropumps will be presented.

The third chapter will introduce the different CFD simulation methods, side by side concentrating on the FLUENT package, grid optimization and their verification. And at last the convergence criteria and grid independent solution will be discussed.

An experimental investigation will be made to the spiral micropump at which the experimental setup and procedure adopted to test the spiral micropump will be presented in the fifth chapter.

The validation of the mathematical model and its grid optimization will be shown in the first section of the sixth chapter; this will be followed by showing a comparison between Newtonian and non-Newtonian results. This will be followed by showing the effect of the aspect ratios of the performance of the three adopted types of micropumps. After that, the performance curves for the different types of micropumps will be constructed. The experimental results will be investigated in next section. The analytical and theoretical shear stress analysis will be discussed in the last section of the sixth chapter.

In the last chapter of the present work, the above study conclusions will be illustrated and recommendations for the future work will be propose. .

CHAPTER 2

LITERATURE SURVEY

2.1 Micropumps

The viscous micropump idea depends on generating significant pressure heads in the viscosity dominated micro-channels by the simple rotation of a rigid element contiguous to the flow field, and it was firstly introduced in 1996 [18]. Number of experimental, theoretical and numerical studies on the viscous micropumps with different configurations has been followed. Eccentric, single and double disk, and spiral channel viscous micropumps are the most viscous micropumps studied thoroughly during last decade. Viscous micropumps are easy to fabricate, have the capability of handling high viscous fluids and the possibility of operation with no valves. This section provides an overview of several types of tested viscous micropumps and reviews the numerical and analytical studies performed to understand, and improve their performance.

2.1.1 Eccentric Pump

The principle of the eccentric (novel) pump is based on generating axial fluid motion in micro channel through the rotation of a cylinder placed asymmetrically in a viscous fluid medium as shown in figure 2.1 [18]. Rotating the cylinder generates a net shear stress against externally imposed pressure gradient in the direction of the flow.

The experiments were carried out by placing the rotating cylinder in leak proof bearings within the tank, and connected with an external motor. The square plate was tightly fitted on the plexiglass walls, where it can move along the wall, and the gap

height from the floor of the tank, which represents the channel height, can be adjusted. Tests were performed using high viscous fluid, glycerin, at low Reynolds number in the range of 0.01-10, using various rotor cross sections: circular, square, and rectangular. Results showed that the flow depends on the geometrical parameters: channel height, and rotor eccentricity, and proportional to the angular velocity. Circular cylinder cross section gave the best pumping performance, and a flow velocity of about 10% of the speed of the cylinder surface, this is consistent with the results obtained from solving Navier- Stokes equation in the limit of negligible inertia forces. A reversible behavior utilizing low-Reynolds-number viscous effect can also be investigated to rotate the cylinder by applying a continuous flow within the channel.

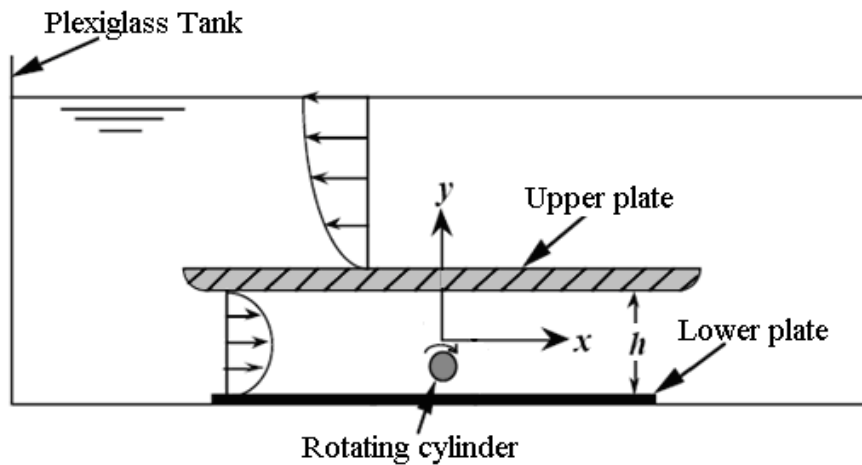


Fig. 2.1: The principle of the eccentric pump is based on generating axial fluid motion in micro channel through the rotation of a cylinder placed asymmetrically in a viscous fluid medium [2].

Following these experiments, several numerical and analytical investigations have been performed. A numerical study of the three-dimensional viscous fluid flow in a novel pump/turbine device appropriate for microscale applications has been performed [21]. The device essentially consists of a rotating or free-to-rotate cylinder eccentrically

placed in a channel, and was shown to be capable of generating a net flow against an externally imposed pressure gradient, or, conversely, generating a net torque in the presence of an externally imposed bulk flow. Finite-element simulations were carried out to study the influence of the width and other geometric as well as dynamic parameters and the results were compared to previous two-dimensional numerical and physical experiments. The three-dimensional simulations indicate a gradual decrease of the bulk velocity and pump performance as the two side walls become closer providing increased viscous resistance to the flow. However, effective pumping is still observed with extremely narrow channels.

In a later study, the same research team performed a numerical simulation of the viscous micropump solving Navier–Stokes equations for the case of the cylindrical rotor at operating range of Reynolds beyond 100 [82]. Critical values for optimum performance were calculated. The highest bulk velocity was achieved when the spacing between the plates is around one and half times the cylinder diameter for a fixed eccentricity or at the maximum eccentricity for a fixed plates spacing. The load flow rate curve for the pump was also plotted, with part of the curve in the negative part of the flow rate axis. This showed that the flow will change direction if the load is increased beyond the pump capability. The maximum efficiency of the pump was determined to be approximately 2.5% for the optimum plate spacing. However, it was observed that the viscous dissipation might cause a measurable temperature rise since viscous forces are the driving forces.

In order to check the effect of viscous dissipation on the pump performance, the same team performed a second numerical simulation [21]. In this study, they solved the

continuity equation, the momentum equation with temperature dependent viscosity, and the energy equation with viscous dissipation terms retained, all coupled together. It was determined that viscous dissipation would not cause a measurable rise in the bulk temperature of the fluid in MEMS applications, yet it may cause a significant rise in the fluid temperature combined with steep temperature gradients near the rotor where the shear stresses are maximum. They also introduced a numerical study for the three-dimensional effects of the sidewalls of the channel, and investigated the possible utilization of the inverse device as a turbine. Results showed reduction in the pumping performance associated with reducing the channel width, where viscous resistance to the flow is increased. However, effective pumping is still noticeable at widths equals a fraction of the rotor diameter. The highest bulk velocity is achieved when the rotor is in contact with either the upper or lower channel walls.

Lubrication analysis and boundary integral simulations for the eccentric pump has been conducted in the limit where the gap (channel) height is small compared with the radius of the pump cylinder [20]. Analytical and numerical investigations at low Reynolds numbers were performed in order to obtain the optimal geometry, and analytical relations among flow rate, torque, pressure drop, and rotation rate relations were provided. The study begins by using the lubrication approximation to provide an analytical solution, where the results obtained from this solution were used to calculate the operating flow parameters and geometry. Then a numerical solution for the stokes flow problem was developed and the region of the lubrication approximation is determined. Results showed that such pumps cannot be developed that achieves maximum flow rate and rotation simultaneously.

A numerical investigation for the transient performance of a single rotor eccentric viscous micropump was investigated [22]. The effect of pump parameters: channel height, eccentricity, Reynolds number, and back pressure on the transient performance of the micropump were studied numerically. The time required to reach steady state operation was calculated, and showed good agreement with previously reported experimental data. The rotor eccentricity parameter was found to be the most important parameter in determining the overall pump transient performance, and the generated pressures can be in the range of 0.1 Pa to 1 kPa or more. More numerical investigations for the transient performance of a rotating cylinder of with different cross-sectional geometries: cylindrical, rectangular, and square were carried out [23]. The effects of geometrical parameters: channel height, and eccentricity, and Reynolds number, pressure load on the flow performance were studied. Results showed that the time required for the flow to attain steady state conditions is increased with increasing the channel height, and that the circular rotor provides the highest non-dimensional velocity.

To enhance the performance of the viscous micropump, further numerical investigations have been carried out by increasing the number of the cylindrical rotors, which have been placed in series or parallel inside the microchannel [24]. Four configurations of rotors were studied: the dual-horizontal rotor, triple-horizontal rotor, symmetrical dual-vertical rotor, and the eight-shaped-dual-vertical rotor.

Multi-rotor micropumps have been found to provide higher flow rates and back pressures, either at series or parallel placing. Results showed that the performance and efficiency of the micropump depend on the pump geometry, where the best efficiency

and highest flow rate are obtained for the symmetrical dual-vertical rotor micropump, while the triple-horizontal rotor pump gives the highest back pressure, and that further research efforts are required in order to enhance pump performance and efficiency.

2.1.2 Single and Double Disk Micropumps

Single and double disk viscous micropump are that use viscous stresses to produce pumping effect by employing one (single) or two (double) disks and a wiper to force the fluid through a passage [12]. These micropumps have been investigated experimentally. Further visualization experiments to provide information on the relative importance of viscous forces, centrifugal forces, and static pressure variations were performed. The experimental results showed nearly linear increase in the flow rate with the rotational speed, which support the dominant effect of viscous forces in small scales. A relatively high flow rate in comparison with other micropumps with the same typical size is achieved.

The same group published further detailed experimental study for the performance characterization of the single disk viscous micropump. An approximate analytical model estimates for the flow field and pressure rise that depends on the pump geometry, disk rotational speed, and fluid properties and ignores the channel aspect ratio $h / (r_2 - r_1) \ll 1$ and the radial velocity component $v_r=0.0$ have been also derived [16]. This model showed deviation from the experimental results as the condition $h / (r_2 - r_1) \ll 1$ is not satisfied.

The single disk viscous pump is comprised of a spinning disk rotating at a close proximity above a C-shaped channel located under the disk and forming the pump chamber. Fluid inlet and outlet ports located at ends of the C-shaped channel. Figure 2.2

shows a view of the single disk pump components. The spinning flat cover is brought to close proximity with the upper walls of the C-channel creating a small gap. The spinning of the channel creates a drag force which moves fluid from channel inlet to channel outlet due to viscous interactions between the fluid and the walls of the channel.

Experimental results were found to be consistent with the derived analytical model for $h/(r_2 - r_1)$, and that the experimental data deviates from the analytical model for $Re > 110$. They found also that the pressure rise can be increased by decreasing the flow passage height, and increasing the rotational speed, fluid viscosity, and the circumferential span of the shear channel. While the flow rate is increased by increasing the flow passage height, width, and disk rotational speed.

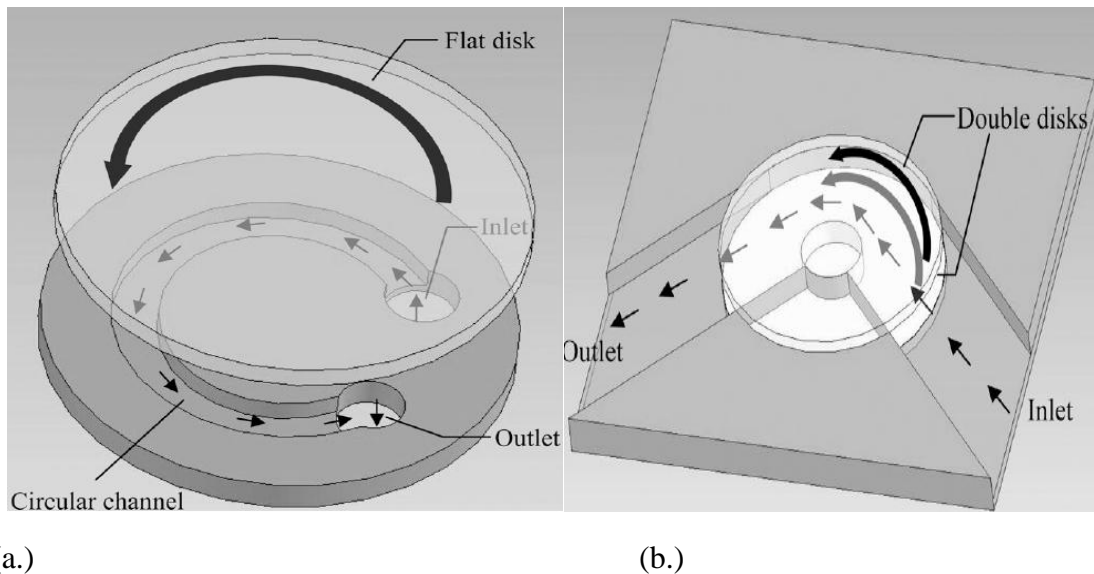


Fig. 2.2: An illustration of the (a.) single and (b.) double disk viscous micropumps [54].

Further numerical and analytical parametric study for the effect of pump design parameters: radius ratio (r_1/r_2) and aspect ratio (h/w) on the flow performance for single and double disk viscous micropumps have been performed [9]. A number of 3D numerical models for the single and double disk micropumps estimating the influence

of radius ratio and other models estimating for the influence of aspect ratio have been built and analyzed at different boundary conditions using FVM.

After deriving the flow rates in the disk pumps analytically for each design parameter, a generalized analytical flow model has been presented. Obtained analytical flow rates were compared with a numerical finite volume solution for several 3D models of the single and double disk pumps at different aspect ratios and radius ratios, and were found in good agreement and verified the generalized model. Generalized model was used to estimate for the flow rates in the single disk viscous pump at different aspect ratios, where the solution was found in good agreement with published experimental results.

Pressure and drag shape factors were also developed to simplify the presentation of the influence of velocity and pressure boundary conditions for a wide range of design parameters on the flow performance. Also, it has been found that the flow rate varies linearly with both the pressure difference and boundary velocity, which supports the validity of the linear lubrication model employed. The study introduces a full model estimates for the influence of geometrical parameters: channel height, width, inner and outer radiuses.

2.1.3 Spiral Channel Micropumps

A spiral-channel viscous pump which works by rotating a disk with spiral groove at a close proximity over a stationary plate, using a planar mechanism has recently proposed [6]. As illustrated in figure 2.3, the pump works with no valves, and the fluid contained in the spiral channel between the disk and the plate is subjected to a net tangential viscous stress on its boundaries, where a positive pressure gradient is

established in the direction of flow. Two holes at either end of the spiral channel provide the required inlet and outlet for the pumped fluid.

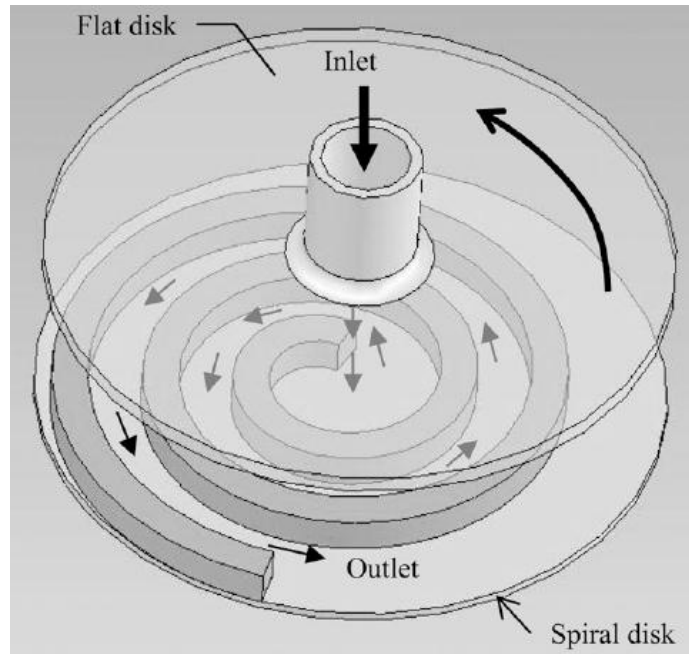


Fig. 2.3: A spiral-channel viscous pump components [54].

An approximate analytical solution for the flow field in the spiral micropump has been constructed [6]. This approximation neglects the curvature of the spiral and treats it as a straight channel with a stationary bottom wall and moving top and side walls. This is further simplified using symmetry into the 2D flow in its middle plane of the channel by considering a large aspect ratio $w/h \rightarrow \infty$, which neglects the effect of the side walls of the spiral channel. The obtained model closely resembles the classical Couette-Poiseuille model, and was solved analytically for the velocity and pressure fields. The modeling parameters and the performance relations of the approximate model are summarized in Table 2.5.

Table 2.1: The modeling parameters and the performance relations of the approximate spiral pump model

Quantity	Formula
Channel boundary velocity	$w_{ch}(z) = \omega_o + \frac{k\omega}{r_a}$
Channel boundary velocity gradient	$\dot{w}_{ch}(z) = \frac{\partial w_{ch}(z)}{\partial z}$
Channel boundary mean velocity	$\bar{w}_{ch}(z) = \frac{1}{l} \int_0^1 w_{ch}(z) dz$

An analytical derivation for the effect of the channel aspect ratio on the flow performance of the spiral channel micropump has also been recently reported (Kilani et al., 2006). In this work the effect of channel aspect ratio is described in terms of a pressure shape factor and a drag shape factor that influences pump performance.

2.2 Rheological investigation of blood as a non-Newtonian fluid

In most of the studies mentioned above, the flowing blood is assumed to be Newtonian. The assumption of Newtonian behavior of blood is acceptable for high shear rate flow. It is not, however, valid when the shear rate is low as is the flow in smaller arteries and in the downstream of the stenosis. It has been pointed out that in some diseased conditions, blood exhibits remarkable non-Newtonian properties. Thurston [66] has shown that blood, being a suspension of enumerable number of cells, possesses significant viscoelastic properties in the frequency range of physiological importance.

Deutsch and Phillips [67] experimentally studied the red cell suspensions and blood plasma to small disturbances in circular Couette flow for the stability of human blood. They confirmed the viscoelastic nature of whole blood and blood cell suspensions. They found that the blood plasma to be Newtonian. They identified two mechanisms by which elasticity may arise in blood namely red cell deformability and red cell aggregation. Liepsch and Morvec [30] investigated the flow in a right 90° bifurcation under steady flow conditions. They found a striking influence of the non-Newtonian properties of polyacrylamide solution on the axial velocity distribution. Especially the size and the location of the region of flow reversal were affected by the non-Newtonian properties of the fluid. Ku and Liepsch [31] studied the axial velocity distribution in a 90° bifurcation under pulsatile flow conditions, also using polyacrylamide solution. They found a reduction of the size of the region with flow reversal for the non-Newtonian fluid in a rigid model. It has to be remarked though, that polyacrylamide solution is much more elastic than blood.

The laminar steady and nonsteady flow of non-Newtonian fluids through a tube was studied by Theodorou and Bellet [32]. Velocity distribution, the pressure drop along the tube and the wall stress were determined. Nakamura and Swada [33] numerically studied the laminar steady flow of non-Newtonian fluid through an axisymmetric stenosis using the finite element methods. The results showed that the non-Newtonian property of blood decreases the axial force acting on the stenosis. The role of non-Newtonian characteristics (such as shear rate dependent viscosity and viscoelasticity) on flow behavior across the sudden expansion step in a circular pipe was investigated by Pak et.al [34] for a wide range of Reynolds numbers including the turbulent flow. The reattachment lengths for the viscoelastic fluids in the laminar flow

regime are found to be much shorter than those for the Newtonian fluid. However, in the turbulent flow regime, the reattachment length for the viscoelastic fluids is two or three times longer than those for water, and gradually increases with increasing concentration of viscoelastic solutions.

The effect of nonaxisymmetric hematocrit distribution on the flow of human and cat blood in small blood vessels of the microcirculation was studied by Das et al [35]. Human blood was described by Quemada's rheological model and the cat blood was described by Casson's model. Investigation of the non-Newtonian steady flow in a carotid bifurcation model by Gijsen et al. [36-37] indicated that the shear thinning is the dominant non-Newtonian property of blood and the viscoelasticity may be ignored for the prediction of the velocity distribution.

Hussain et al. [38] investigated the qualitative analysis of parameters that affect apparent blood viscosity at different low shear rates. i.e. between 1 s^{-1} and 100 s^{-1} . Viscosity profile of a large number of blood samples from thromboembolic stroke cases and age and sex matched health controls were studied which confirmed non-Newtonian power law behavior of blood. The power law coefficients, n and k , which are unique to each blood sample, were related with blood viscosity parameters in the form of a mathematical equation by performing non-linear regression analysis. The calculation of n and k of a blood sample using the equation of obtained, provided a quick information on its apparent viscosity values at any given shear rate without viscometry. The calculated and the experimental viscosity were found in good agreement within a permissible error range.

Buchanan et al. [39] studied the rheological effects on pulsatile hemodynamics in a stenosed tube. They considered a transient laminar axisymmetric flow through a tube with a smooth local area of reduction of 75%. The influences of three rheology models (i.e. Newtonian, power law and Quemada) were investigated using an experimentally validated control volume method. Three Womersley numbers were compared for a sinusoidal input with a mean Reynolds number of 200. The results showed that for the highest Womersley number considered, a second co-rotating vortex was formed distal to the primary vortex. It was found that the shear-thinning rheological models have a secondary effect on the flow field that primary appears in terms of subtle changes to the hemodynamic wall parameters. The non-Newtonian models affected the entrainment of fluid like particles in the post-stenotic region measurably. The particle residence time (PRT), defined as the ratio of transient to steady residence times, was found to be less than or equal to unity for the majority of fluid elements for all rheology's' and Womersley numbers considered.

Shalman *et al.* [40] established a relationship between actual hemodynamic conditions and the parameters that define stenosis severity in the clinical setting in stenosed coronary artery. A constant flow regulation mechanism resulted in coronary flow reserve (CFR) and fractional flow reserve (FFR) values that were within the physiological range, while a constant wall-shear stress model yielded unrealistic values. Neofytou and Drikakis [41] numerically investigated the instability of non-Newtonian flow in a channel with a sudden expansion. Three non-Newtonian models, Casson, Power-Law and Quemada models were employed. Two groups of three cases were considered for all the models. In the first group were the cases of constant $Bi=0.1, 0.06$ and 0.02 and varying Re and in the second group were the cases of constant

$Re=400,500$, and 600 and varying Bi . Three stages of transition from symmetric to asymmetric condition are observed for all the models. The length of the vortices at the point of transition from symmetry to asymmetry is the same for all three non-Newtonian models. Chen and Liu [42] numerically investigated the influence of the non-Newtonian property of fluid as well as of curvature and out-of-plane geometry in the non-planar daughter vessel on wall shear stress (WSS) and flow phenomena. The results supported that the non-planarity of blood vessels and the non-Newtonian properties of blood are an important factor in hemodynamics and may play a significant role in vascular biology and pathophysiology. Recently, Mandal [43] numerically solved the problem of non-Newtonian and non-linear blood flow through a stenosed artery. The non-Newtonian behavior of the streaming blood is characterized by the generalized Power-law model. The model was employed to study the effects of the taper angle, wall deformation, and severity of the stenosis within its fixed length, steeper stenosis of the same severity, nonlinearity and non-Newtonian rheology of the flowing blood on the flow field.

Finally, Herschel Bulkley non-Newtonian model was considered in the present study to express the real behavior of blood flow through the single disk, double disk and spiral channel micropumps.

CHAPTER 3

THEORITICAL AND NUMERICAL BACKGROUNDS

3.1 Introduction

In this chapter, a brief about the micropumps that discusses their importance, types, and the history of the type used in this thesis will be discussed. Then, several blood properties will be clarified in the third chapter. The equations that will be used to deal with the microfluidic problems using both Newtonian and non-Newtonian fluids will be illustrated in the fourth section, this will include an illustration of the several non-Newtonian fluid flow models used to describe the non-Newtonian flows. Last, a brief about the previous done works that are related to the core of this study will be shown in the literature review chapter.

3.2 Micropumps

As a result of the scaling size, operation voltage, and power consumptions limitations of the conventional macroscale pumps to be used in the most recent MEMS/NEMS systems and in order to meet the huge development and demand of the various MEMS/NEMS systems, enormous number of researchers and scientists had studied and improved several types of micropumps at which they had classified the micropumps into two categories:

A. The Directly Driven Micropumps: this type of micropumps has no mechanical moving parts (i.e. actuator) to force the pumping media to move; instead of that the directly-driven micropumps directly forces the pumping media to move using a special dragging mechanism. Reference to the dragging mechanism; the directly-driven micropumps are categorized into four subdivisions which are: the electrohydrodynamic

micropumps (EHD), the electroosmotic micropumps, the magnetohydrodynamic (MHD) micropumps and the surface wave-induced micropumps[1].

B. The Indirectly-Driven Micropumps: at which this type of pumps the actuators produce an external induced pressure that forces the pumping media to move. Reference to the actuator mechanism of operation; the indirectly-driven micropumps are classified into four subdivisions which are: reciprocating membrane, peristaltic, rotary, syringe and bubble indirectly-driven micropumps.

The pumping media, such as liquid or gas, in the indirectly-driven micropumps is forced to move via the effect of externally induced pressure that is created by an actuator. Reference to the mechanism adopted to operate those directly-driven micropumps; the indirectly driven micropumps are distributed into five sub-groups which are: the reciprocating membrane micropumps, the most common sub-group, at which the micropumps consists from a reciprocating membrane and a check valve, peristaltic micropumps at which the flow is generated through the consecutive motion of multiple membranes in series, syringe (or infusion) micropumps, the rotary micropumps and the bubble-driven micropumps at which the force is exerted on the fluid through the micron-size of the bubbles. Figure 3.1 below summarizes the up to date most known rotating micropumps

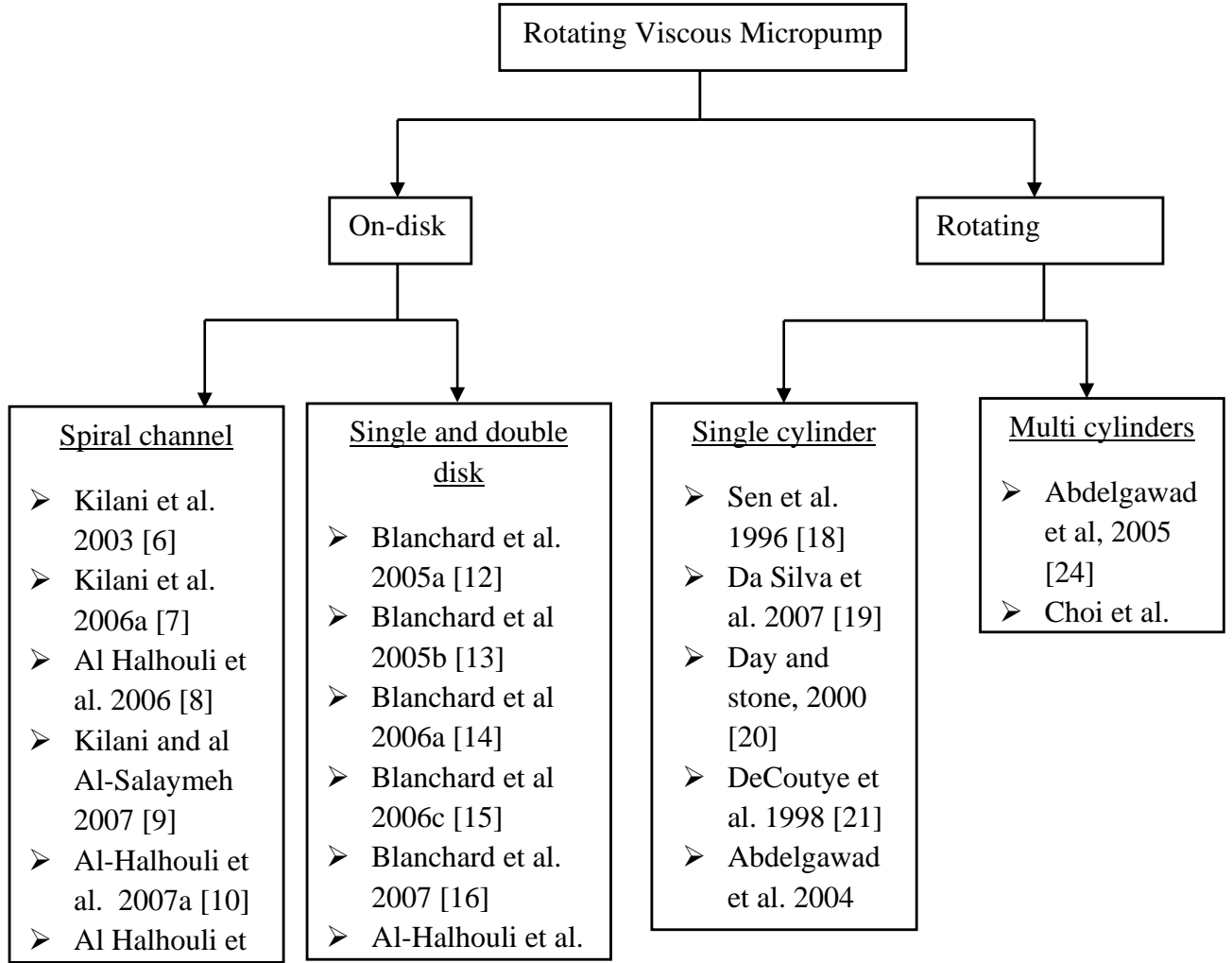


Fig 3.1: Classification of rotating viscous micropumps and a survey of references.

Noting that, the three types of micropumps adopted in the study are classified in the rotary indirectly-driven micropumps.

3.3 Blood Properties

Blood is a heterogeneous suspension containing several different components. Blood consists of plasma with red blood cells (erythrocytes), white blood cells (leucocytes), and platelets (thrombocytes) in suspension. In the typical adult human, blood is composed of approximately 45% of plasma, and the other 55% consists of a further heterogeneous mixture of cellular components. Plasma is composed of 93%

water and 3% particles: electrolytes, proteins, gases, nutrients, hormones, and waste products. Erythrocytes, or red blood cells (RBCs), are flattened discs with a depressed center, about $5.2 \mu m$ thick and $7 \mu m$ wide. The depressed center provides increased surface area for the diffusion of gases. RBCs contain no nuclei or mitochondria, but they do contain hemoglobin. It is the hemoglobin, which binds to oxygen and allows the RBCs to transport oxygen to cells. Leukocytes, or white blood cells (WBCs), are larger than RBCs. They have a nuclei and mitochondria which enable them to move around. WBCs are capable of squeezing through pores in capillary walls in order to reach sites of infection. This aids WBCs in their participation in the body's immune response. Platelets are the smallest formed element and are actually fragments of large bone marrow cells. They contain no nuclei but are still capable of movement and function in blood clotting. All formed elements of blood are produced in the myeloid tissue, or red bone marrow, in a process known as hemopoiesis. Furthermore, all these cells are deformable, with the erythrocytes being the most deformable. Significant deformations occur when the cells are passing through the capillaries. However, the cell membranes do not rupture because each cell has a cytoskeleton that supports its shape.

Therefore, the mechanical properties of blood should be studied by analyzing a liquid containing a suspension of flexible particles. A liquid is said to be Newtonian if the coefficient of viscosity is constant at all the rates of shear. This condition exists in most homogeneous liquids, including blood plasma. But the mechanical behavior of a liquid containing a suspension of particles can vary such that the liquid becomes non-Newtonian. These deviations become particularly significant when the particle size becomes appreciably large in comparison to the dimension of the channel in which the fluid is flowing. The situation happens in the microcirculation (for the small arterioles

and capillaries). If the suspended particles are spherical and non-settling, then for any motion the shear stress will be proportional to the rate of shear and the suspension will be proportional to the rate of shear and the suspension will behave as a Newtonian fluid. However, if the suspended particles are not spherical or deformable in any way, then the shear stress is not proportional to the shear rate. The cells suspended in blood are not rigid spheres; therefore the behavior of the blood is non-Newtonian. But it has shown that the human blood is Newtonian at all rates of shear for hematocrits (proportion, by volume, of the blood that consists of red blood cells) up to about 12%. In general blood has a higher viscosity than plasma, and as the hematocrit rises, the viscosity of the suspension increases and non-Newtonian behavior is observed, being detectable first at very low rates of shear. Studies with human blood show that viscosity is independent of shear rate when the shear rate is high.

In large channels it is reasonable to assume blood has a constant viscosity because the channel diameters are large compared with the individual cell diameters and because shear rates are high enough for viscosity to be independent of them. For very small channels, it is not easy to reach conclusions as to the Newtonian nature of blood because some effects tend to decrease the viscosity and others to increase it.

3.4 Governing Equations

The behavior of any fluid dynamics problem can be described and determined by a set of governing equations derived from the conservation flow models (i.e. conservation of species, mass momentum and energy equations). The same continuum flow model behavior can also be adopted when dealing with plenty of microfluidic

problems. Several important properties related to the fluid dynamics will be discussed and illustrated in the following sections.

The mass, momentum, and energy equations (i.e. the governing equations) in their full form in Cartesian coordinates are expressed as the following:

The conservation of mass equation:

$$\frac{\partial \rho}{\partial t} + \frac{\partial(\rho U_i)}{\partial x_i} = 0.0, i = 1,2,3 \quad (3.1)$$

Where ρ is the fluid density, t is the time, U_i are the Cartesian velocity components (u,v,w) in the (x,y,z) Cartesian coordinates respectively.

The Conservation of momentum equations are represented in Navier Stokes equations in the three Cartesian coordinates, which can be represented as:

$$\rho \left[\frac{\partial U_i}{\partial t} + U_j \cdot \frac{\partial U_i}{\partial x_j} \right] = - \frac{\partial P}{\partial x_i} + \frac{\partial \tau_{ij}}{\partial x_j} + \rho g_i, i = 1,2,3 \text{ and } j = 1,2,3 \quad (3.2)$$

At

which

$$\tau_{ij} = \eta \left[\frac{\partial U_j}{\partial x_i} + \frac{\partial U_i}{\partial x_j} - \frac{2}{3} \delta_{ij} \frac{\partial U_k}{\partial x_k} \right] \quad (3.3)$$

Where η is the apparent dynamic viscosity which depends on the Newtonian or non-Newtonian flow behavior (this will be discussed in the following chapters) and δ_{ij} is the Kronecker delta.

The conservation of energy equation is written as the following:

$$\rho c_p \left[\frac{\partial T}{\partial t} + U_j \cdot \frac{\partial T}{\partial x_j} \right] = \nabla \cdot (K \nabla T) + \dot{q} + \eta \Phi, i = 1,2,3 \text{ and } j = 1,2,3 \quad (3.4)$$

Where c_p is the specific heat at constant pressure, Thermal conductivity, Φ is the viscous dissipation and \dot{q} is the heat generation term.

The current study deals only with the continuity and momentum equations. Several terms and assumptions has to be illustrated before solving the conservation equation some of these terms are: Newtonian and non-Newtonian fluids, Laminar and turbulent fluid flows, fully developed flow, incompressible and compressible flows, the slip and no slip boundary conditions and the friction factors. A brief illustration of these terms will be considered in the following subsections.

3.5 Non-Newtonian fluids

A Newtonian fluid is one, which exhibits the following property. The shear stress, or resisting forces, and velocity gradient, or rate of deformation $\frac{du}{dy}$, are linearly related

$$\tau = \mu \frac{du}{dy} \quad (3.5)$$

Where μ is the coefficient of viscosity.

A non-Newtonian fluid is a fluid in which the viscosity changes with the applied shear force. As a result, non-Newtonian fluids may not have a well-defined viscosity. For non-Newtonian fluids, the shear stress can be written in terms of non-Newtonian viscosity η :

$$\bar{\tau} = \eta(\bar{D})\bar{D} \quad (3.6)$$

where η is a function of the shear rate $\dot{\gamma}$ and \bar{D} is a rate of deformation tensor and is defined by

$$\bar{D} = \left(\frac{\partial u_j}{\partial x_i} + \frac{\partial u_i}{\partial x_j} \right) \quad (3.7)$$

$\dot{\gamma}$ is also related to the second invariant of $\overline{\overline{D}}$ and is defined as

$$\dot{\gamma} = \sqrt{\overline{\overline{D}}:\overline{\overline{D}}} \quad (3.8)$$

In the following sub-sections; the most known non-Newtonian fluid flow models will be discussed.

3.5.1 Non-Newtonian Power Law Model

The apparent blood viscosity, which is the ratio of shear stress to shear rate at a particular rate of shear, can be expressed as

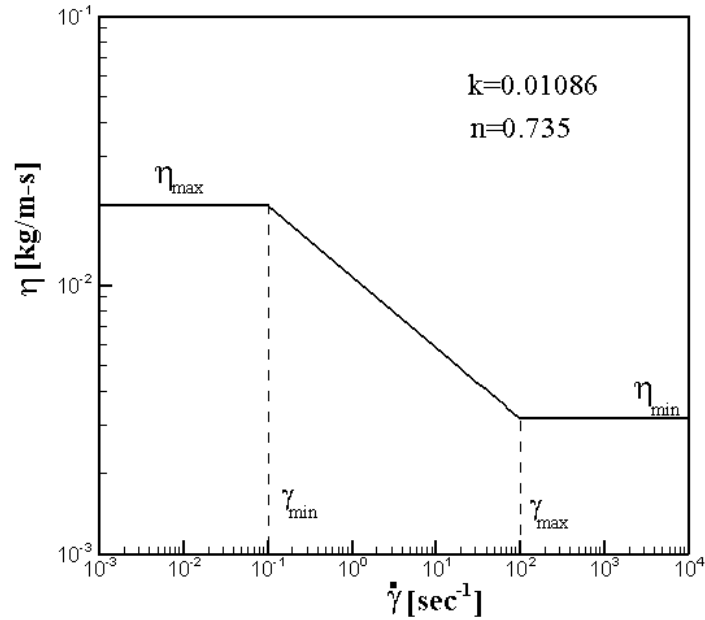
$$\eta = \begin{cases} \eta_{min} & \dot{\gamma} > \dot{\gamma}_{max} \\ k\dot{\gamma}^{n-1} & \dot{\gamma}_{min} < \dot{\gamma} < \dot{\gamma}_{max} \\ \eta_{max} & \dot{\gamma} < \dot{\gamma}_{min} \end{cases} \quad (3.9)$$

Where k is the average viscosity of the fluid (the consistency index), n is a measure of the deviation of the fluid from Newtonian (power-law index) shows the variation of viscosity with shear rate according to the non-Newtonian power law. Here η_{min} and η_{max} are respectively, the lower and upper limits of the power law. Figure 2.2 shows the how the viscosity is limited by $\min \eta$ and $\max \eta$ at low and high shear rates.

The power law model is known to be limited to approximately three decades of accuracy and for the rheological data here $\dot{\gamma}_{max} = 100 \text{ s}^{-1}$, $\dot{\gamma}_{min} = 10 \text{ s}^{-1}$. Table 2.1 shows the Non-Newtonian Power-Low model parameters.

Table 3.1: Non-Newtonian Power-Law model parameters

Parameter	List
$\eta_{\infty} \left(\frac{kg}{m} \cdot s \right)$	0.0032
$\eta_o \left(\frac{kg}{m} \cdot s \right)$	0.02
k	0.1086
n	0.735

**Figure 3.2:** Variation of Viscosity with Rate of Strain According to the Non-Newtonian Power [57].

3.5.2 The Carreau Model

The Carreau model attempts to describe a wide range of fluids by the establishment of a curve-fit to piece together functions for both Newtonian and shear-thinning ($n < 1$) non-Newtonian laws. In the Carreau model, the viscosity is

$$\eta = \eta_{\infty} + (\eta_o - \eta_{\infty}) [1 + (\dot{\gamma}\lambda)^2]^{(n-1)/2} \quad (3.10)$$

Where the parameters n , λ , η_0 and η_∞ are dependent upon the fluid. λ is the time constant, n is the power-law index, η_0 and η_∞ are, respectively, the zero and infinite shear viscosities. Figure 2.3 shows how viscosity is limited by η_0 and η_∞ at low and high shear rates. n can be varied to obtain the power-law region of the shear-thinning behavior. Relaxation time, λ , when increased while keeping all the other parameters constant shifts the power-law region to the right. Thus it dictates the shear-rates at which the power-law transition takes place. The power law index n governs the power-law regime in general. Table 3.2 shows the Carreau model parameters.

Table 3.2: Carreau model parameters.

Parameter	List
$\eta_\infty (\frac{kg}{m} \cdot s)$	0.0032
$\eta_0 (\frac{kg}{m} \cdot s)$	0.05
$\lambda (Sec)$	8.2
n	0.2128

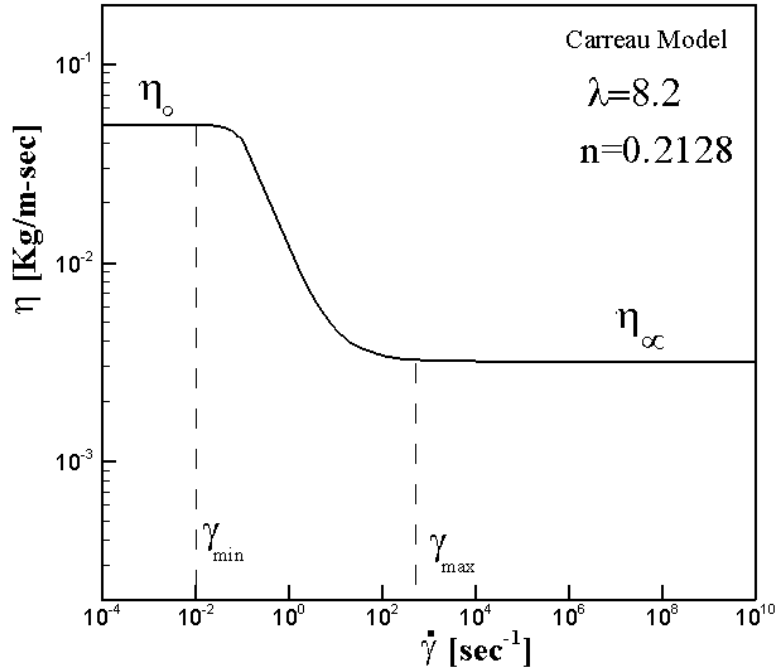


Figure 3.3: Variation of Viscosity with Rate of Strain According to the Carreau Model [57].

3.5.3 The Carreau-Yasuda Model

The Carreau-Yasuda model looks like:

$$\eta = \eta_\infty + (\eta_0 - \eta_\infty)[1 + (\dot{\gamma}\lambda)^a]^{(n-1)/a} \quad (3.11)$$

Where $\dot{\gamma}$ is the shear rate, η_∞ is the shear rate viscosity at infinite shear rates, η_0 is the shear rate viscosity and λ is the relaxation time in seconds. Parameters a and n can be varied to obtain the power-law region of shear-thinning behavior. Relaxation time, λ , when increased while keeping all the other parameters constant shifts the power-law region to the right. Thus it dictates the shear-rates at which the power-law transition takes place. Parameter ‘ a ’ dictates the curvature at the top of the curve. A higher ‘ a ’ means a sharper transition of viscosity into the knowledge of these parameters become necessary while implementing a Carreau-Yasuda model into numerical simulations.

Table 3.3 shows the Carreau-Yasuda model parameters. Figure 3.4 shows how viscosity is limited by η_o and η_∞ at low and high shear rates.

Table 3.3: Carreau-Yasuda model parameters

Parameter	List
$\eta_\infty (\frac{kg}{m} \cdot s)$	0.0032
$\eta_o (\frac{kg}{m} \cdot s)$	0.016
$\lambda (Sec)$	8.2
n	0.2128
a	0.64

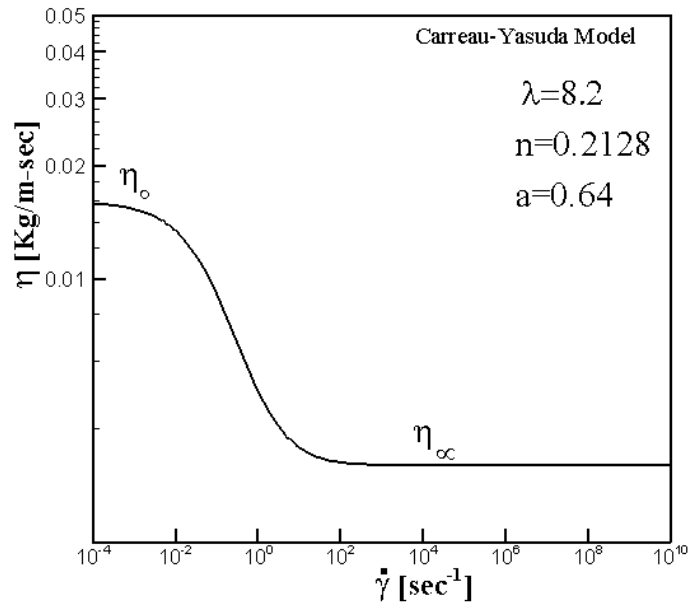


Fig. 3.4: Variation of Viscosity with Rate of Strain According to the Carreau-Yasuda Model [57].

3.5.4 Herschel-Bulkley Model for Bingham Plastics

The power law model described above is valid for fluids for which the shear stress is zero when the strain rate is zero. Bingham plastics are characterized by a non-zero shear stress when the strain rate is zero:

$$\tau = \tau_o + \eta \bar{D} \quad (3.12)$$

Where τ_o is the yield stress:

- For $\tau < \tau_o$, the material remains rigid.
- For $\tau > \tau_o$, the material flows as a power-law fluid.

The Herschel-Bulkley model combines the effects of Bingham and power-law behavior in a fluid. For low strain rates ($\dot{\gamma} < \tau_o/\mu_o$), the "rigid" material acts like a very viscous fluid with viscosity, μ_o . As the strain rate increases and the yield stress threshold, τ_o , is passed, the fluid behavior is described by a power law.

$$\eta = \frac{\tau_o + k[\dot{\gamma}^n - (\tau_o/\mu_o)^n]}{\dot{\gamma}} \quad (3.13)$$

Where k is the consistency index and n is the power-law index.

Figure 2.5 below shows how shear stress (τ) varies with shear rate ($\dot{\gamma}$) for the Herschel-Bulkley model.

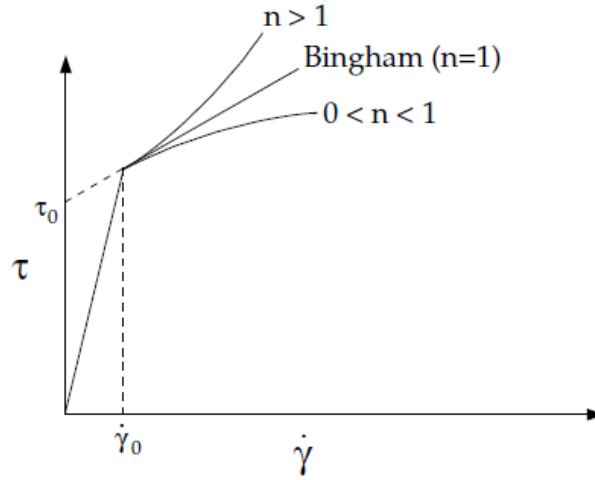


Figure 3.5: Shear stress (τ) varies with shear rate ($\dot{\gamma}$) for the Herschel-Bulkley model. Noting that this model will be adopted for current study [57].

3.5.5 Cross Model

The Cross model for viscosity is

$$\eta = \frac{\eta_o}{1+(\lambda\dot{\gamma})^{1-n}} \quad (3.14)$$

Where η_o = zero-shear-rate viscosity

λ = natural time (i.e., inverse of the shear rate at which the fluid changes from Newtonian to power-law behavior)

n = power-law index

The Cross model is commonly used when it is necessary to describe the low-shear-rate behavior of the viscosity.

3.6 Laminar, transitional and turbulent fluid flow

In fluid mechanics, Reynolds number is usually the criteria to determine whether the flow is in laminar, transient or turbulent phase of flow. For the power flow and Herschel-Bulkley non-Newtonian fluid flow; Reynolds number is defined as the following:

$$Re = \frac{h^n \bar{w}^{(2-n)} \rho}{k} \quad (3.15)$$

Where h is the height of the channel of the micropump, \bar{w} is the average velocity of the moving walls of the pumps, ρ is the density, n is the power law index and k is the consistency factor.

Despite the fact that the fluidic flow in microchannels is almost acting as a laminar flow, scientists did several experiments to determine the range of Reynolds number at which the flow transition from laminar to transitional and then to turbulent occurs. The results of the experiments done by the scientists were varying from one research to another; this variation was a result of the undetectable errors, measurement errors and different surface effects. Several studies found that the fluid flow in different microchannels changes from laminar to transitional phase in Reynolds number ranges between 200-700 and the fully development of turbulent flow occurs with Reynolds number ranges from 400-1500 (Xu et al.,). Other researchers found that the ranges of Reynolds at which the flow goes from laminar to transitional and from transitional to turbulent are the same ranges as in macroscale fluidic flow. In the current study, the flow was investigated and found laminar with Reynolds numbers $\ll 1$.

3.7 Compressible and Incompressible Fluid Flows

Incompressible fluid flows are fluids motion with negligible changes in density. No fluid is truly incompressible, since even liquids can have their density increased through application of sufficient pressure. But density changes in a flow will be negligible if the Mach number, Ma , of the flow is small. This condition for incompressible flow is given by the equation below, where V is the fluid velocity and a is the speed of sound of the fluid. It is nearly impossible to attain $Ma = \frac{V}{a} < 0.3$.

0.3 in liquid flow because of the very high pressures required. Thus liquid flow is incompressible.

3.8 Fully Developed Flow and Entrance Length

When a viscous fluid flows in a duct, a velocity boundary layer develops along the inside surfaces of the duct. The boundary layer fills the entire duct gradually. The region where the velocity profile is developing is called the hydrodynamics entrance region, and its extent is the hydrodynamic entrance length. An estimate of the magnitude of the hydrodynamic entrance length, L_h , in laminar flow in a duct is given by [26]:

$$\frac{L_h}{D_h} = 0.065Re \quad (3.16)$$

The region beyond the entrance region is referred to as the hydrodynamically fully developed region. In this region, the boundary layer completely fills the duct and the velocity profile becomes invariant with the axial coordinate.

3.9 Slip and no Slip Boundary Conditions

The Knudsen number (Kn) is the ratio of the mean free path to the typical device scale. Numerous experiments [27, 28] have determined that noncontinuum effects become observable when Kn reaches approximately 0.1, and continuum equations become meaningless (the “transition flow regime”) at Kn of approximately 0.3. For atmospheric temperature and pressure, the mean free path (of air) is approximately 70 nm. Thus, atmospheric devices with features smaller than approximately 0.2 μm will be subject to nonnegligible, noncontinuum effects. In many cases, such small dimensions are not present, thus the fluidic analysis can safely use the standard Navier–Stokes

equations (as is the case for the microengine). [29]. Table 2.4 below; shows the different flow regimes based on the amount on Knudsen number Kn:

Table3.4: Flow regimes and their flow model based on Knudsen number.

The value of Knudsen number	Flow description	Flow model
$k_n \rightarrow 0$	Continuum with no molecular diffusion	Euler equations
$k_n \leq 10^{-3}$	Continuum with molecular diffusion	Navier-Stokes equations with no-slip boundary conditions
$10^{-3} \leq k_n \leq 10^{-1}$	Continuum - transition	Navier-Stokes equations with slip boundary conditions
$k_n \leq 10$	Transition	Burnett equations with slip boundary conditions , Moment equations, DSMC, Lattice Boltzmann
$k_n > 10$	Free molecular flow	DSMC, Lattice Boltzmann

Noting that the model adopted in this study is the Navier Sstokes equations with no-slip boundary conditions.

3.10 Friction factor

Recently, an enormous number of researches to study the fluid flow in both smooth and rough microchannels were carried out, in order to check the validity of the conventional theory of friction factor when dealing with fluids in microscale and to

discuss the inconsistent published results described the pressure drop, and friction factor in microscale [44, 45, and 46]. In conclusion, the experimental results was found to be in agreement with the conventional theory, when the experimental conditions is consistent with the theoretical ones [47]. A detailed study for the pressure drop in different cross sectional, fully developed, laminar, incompressible, smooth microchannels was developed [48] A compact approximate model as a function of geometrical parameters was proposed, and showed good agreement with the experimental data. The study was carried through a derivation for the Fanning friction factor (f) for different microchannel cross sections using Fanning friction factor equation [2]:

$$f = \frac{\bar{\tau}}{0.5\rho\bar{w}^2} \quad (3.17)$$

Where $\bar{\tau}$ is the mean wall shear stress, ρ is the fluid density and \bar{w} is the fluid mean velocity.

3.11 CFD Simulation Methods

In many cases it is important to obtain quantitative data about physical, technical or other real life systems. One may obtain these through measurements. However, if we have sufficiently accurate mathematical models for a system, we can also try to derive quantitative data from these models. Models for technical problems often take the form of a PDE or a system of PDEs, and although much analytical theory is available for PDEs, most of these equations do not allow an explicit solution in closed form. Therefore numerical methods are used to get insight in their quantitative behavior.

In practice it is clear that there are many restrictions in gathering reliable data from real-life measurements. In the numerical simulation of these systems, limitations of accuracy are caused by possible inaccuracies in the mathematical model, because the

model is often a simplification of reality, and also because there is always a limitation of computing resources.

Numerical mathematics takes the mathematical equations as a starting point and strives for an efficient and accurate approximation of the quantitative data.

Several discretization methods are used to transfer the PDE set of equations into a set of algebraic equations, the most known discretization methods are the finite difference method (FDM), the finite element method (FEM) and the finite volume method (FVM).

In the finite difference method, a grid generation is firstly done in order to discretize the problem domain. This will be followed by substituting the PDE derivatives in the system of PDE equation with the finite difference schemes such as the central finite difference scheme; this will transform the set of PDE equations into a set of algebraic equations. The next step will be solving the set of algebraic equations by implementing these equations into a computer code. A fully detailed example of solving the current problem is shown in the previous chapter.

In the finite element method, the solution approach is based either on eliminating the differential equations completely (steady state problems) and transform them into a system of algebraic equations, or rendering the PDE into an approximating system of ordinary differential equations, which are then numerically integrated using standard techniques such as Runge-Kutta, etc. the main challenge in using the finite element method is to create an equation that approximates the equation to be studied, but is numerically stable, meaning that errors in the input and intermediate calculations do not accumulate and cause the resulting output to be meaningless. There are many ways of doing this, all with advantages and disadvantages.

The finite element method helps tremendously while dealing with structural simulations in producing stiffness and strength visualizations and also in minimizing weight, materials, and costs by allowing a detailed visualization of where structures bend or twist, and indicates the distribution of stresses and displacements. FEM software provides a wide range of simulation options for controlling the complexity of both modeling and analysis of a system. Similarly, the desired level of accuracy required and associated computational time requirements can be managed simultaneously to address most engineering applications. FEM allows entire designs to be constructed, refined, and optimized before the design is manufactured.

The finite volume method is also method for representing and evaluating partial differential equations in the form of algebraic equations .Similar to the finite difference method or finite element method, values are calculated at discrete places on a meshed geometry. "Finite volume" refers to the small volume surrounding each node point on a mesh. In the finite volume method, volume integrals in a partial differential equation that contain a divergence term are converted to surface integrals, using the divergence theorem. These terms are then evaluated as fluxes at the surfaces of each finite volume. Because the flux entering a given volume is identical to that leaving the adjacent volume, these methods are conservative. Another advantage of the finite volume method is that it is easily formulated to allow for unstructured meshes. The finite volume method is used in many computational fluid dynamics packages.

3.12 Introduction to FLUENT Package

FLUENT is one of the many commercial packages available to perform CFD. It is also the most widely used general-purpose CFD software to perform fluid flow and heat transfer analysis of real industrial processes. Its unique capabilities include an

unstructured, finite volume based solver which is near-ideal for parallel performance. Its enhanced features such as complete mesh flexibility, solver capabilities, additional models to simulate the accompanying effects of turbulence, acoustics, heat transfer, species transport, reactions and combustion, dynamic mesh modeling, makes it an ideal choice to perform CFD simulations with. In this section a brief description of the salient features of the FLUENT CFD package is presented.

3.13 SIMPLE algorithm

The SIMPLE algorithm was developed for calculation of the flow field. SIMPLE stands for Semi-Implicit Method for Pressure Linked Equations. The procedure has been described in detail in [53].

The momentum equations can be solved only if the pressure field is given or is somehow estimated. Unless the correct pressure field is not employed, the resulting field will not satisfy the continuity equation. Such an incorrect velocity field derived on a guessed pressure field P^* will be denoted by u^* , v^* (for a two-dimensional case).

The aim of the SIMPLE algorithm is to improve the guessed pressure such that the resulting starred velocity field will progress towards satisfying the continuity equation. Let us assume that the corrected pressure is obtained from the following relation:

$$P = P^* + P' \quad (3.18)$$

Where P' and P^* are the corrected and guessed pressures respectively, the corresponding velocity corrections can be introduced similarly to the velocity components as the following:

$$u = u^* + u' \quad (3.19)$$

$$v = v^* + v' \quad (3.20)$$

Using the discretization equations, it can be shown that the velocity components respond to the pressure correction in the following manner.

$$u_e = u_e^* + \frac{A_e}{a_e} (P'_P - P'_E) \quad (3.21)$$

$$v_n = v_n^* + \frac{A_n}{a_n} (P'_P - P'_N) \quad (3.22)$$

where the subscripts P, E, and N denote the grid points lying next to the control volume faces e and n, a's are the finite difference coefficients, and A represents the area of the control volume face on which the pressure difference acts.

It is now possible to integrate the continuity equation over a typical control volume and obtain the discretized equation for the corrected pressure P' [54].

The sequence of operations in SIMPLE can be represented by the following diagram:

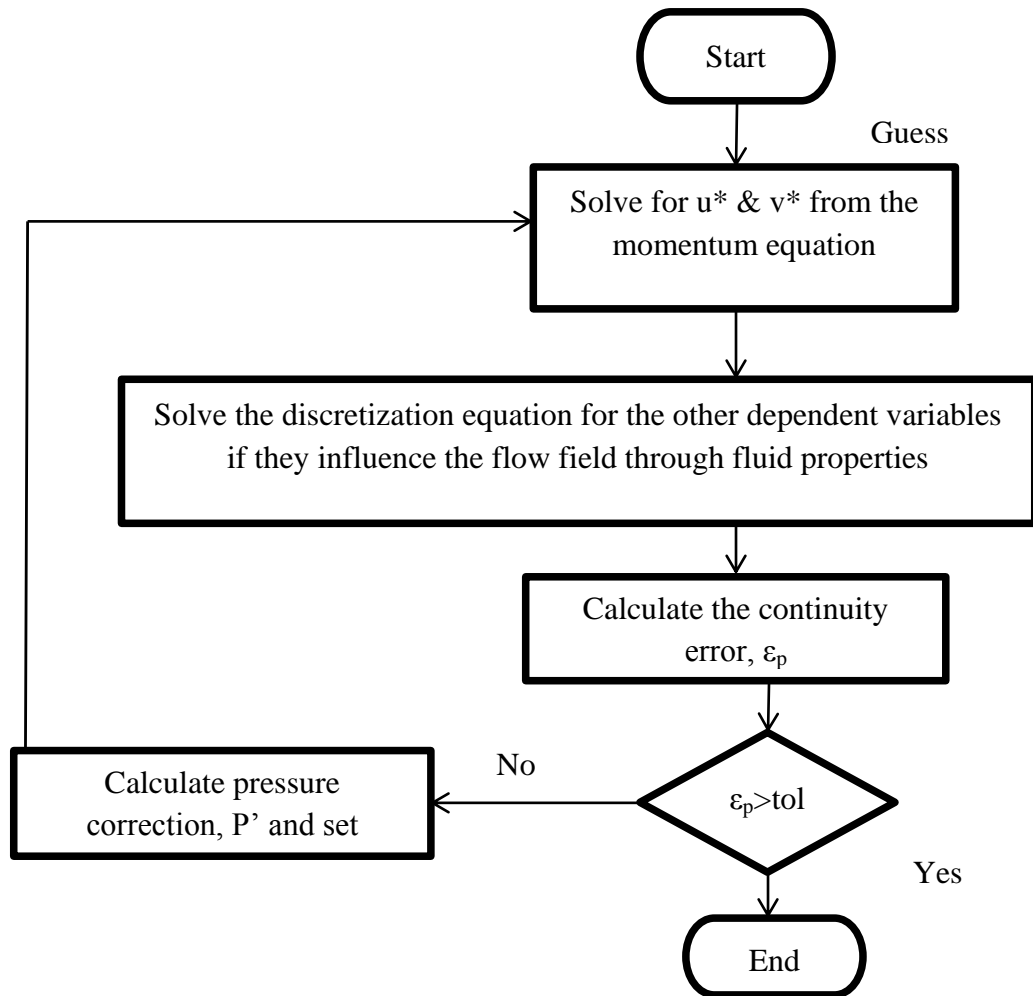


Fig. 3.6: Schematic diagram of the sequence of operations of the SIMPLE algorithm.

3.14 The staggered grid

It is possible to employ a different grid for each dependent variable. In the case of the velocity components, there is a lot to benefit from such a procedure. Such a displaced or "staggered" grid for the velocity components was first used by [92]. This is the basis of the SIMPLE algorithm developed by Patankar and Spalding which is used in FLUENT. In the staggered grid, the velocity components are calculated for the points that lie on the control volume faces.

An immediate consequence of the staggered grid is that the mass flow rates across the control volume faces can be calculated without the interpolation of the relevant velocity component. For a typical control volume, it is easy to see that the discretized continuity equation would contain the differences of adjacent velocity components, and that this would prevent a wavy velocity field from satisfying the continuity equation. In the staggered grid, only reasonable velocity fields would have the possibility of being accepted. The other advantage is that the pressure difference between two adjacent grid points becomes the natural driving force for the velocity component located between these grid points. Thus, non-uniform pressure fields will not be treated as uniform ones.

The above freedom has its own disadvantages. Computer CFD softwares like FLUENT based on the staggered grid approach must carry all the indexing and geometric information about the location of the velocity components and must perform certain tiresome and time consuming interpolations. But the benefits are worth the additional trouble.

The following section describes in detail the interpretation of the staggered grid approach implemented by FLUENT.

3.15 Grid Dependency and Numerical Stability

Grid spacing is of primary importance in any kind of numerical analysis, as the accuracy of the solution will depend upon the choice of the computational grid. Flow features on the scale of the grid spacing or finer than the grid spacing cannot be predicted. The fineness of the grid close to the wall will affect the accuracy with which the shear stress and heat transfer at the wall are predicted. One more cause for error is rapid changes in the grid spacing.

The issue of grid dependency arises out of the attempt to model a continuous phenomenon by keeping track of the flow properties at discrete storage locations (the computational nodes). The finite difference technique requires that the differential equations for continuity, momentum and energy be converted into algebraic or 'difference' equations which can be solved on a computer. In order to be able to do this, one must make assumptions as to how each flow t variable changes between the discrete storage locations generated. The discretization process could employ any number of schemes in order to perform the above interpolation. One approach would be to assume a linear variation in the values of the flow variables between adjacent nodes. This method, though simple is generally unsatisfactory. A better approach is to use the characteristics of the surrounding flow, specifically the relative strength of the convection and diffusion, in order to formulate a more accurate interpolation between the nodes.

Grid dependency arises when the change in a flow variable between nodes exceeds that which can be handled by the discretization scheme used. For example, if a second order scheme is employed, the predicted solution is accurate if the variation of the solution is zero, linear, or quadratic between the nodes. If the variation is more rapid than this, error is induced. This error can be reduced by decreasing the distance between the nodes.

The grid dependency of a solution can be assessed only by resolving the grid to generate a finer mesh. The solution is then compared with the simulation performed using the coarser grid. If the solutions are within the predetermined residuals, then a '**grid-independent**' solution has been obtained.

3.16 Residuals reported by FLUENT

After every iteration during the solution routine, the program FLUENT reports residuals for each of the equation that is being solved. These residuals stand as a measure of the extent to which each equation is satisfied throughout the flow field. FLUENT computes the residuals for each conservation equation by adding up the imbalance in the equation for all the computational cells in the solution domain. This discretized form of the conservation equation In two dimensions for a general variable ϕ_p is as follows:

$$A_p \phi_p = \sum_{All\ nodes} A_{nb} \phi_{nb} \quad (3.23)$$

The coefficients are the finite difference coefficients which combine convection and diffusion through the control volume surrounding the typical grid point P. The non-normalized residual, R, is the imbalance in equation 4.7 integrated over all the computational points P. In other words,

$$R = \sum_{All\ nodes} A_{nb} \phi_{nb} - A_p \phi_p \quad (3.24)$$

In FLUENT, the residuals are normalized by the left-hand side of equation 4.8, summed over the computational nodes:

$$\bar{R} = \frac{\sum_{All\ nodes} A_{nb} \phi_{nb} - A_p \phi_p}{\sum_{All\ nodes} A_p \phi_p} \quad (3.25)$$

FLUENT generally reports normalized residuals unless otherwise requested. If the residuals gradually decrease over a number of iterations, it is assumed that the procedure is close to converging to a solution. As an approximate guide, the residuals

have to fall below $1.0e-06$ for convergence to be achieved to within engineering accuracy.

CHAPTER 4

MATHEMATICAL MODELING

4.1 Introduction

In this chapter Navier-Stokes governing equations will be handled so that a set of assumptions that fit with the behavior and specifications of the current flow are implemented in the Navier-Stokes equations in order to have a simplified form of these equations.

The Herschel-Bulkley non-Newtonian model will be adopted to represent the non-Newtonian nature of blood. This model will also be implemented in Navier-Stokes equations.

As it is completely well known, Navier-Stokes equations don't have implicit equations that governs the pressure variation within the flow, as a result of that one of the pressure-velocity coupling methods will be adopted to encounter the pressure variation in the solution of the current system.

The iterative update of coefficients is adopted to linearize the obtained system of equations. Then, the central finite difference method will be utilized in discretizing linearized governing equations and the domain of solution.

Finally, the mathematical formulation for each of the single disk, double disk and spiral pumps will be illustrated at the end of this chapter.

4.2 Continuity and Navier-Stokes equations

Before proceeding with the Navier Stokes equations, the conditions of the unfolding approximations for single disk, double disk and spiral pumps shall be illustrated [6] in order to have a valid unfolding approximation both of Reynolds number and channel width to radius of curvature ratio shall be small “both conditions are achieved in this study”.

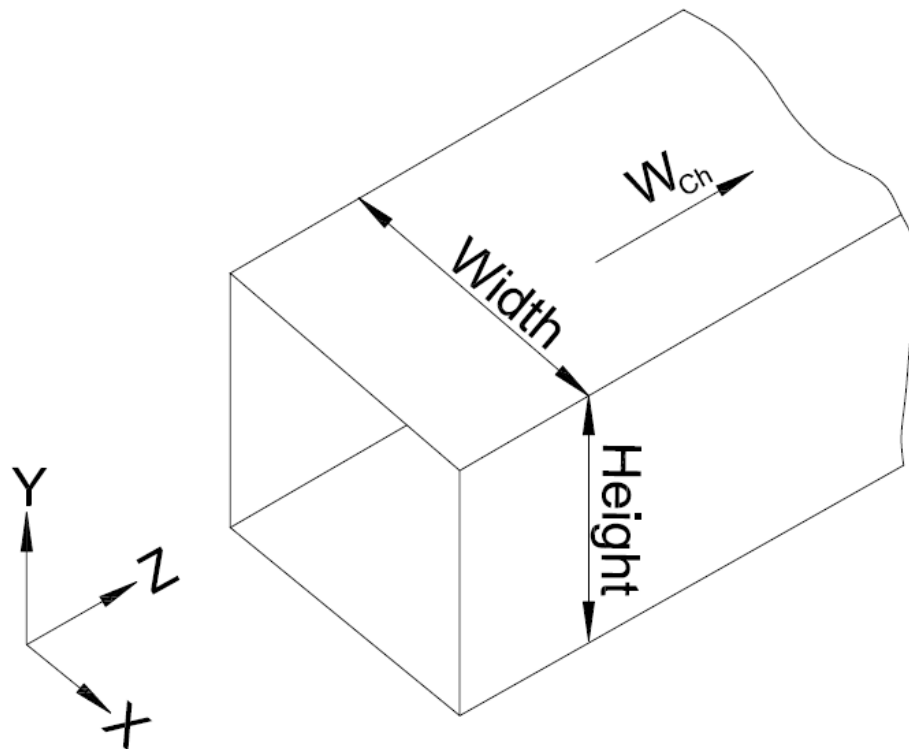


Fig.4.1: The considered geometry for the present work in the unfolding approximation.

As shown the previous chapter, a set of Navier-Stokes equations at which the Bulkley Herschel Non-Newtonian fluid flow model will be considered under certain assumptions to meet the behavior of the current fluid flow. The set of equations that will be used in this study are as the following:

$$\rho \left[\frac{\partial U_i}{\partial t} + U_j \cdot \frac{\partial U_i}{\partial x_j} \right] = - \frac{\partial P}{\partial x_i} + \frac{\partial \tau_{ij}}{\partial x_j} + \rho g_i, \quad i = 1,2,3 \text{ and } j = 1,2,3 \quad (4.1)$$

Where

$$\tau_{ij} = \eta \left[\frac{\partial U_j}{\partial x_i} + \frac{\partial U_i}{\partial x_j} - \frac{2}{3} \delta_{ij} \frac{\partial U_k}{\partial x_k} \right] \quad (4.2)$$

The used assumptions are:

- Steady state flow $\rightarrow \frac{\partial}{\partial t} (\) = 0.0$.
- Fully developed flow $\rightarrow \frac{\partial}{\partial z} (\) = 0.0$.
- Low Reynolds number \rightarrow Inertial term of acceleration = 0.0.
- Bulkley Herschel non-Newtonian fluid flow $\rightarrow \eta = k\dot{\gamma}^{(n-1)} + \frac{\tau_0}{\dot{\gamma}}$.
- Incompressible fluid $\rightarrow \rho = \text{constant}$.
- Negligible gravity forces $\rightarrow g = 0.0$.

Reference to the above assumptions, the set of governing equations of both continuity and momentum equations are resulted as the following:

The continuity equation

$$\frac{\partial u}{\partial x} + \frac{\partial v}{\partial y} = 0.0 \quad (4.3)$$

The z-momentum equation

$$\frac{\partial}{\partial x} \left(\eta \frac{\partial w}{\partial x} \right) + \frac{\partial}{\partial y} \left(\eta \frac{\partial w}{\partial y} \right) - \frac{dP_m}{dz} = 0.0 \quad (4.4)$$

The x-momentum equation

$$\frac{\partial}{\partial x} \left(2\eta \frac{\partial u}{\partial x} \right) + \frac{\partial}{\partial y} \left(\eta \left[\frac{\partial u}{\partial y} + \frac{\partial v}{\partial x} \right] \right) - \frac{\partial P}{\partial x} = 0.0 \quad (4.5)$$

The y-momentum equation

$$\frac{\partial}{\partial x} \left(\eta \left[\frac{\partial u}{\partial y} + \frac{\partial v}{\partial x} \right] \right) + \frac{\partial}{\partial y} \left(2\eta \frac{\partial v}{\partial y} \right) - \frac{\partial P}{\partial y} = 0.0 \quad (4.6)$$

Where η is the apparent dynamic viscosity of Herschel-Bulkley non-Newtonian model and given by

$$\eta = k\dot{\gamma}^{(n-1)} + \frac{\tau_0}{\dot{\gamma}} \quad (4.7)$$

And

$$\dot{\gamma} = \sqrt{2 \left(\frac{\partial u}{\partial x} \right)^2 + 2 \left(\frac{\partial u}{\partial y} \right)^2 + \left(\frac{\partial u}{\partial y} + \frac{\partial v}{\partial x} \right)^2 + \left(\frac{\partial w}{\partial x} \right)^2 + \left(\frac{\partial w}{\partial y} \right)^2} \quad (4.8)$$

It can be easily noted that the pressure term in the momentum equation is divided into two terms: cross sectional mean pressure, $P_m = P_m(z)$ and the in-plan perturbation pressure, $P = P(x,y)$. when taking the fully developed flow into consideration this implies that P_m is varying linearly along the channel length i.e. $\frac{dP_m}{dz}$ is constant and must be an input in order to obtain a closed system of equations. On the other hand the P varies over the cross-section in such a way as to satisfy the continuity equation [51].

For the purpose of numerical solution it is convenient to make the governing equation dimensionless; in the current study the following dimensionless numbers are adopted:

$$x^* = \frac{x}{L}, \quad y^* = \frac{y}{L}, \quad z^* = \frac{z}{L} \quad (4.9, 10 \text{ and } 11)$$

$$u^* = \frac{u}{\bar{w}_{ch}}, \quad v^* = \frac{v}{\bar{w}_{ch}}, \quad w^* = \frac{w}{\bar{w}_{ch}} \quad (4.12, 13 \text{ and } 14)$$

$$P_m^* = \frac{P_m L^n}{k \bar{w}_{ch}^n}, \quad P^* = \frac{P L^n}{k \bar{w}_{ch}^n} \quad (4.15 \text{ and } 16)$$

$$\mu = \frac{\eta L^{(n-1)}}{k \bar{w}_{ch}^{(n-1)}} \quad (4.17)$$

Applying the above mentioned set of dimensionless variables to the continuity, momentum equations and Herschel-Bulkley model equations yields the following:

The continuity equation

$$\frac{\partial u^*}{\partial x^*} + \frac{\partial v^*}{\partial y^*} = 0.0 \quad (4.18)$$

The z-momentum equation

$$\frac{\partial}{\partial x^*} \left(\mu \frac{\partial w^*}{\partial x^*} \right) + \frac{\partial}{\partial y^*} \left(\mu \frac{\partial w^*}{\partial y^*} \right) - \frac{dP_m^*}{dz^*} = 0.0 \quad (4.19)$$

The x-momentum equation

$$\frac{\partial}{\partial x^*} \left(2\mu \frac{\partial u^*}{\partial x^*} \right) + \frac{\partial}{\partial y^*} \left(\mu \left[\frac{\partial u^*}{\partial y^*} + \frac{\partial v^*}{\partial x^*} \right] \right) - \frac{\partial P^*}{\partial x^*} = 0.0 \quad (4.20)$$

The y-momentum equation

$$\frac{\partial}{\partial x^*} \left(\mu \left[\frac{\partial u^*}{\partial y^*} + \frac{\partial v^*}{\partial x^*} \right] \right) + \frac{\partial}{\partial y^*} \left(2\mu \frac{\partial v^*}{\partial y^*} \right) - \frac{\partial P^*}{\partial y^*} = 0.0 \quad (4.21)$$

Herschel-Bulkley model

$$\mu = (\dot{\gamma}^*)^{(n-1)} + \frac{\tau_d}{(\dot{\gamma}^*)} \quad (4.22)$$

Where

$$\dot{\gamma}^* = \sqrt{2 \left(\frac{\partial u^*}{\partial x^*} \right)^2 + 2 \left(\frac{\partial v^*}{\partial y^*} \right)^2 + \left(\frac{\partial u^*}{\partial y^*} + \frac{\partial v^*}{\partial x^*} \right)^2 + \left(\frac{\partial w^*}{\partial x^*} \right)^2 + \left(\frac{\partial w^*}{\partial y^*} \right)^2} \quad (4.23)$$

And

$$\tau_d = \frac{\tau_o}{k(\bar{w}ch/L)^n} \quad (4.24)$$

For the treatment of the in-plane pressure and continuity equations (pressure-velocity coupling) a penalty formulation is adopted for the current study [52]. This approach (i.e. the penalty formulation) has been widely used for the prediction of the incompressible flows. The penalty approach key is replacing the continuity equation by weakened constraint:

$$\frac{\partial u^*}{\partial x^*} + \frac{\partial v^*}{\partial y^*} = \frac{-P^*}{\lambda} \quad (4.25)$$

Where λ is the penalty parameter. λ shall be large enough in order to almost achieve the continuity equation, typical values for λ varies between $10^5 - 10^9$. Pressure term in the penalty formulation is then rearranged be substituted instead of the in-plane perturbation pressure gradients (i.e. $\frac{\partial P^*}{\partial x}$ and $\frac{\partial P^*}{\partial y}$) in both of the transverse momentum equations to obtain the following x and y momentum equations:

The x-momentum equation

$$\frac{\partial}{\partial x^*} \left(2\mu \frac{\partial u^*}{\partial x^*} \right) + \frac{\partial}{\partial y^*} \left(\mu \left[\frac{\partial u^*}{\partial y^*} + \frac{\partial v^*}{\partial x^*} \right] \right) - \frac{\partial}{\partial x^*} \left[\lambda \left(\frac{\partial u^*}{\partial x^*} + \frac{\partial v^*}{\partial y^*} \right) \right] = 0.0 \quad (4.26)$$

The y-momentum equation

$$\frac{\partial}{\partial x^*} \left(\mu \left[\frac{\partial u^*}{\partial y^*} + \frac{\partial v^*}{\partial x^*} \right] \right) + \frac{\partial}{\partial y^*} \left(2\mu \frac{\partial v^*}{\partial y^*} \right) - \frac{\partial}{\partial y^*} \left[\lambda \left(\frac{\partial u^*}{\partial x^*} + \frac{\partial v^*}{\partial y^*} \right) \right] = 0.0 \quad (4.27)$$

At which the longitudinal momentum equation remains unchanged.

In order to linearize the above system of equations, the “simple iterative update of coefficients” method is implemented at which the viscosity coefficients in the above

equations is evaluated at a previous node “lagging coefficients” and then the system is solved for the new values of u^* , v^* and w^* at the next nodal level. The coefficients can then be updated by utilizing the new solution. These calculations are repeated until a preset convergence criteria is obtained. For more details, refer to [56].

In order to discretize both of the linearized governing equations and the domain of the problem; the following central finite difference formulas are adopted:

$$\frac{\partial u_i^*}{\partial x^*} = \frac{u_i^*(i+1,j) - u_i^*(i-1,j)}{2h}, \quad i = 1, 2 \text{ and } 3 \quad (4.28)$$

$$\frac{\partial u_i^*}{\partial y^*} = \frac{u_i^*(i,j+1) - u_i^*(i,j-1)}{2h} \quad (4.29)$$

$$\frac{\partial^2 u_i^*}{\partial x^{*2}} = \frac{u_i^*(i+1,j) - 2u_i^*(i,j) + u_i^*(i-1,j)}{h^2} \quad (4.30)$$

$$\frac{\partial^2 u_i^*}{\partial y^{*2}} = \frac{u_i^*(i,j+1) - 2u_i^*(i,j) + u_i^*(i,j-1)}{h^2} \quad (4.31)$$

Where h is the step size in both x and y directions.

After performing several mathematical manipulations, the resulted governing equations will be as the following:

- The strain rate and apparent viscosity which are calculated one step in advance before calculating the velocity field are defined as the following:

$$\dot{\gamma}^* = \sqrt{\left(2(u^*(i+1,j) - u^*(i-1,j))^2 + 2(v^*(i,j+1) - v^*(i,j-1))^2 + (u^*(i,j+1) - u^*(i,j-1) + v^*(i+1,j) - v^*(i-1,j))^2 + (w^*(i+1,j) - w^*(i-1,j))^2 + (w^*(i,j+1) - w^*(i,j-1))^2 \right)} \quad (4.32)$$

$$\text{And } \mu = \dot{\gamma}^{*(n-1)} + \frac{\tau_d}{\dot{\gamma}^*} \quad (4.33)$$

- The velocity components are represented as the following:

$$w^*(i, j) = \frac{1}{4} (w^*(i+1, j) + w^*(i-1, j) + w^*(i, j+1) + w^*(i, j-1)) - \frac{h^2}{4\mu} \frac{dP_m^*}{dz} \quad (4.34)$$

$$u^*(i, j) = \frac{2\mu+\lambda}{6\mu+2\lambda} (u^*(i+1, j) - u^*(i-1, j)) + \frac{\mu}{6\mu+2\lambda} (u^*(i, j+1) - u^*(i, j-1)) + \frac{\mu+\lambda}{6\mu+2\lambda} (v^*(i+1, j+1) - v^*(i+1, j-1) - v^*(i-1, j+1) + v^*(i-1, j-1)) \quad (4.35)$$

$$v^*(i, j) = \frac{2\mu+\lambda}{6\mu+2\lambda} (v^*(i, j+1) - v^*(i, j-1)) + \frac{\mu}{6\mu+2\lambda} (v^*(i+1, j) - v^*(i-1, j)) + \frac{\mu+\lambda}{6\mu+2\lambda} (u^*(i+1, j+1) - u^*(i+1, j-1) - u^*(i-1, j+1) + u^*(i-1, j-1)) \quad (4.36)$$

Finally, the finite difference discretized equations side by side with the boundary conditions for each type of pumps (this will be illustrated in the following sections) where solved using Matlab.

4.3 Mathematical Formulation:

This section will present the mathematical formulation of the single disk, double disk and spiral channel micropumps and their dedicated boundary conditions as the following:

4.3.1 Single Disk Micropumps

The previously derived set of finite difference equations is adopted with having the upper wall of the channel moving i.e. the governing equations for the single disk micropumps are:

The strain rate and apparent viscosity which are calculated one step in advance before calculating the velocity field are defined as the following:

$$\dot{\gamma}^* = \sqrt{\left(\begin{aligned} &2(u^*(i+1, j) - u^*(i-1, j))^2 + 2(v^*(i, j+1) - v^*(i, j-1))^2 + \\ &(u^*(i, j+1) - u^*(i, j-1) + v^*(i+1, j) - v^*(i-1, j))^2 + \\ &(w^*(i+1, j) - w^*(i-1, j))^2 + (w^*(i, j+1) - w^*(i, j-1))^2 \end{aligned} \right)} \quad (4.37)$$

$$\text{And } \mu = \dot{\gamma}^{*(n-1)} + \frac{\tau_d}{\dot{\gamma}^*} \quad (4.38)$$

The velocity components are represented as the following:

$$w^*(i, j) = \frac{1}{4}(w^*(i+1, j) + w^*(i-1, j) + w^*(i, j+1) + w^*(i, j-1)) - \frac{h^2}{4\mu} \frac{dP_m^*}{dz} \quad (4.39)$$

$$\begin{aligned} u^*(i, j) &= \frac{2\mu+\lambda}{6\mu+2\lambda}(u^*(i+1, j) - u^*(i-1, j)) + \frac{\mu}{6\mu+2\lambda}(u^*(i, j+1) - u^*(i, j-1)) + \\ &\frac{\mu+\lambda}{6\mu+2\lambda}(v^*(i+1, j+1) - v^*(i+1, j-1) - v^*(i-1, j+1) + v^*(i-1, j-1)) \end{aligned} \quad (4.40)$$

$$\begin{aligned} v^*(i, j) &= \frac{2\mu+\lambda}{6\mu+2\lambda}(v^*(i, j+1) - v^*(i, j-1)) + \frac{\mu}{6\mu+2\lambda}(v^*(i+1, j) - v^*(i-1, j)) + \\ &\frac{\mu+\lambda}{6\mu+2\lambda}(u^*(i+1, j+1) - u^*(i+1, j-1) - u^*(i-1, j+1) + u^*(i-1, j-1)) \end{aligned} \quad (4.41)$$

With the following boundary conditions in the dimensionless format:

No slip conditions:

$$w^*(0, y^*) = w^*(L, y^*) = w^*(x^*, 0) = 0 \quad (4.42)$$

Moving upper wall

$$w^*(x^*, \alpha) = 1 \quad (4.43)$$

Impermeable walls

$$u^*(0, y^*) = u^*(L, y^*) = u^*(x^*, 0) = u^*(x^*, \alpha) = 0 \quad (4.44)$$

$$v^*(0, y^*) = v^*(L, y^*) = v^*(x^*, 0) = v^*(x^*, \alpha) = 0 \quad (4.45)$$

4.3.2 Double Disk Micropumps

Here both of the top and bottom walls are rotating in the same direction while keeping the side walls stationary, the resulting equations and boundary conditions are as the following

The strain rate and apparent viscosity which are calculated one step in advance before calculating the velocity field:

$$\dot{\gamma}^* = \sqrt{\left(\begin{array}{l} 2(u^*(i+1, j) - u^*(i-1, j))^2 + 2(v^*(i, j+1) - v^*(i, j-1))^2 + \\ (u^*(i, j+1) - u^*(i, j-1) + v^*(i+1, j) - v^*(i-1, j))^2 + \\ (w^*(i+1, j) - w^*(i-1, j))^2 + (w^*(i, j+1) - w^*(i, j-1))^2 \end{array} \right)} \quad (4.46)$$

$$\text{And } \mu = \dot{\gamma}^{*(n-1)} + \frac{\tau_d}{\dot{\gamma}^*} \quad (4.47)$$

The velocity components are represented as the following:

$$w^*(i, j) = \frac{1}{4}(w^*(i+1, j) + w^*(i-1, j) + w^*(i, j+1) + w^*(i, j-1)) - \frac{h^2}{4\mu} \frac{dP_m^*}{dz} \quad (4.48)$$

$$u^*(i, j) = \frac{2\mu+\lambda}{6\mu+2\lambda}(u^*(i+1, j) - u^*(i-1, j)) + \frac{\mu}{6\mu+2\lambda}(u^*(i, j+1) - u^*(i, j-1)) + \frac{\mu+\lambda}{6\mu+2\lambda}(v^*(i+1, j+1) - v^*(i+1, j-1) - v^*(i-1, j+1) + v^*(i-1, j-1)) \quad (4.49)$$

$$v^*(i, j) = \frac{2\mu+\lambda}{6\mu+2\lambda}(v^*(i, j+1) - v^*(i, j-1)) + \frac{\mu}{6\mu+2\lambda}(v^*(i+1, j) - v^*(i-1, j)) + \frac{\mu+\lambda}{6\mu+2\lambda}(u^*(i+1, j+1) - u^*(i+1, j-1) - u^*(i-1, j+1) + u^*(i-1, j-1)) \quad (4.50)$$

With the following boundary conditions in the dimensionless format:

No slip conditions:

$$w^*(0, y^*) = w^*(L, y^*) = 0 \quad (4.51)$$

Moving top and bottom walls

$$w^*(x^*, 0) = w^*(x^*, \alpha) = 1 \quad (4.52)$$

Impermeable walls

$$u^*(0, y^*) = u^*(L, y^*) = u^*(x^*, 0) = u^*(x^*, \alpha) = 0 \quad (4.53)$$

$$v^*(0, y^*) = v^*(L, y^*) = v^*(x^*, 0) = v^*(x^*, \alpha) = 0 \quad (4.54)$$

4.3.3 Spiral Channel Micropumps

In the spiral pump the top wall with the two side walls are proposed to be moving while keeping the bottom stationary, the resulting equations and boundary conditions are as the following

The strain rate and apparent viscosity which are calculated one step in advance before calculating the velocity field:

$$\dot{\gamma}^* = \sqrt{\left(\begin{array}{l} 2(u^*(i+1, j) - u^*(i-1, j))^2 + 2(v^*(i, j+1) - v^*(i, j-1))^2 + \\ (u^*(i, j+1) - u^*(i, j-1) + v^*(i+1, j) - v^*(i-1, j))^2 + \\ (w^*(i+1, j) - w^*(i-1, j))^2 + (w^*(i, j+1) - w^*(i, j-1))^2 \end{array} \right)} \quad (4.55)$$

$$\text{And } \mu = \dot{\gamma}^{*(n-1)} + \frac{\tau_d}{\dot{\gamma}^*} \quad (4.56)$$

The velocity components are represented as the following:

$$w^*(i, j) = \frac{1}{4} (w^*(i+1, j) + w^*(i-1, j) + w^*(i, j+1) + w^*(i, j-1)) - \frac{h^2}{4\mu} \frac{dP_m^*}{dz} \quad (4.57)$$

$$u^*(i, j) = \frac{2\mu+\lambda}{6\mu+2\lambda} (u^*(i+1, j) - u^*(i-1, j)) + \frac{\mu}{6\mu+2\lambda} (u^*(i, j+1) - u^*(i, j-1)) + \frac{\mu+\lambda}{6\mu+2\lambda} (v^*(i+1, j+1) - v^*(i+1, j-1) - v^*(i-1, j+1) + v^*(i-1, j-1)) \quad (4.58)$$

$$v^*(i, j) = \frac{2\mu+\lambda}{6\mu+2\lambda} (v^*(i, j+1) - v^*(i, j-1)) + \frac{\mu}{6\mu+2\lambda} (v^*(i+1, j) - v^*(i-1, j)) + \frac{\mu+\lambda}{6\mu+2\lambda} (u^*(i+1, j+1) - u^*(i+1, j-1) - u^*(i-1, j+1) + u^*(i-1, j-1)) \quad (4.59)$$

With the following boundary conditions in the dimensionless format:

No slip conditions:

$$w^*(x^*, 0) = 0 \quad (4.60)$$

Moving walls

$$w^*(0, y^*) = w^*(L, y^*) = w^*(x^*, \alpha) = 1 \quad (4.61)$$

Impermeable walls

$$u^*(0, y^*) = u^*(L, y^*) = u^*(x^*, 0) = u^*(x^*, \alpha) = 0 \quad (4.62)$$

$$v^*(0, y^*) = v^*(L, y^*) = v^*(x^*, 0) = v^*(x^*, \alpha) = 0 \quad (4.63)$$

Last, a grid optimization for the created program is done in order to obtain the mesh independent solution; more details are in chapter six “results and discussion”.

CHAPTER 5

Experimental Investigations, Operations and Results: Spiral Micropump

5.1. Introduction

This chapter will illustrate the manufacturing process, operation and setup testing for two spiral micropumps that were used in this work. The main goal of this work is to verify the validity of the numerical solution made for the current study. This is done by using two micropumps with different aspect ratios that were operated with two different working fluids the first fluid was the distilled water while a blood mimicking fluid was used to simulate the blood flow in the second fluid, extra details about the blood mimicking fluid will be shown in the following sections. At the end of this chapter, the experimental result for the two spiral channel micropumps will be shown for the two used fluids. Furthermore, a comparison of the experimental results using the distilled water with the analytical solution [8] will be illustrated and the reasons due to the deviation between them will be discussed.

5.2. Spiral Micropump Manufacturing Process (SU-8 UV Lithography)

From a light source light is directed through a mask carrying the circuit design down onto the substrate wafer covered with a photo-sensitive film, called the photoresist. Depending on the local photo-exposure defined by the photolithographic mask the photoresist can be partly removed by a chemical developer leaving well-defined parts of the substrate wafer exposed to etching or metal deposition.

The substrate wafer is typically a ceramic wafer disk with a thickness around 500 μm and diameter of 100 mm (a 4 inch wafer). Wafers of different purities are purchased at various manufacturers.

The procedure of the SU-8 (which is a negative photoresist) fabrication process adopted to produce the spiral micro pump channel is as the following:

The fabrication process begins with a sacrificial layer of 3 nm Cr and 10 μm Cu deposited onto the substrate (Fig. 5.1, I). According to the required structure height, multilayer of SU-8 can then be deposited. The base layer of SU-8 is spun on the ceramic substrate, dried, exposed totally, and then post exposure baked (PEB) for 45 minutes using ramped temperature 60-95 oC (Fig.5.1, II).

The spiral protrusion layer is fabricated by spinning a new layer of SU-8 above the first exposed one, and then dried, exposed to UV light under the spiral mask, and PEB (Fig. 5.1, III).

After that the SU-8 layers were developed in 4-hydroxybutyric acid lactone used as pre-developer and 1-methoxy-2-propylacetat to remove the unexposed material, and the sacrificial layer is etched and the SU-8 patterns are removed (Fig. 5.1, IV). The fabricated SU-8 patterns are of 380 μm channel height, and 100-1200 μm widths[53].

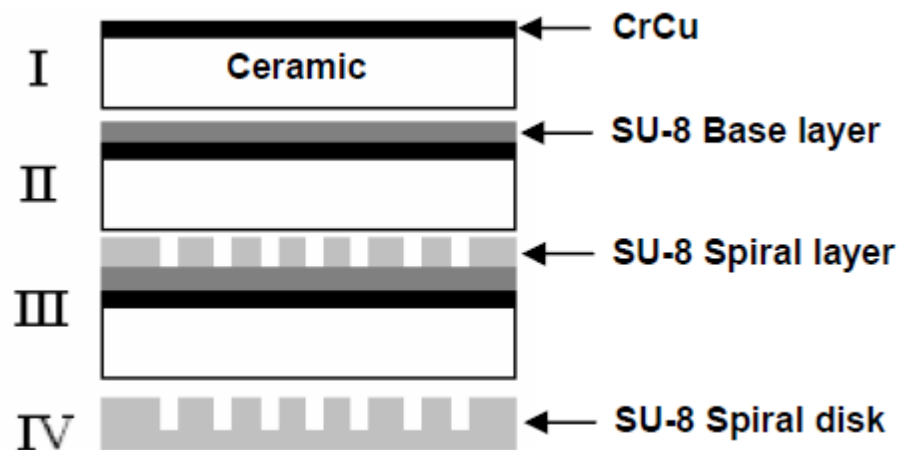


Fig. 5.1: Fabrication procedure of SU-8 using UV depth lithography [54].

The final shape of the spiral channel disk will be as the following:



Fig 5.2: The final shape of the spiral channel silicon disk

5.3. Spiral Pump Configuration and Operation

The spiral channel viscous pump is consisting mainly from two components: a stationary disk and a spinning spiral channel disk that presents the pump chamber side

by side with the fluid inlet and outlet ports that are located at center of the stationary disk and one of the quarters on the side wall of the stationary disk respectively.

The stationary disk shall be very close to the moving of the spiral channel in order to produce a small gap that will result minimizing leakage from the pump chamber.

In the absence of the external pressure produced by increasing the height of the discharge reservoir, the rotating spiral channel disk creates a drag force which moves fluid in a Couette flow pattern between the and the outlet of the spiral channel due to viscous interactions between the fluid and the walls of the channel. If the external pressure is produced, a pressure gradient along the channel axis will form such that the pressure difference between channel inlet and channel outlet is equal to the imposed external pressure. This static pressure then opposes the motion induced by the channel rotation, and a rotating Poiseuille-Couette flow is induced in the fluid inside the channel. If the opposing axial static pressure is large enough, some of the fluid in the spiral channel will recirculate in the opposite direction of the channel rotation. If the fluid outlet port is closed, the net flow is zero, but there will be some fluid movement inside the channel, and the maximum pressure rise between the inlet and the outlet of the channel is generated [2].

5.4. Spiral Pump Setup and Testing

The following devices and instruments have been used for the setup of the experiments carried out in this work:

1. A variable power source as shown in figure 5.3, at which a variable input voltage is delivered to the D.C. current micro-motor so that we can change the rotational speed of the motor.



Fig 5.3: The used variable power source in the present experiment.

2. An analogue oscilloscope as shown in figure 5.4, this oscilloscope is used to find the time needed for the motor to perform one cycle, after that the rotational speed of the motor and the pump can be figured out.

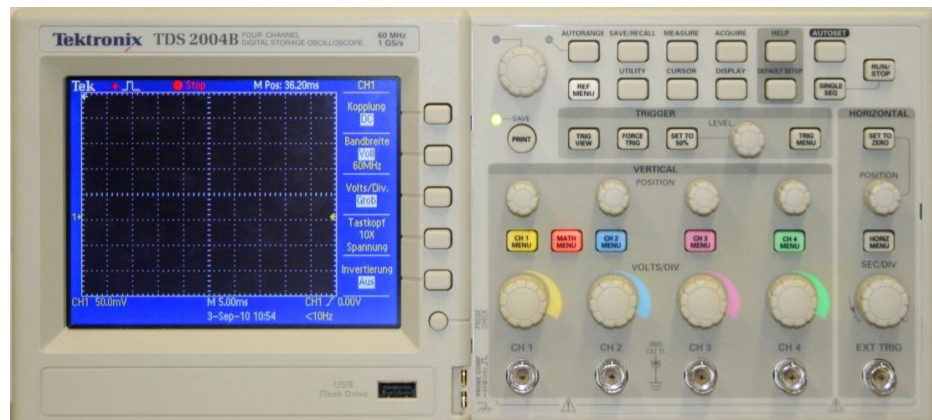


Fig 5.4: The used analogue oscilloscope in the present experiment.

3. A D.C. current micro-motor: this D.C. current micro-motor is Faulhaber 3257G 012CR which is coupled to the spiral channel shaft in order to force the spiral channel disk to rotate.
4. Two spiral channel micropumps: two spiral channel micropumps were investigated by using both distilled water and blood mimicking fluids. Extra details will be presented in the following paragraphs.
5. A steel base to assemble the micro-motor to the spiral microchannel on.
6. A digital scale as shown in figure 5.5, at which the digital scale measures the mass of the conveyed fluid from the input tank (i.e. the reservoir) to the output tank (i.e. filling tank).

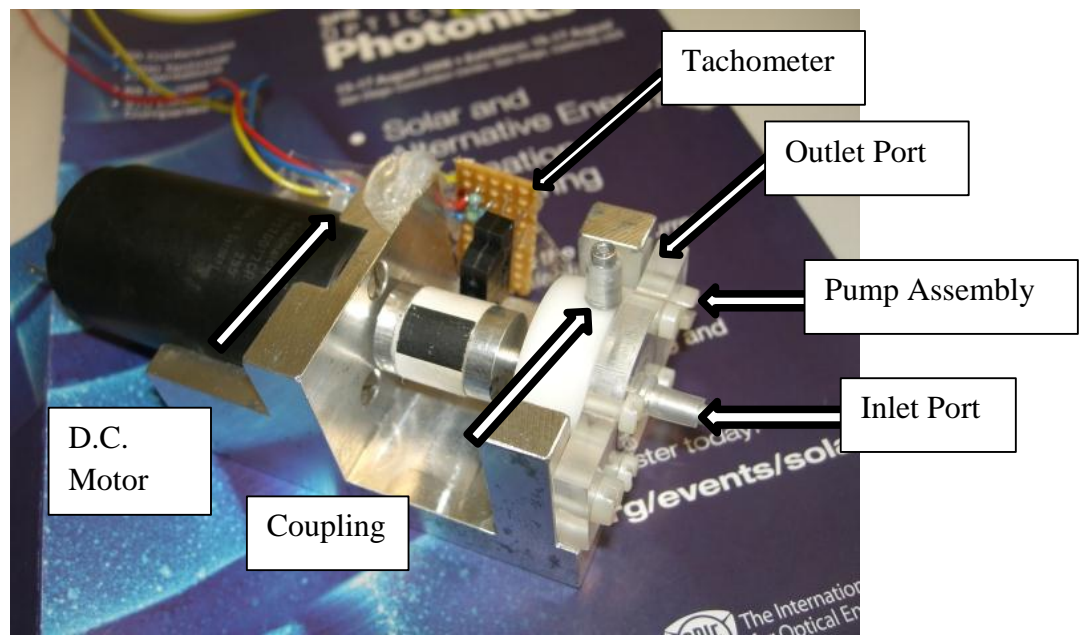


Fig 5.5: The digital scale used in the present experiment.

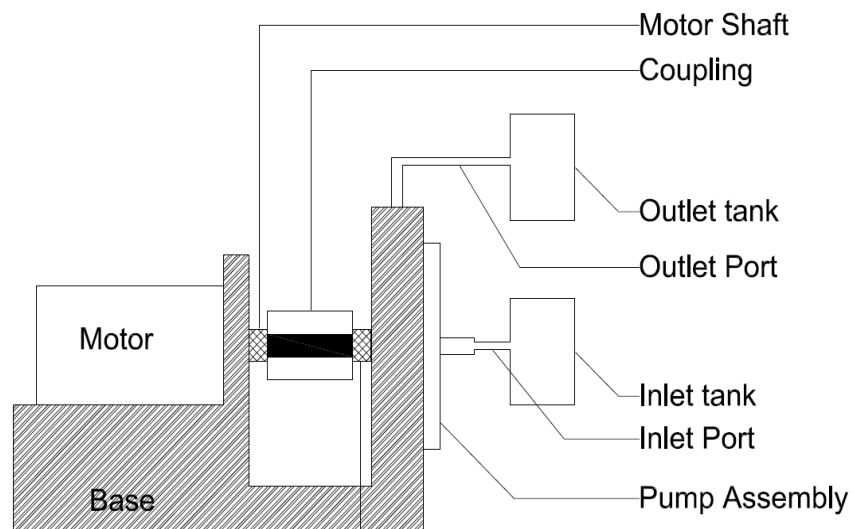
7. Tachometer: this tachometer is used to transform the white and black colors to a digital signal that is then transformed to the oscilloscope; accordingly the rotational speed of the coupling will be shown as a sinusoidal signal on the oscilloscope.

8. Two laboratory cups, these two cups have been used as the reservoir and the filling tank.
9. Stop watch: the stop watch has been used to measure the time needed for a the fluid to be delivered to the filling tank.
10. Wirings: the several wires have been used to connect the D.C. micro-motor to the variable power source and also to connect the tachometer to the analogue oscilloscope.
11. Rubber tubes: to connect between the reservoir and the input port of the micropump from one side and to connect from the output port of the micropump and the filling tank from the other side.
12. Two working fluid media: the first one is an ordinary distilled water to be used as a well-known Newtonian fluid and a blood mimicking fluid to be used as a non-Newtonian fluid.

Figure 5.6 shows the setup adopted for the spiral pump in the present work. The setup is consisting from: A Faulhaber 3257G 012CR DC micro-motor from the motor that is connected to the spiral micropump through a white and black colored coupling. A coupling that has three black strips and other three white strips ordered as black-white-black... This coloring scheme is so important to measure the rotational speed of the motor through connecting a tachometer to an analogue oscilloscope. The micropump case is connected to the inlet tank from the center of its case from one side and to the outlet tank from one of the case quarters from the other side. A digital scale is used to weigh the amount of fluid transported to the outlet tank. And a stop watch to measure the time needed for the fluid to move from the inlet tank to the outlet.



(a)



(b)

Fig. 5.6: Setup adopted for the current spiral micropump side. (a). an exact photo for the spiral channel micropump and the D.C. micromotor connected to each other. (b). a diagram that shows the pump setup.

The obtained spiral micropump disk is first mounted to a metal shaft using a small amount of silicon. Then a digital microscope is used to insure that the spiral channel disk is exactly located at the center of the metal disk and has no eccentricity

also microscope is used to insure that no silicon extra amounts are existing side by side measuring the width of the spiral micropump. Then the spiral micropump is lift for one day to have the bonds between the silicon micropump and the metal disk strong enough to withstand the loads exerted on the spiral micropump by the working fluid while operating. In the second day, the spiral micropump is assembled to its case to have the pump side complete, then the inlet and outlet ports are connected to the inlet and outlet tanks through 2.5mm diameter flexible rubber tubes.

From the other side of the present setup the motor is connected to a variable input power source at which the motor input power is increased and decreased through changing the magnitude of the voltage, as a result of changing the input power the motor speed was changing. In order to measure the motor speed, the coupling between the motor shaft and the pump shaft was colored in white and black as mentioned above and then a tachometer was just directed to that coupling and then connecting to and oscilloscope. In order to measure the rotational speed if the motor the sinusoidal signal observed on the oscilloscope is analyzed as the following: after refining the oscilloscope view a number of six cycles is determined (this is due to the six white and black colors on the coupling) and then figuring out number of squares, n at which these six cycles are encountered in. after that the time at which each square is representing is recorded, t_s . By this, the time needed for the motor to rotate in 360° can be measured. Consequently the rotational speed can be figured out. The equation below gives the formula at which the rotational speed of the motor is determined:

$$\omega = \frac{60}{n \times t_s} \quad (5.1)$$

After that the weight of the outlet tank is measured using the digital scale then the pump is operated. After each certain period of time the pump is stopped and then the outlet tank weight is measured. The difference in weight at each time represents the amount of fluid had been pumped to the outlet tank. By measuring the time needed to encounter the above mentioned pumped fluid using a digital stop watch; the mass flow rate can easily be calculated. This process is done five times for each run, and then the average mass flow rate is calculated.

5.5 Blood Mimicking Fluid

Due to the difficulties to attain human blood to make the experimental results on, and also due to the properties that might differ from one blood package to another and due to the difficulties of storing and dealing with the natural human blood; a blood mimicking fluid is used.

A “concentrated doppler fluid” that is produced, tested and certified by the Danish Phantom Design Company is brought to run the blood experiments on as a blood mimicking fluid. The concentrated Doppler fluid consists from the constituents represented in the table 5.1:

Table 5.1: The constituents of the used blood mimicking fluid

Name	Case No.	Content	Symbol
<u>Glycerol</u>	8043-29-6	<15%	C3H5(OH)3
<u>Triton X-100</u>	9002-93-1	<2%	C34H36O11
<u>Orgasol</u>		10%	Polyamide-12
<u>NaBenoat</u>	132-677--2	1%	C18H12NO3*Na
<u>Na2EDTA</u>	6381-92-6	0.5%	C10H14N2Na2O8

In order to use the above mentioned concentrated Doppler fluid, the fluid shall be shaken well for about five to ten minutes one day before using it, then in the day after that a gentle shaking is made on the fluid until the fluid become homogeneous and all suspended particles distributed well.

5.6 Flow rate experimental results:

In this section, two microscale spiral channel pumps were tested with both distilled water and blood mimicking material. The dimensions of the two spiral channels were as the following:

Table 5.2: The dimensions of the two tested spiral channel pumps.

	Channel 1	Channel 2
Channel width [μm]	400	500
Channel average radius [μm]	1650	1650
Channel angle [rad.]	2π	2π
Channel height [μm]	800	800
Channel length [μm]	10367.26	10367.26

The obtained results show a good agreement between the theoretical and experimental results in behavior although that the experimental results are less in magnitude than the theoretical results due to the losses encountered in the experimental work and the human and instrumental errors as described in chapter five. The results were as the following:

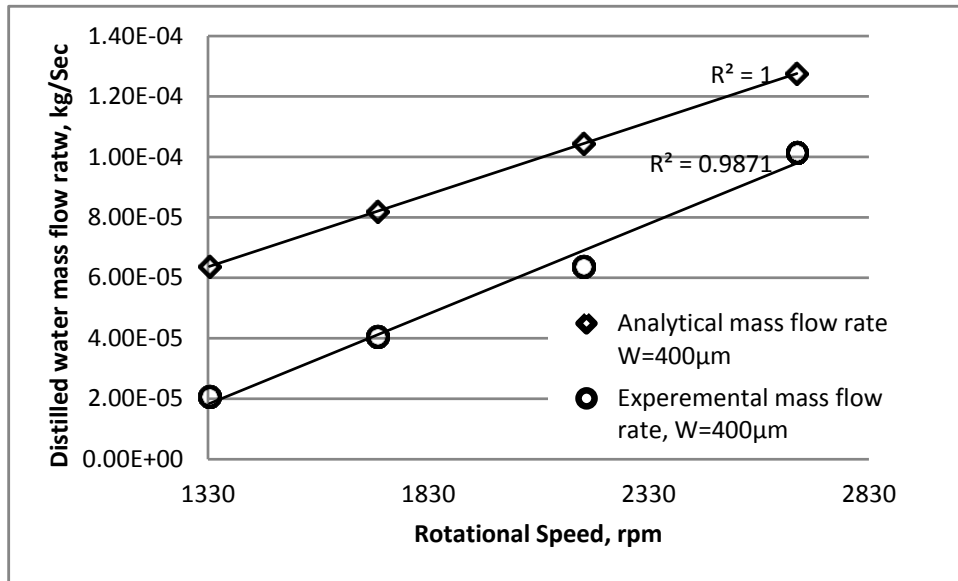


Fig. 5.7: Comparison between the analytical and experimental results for distilled water flow in the first spiral channel pump.

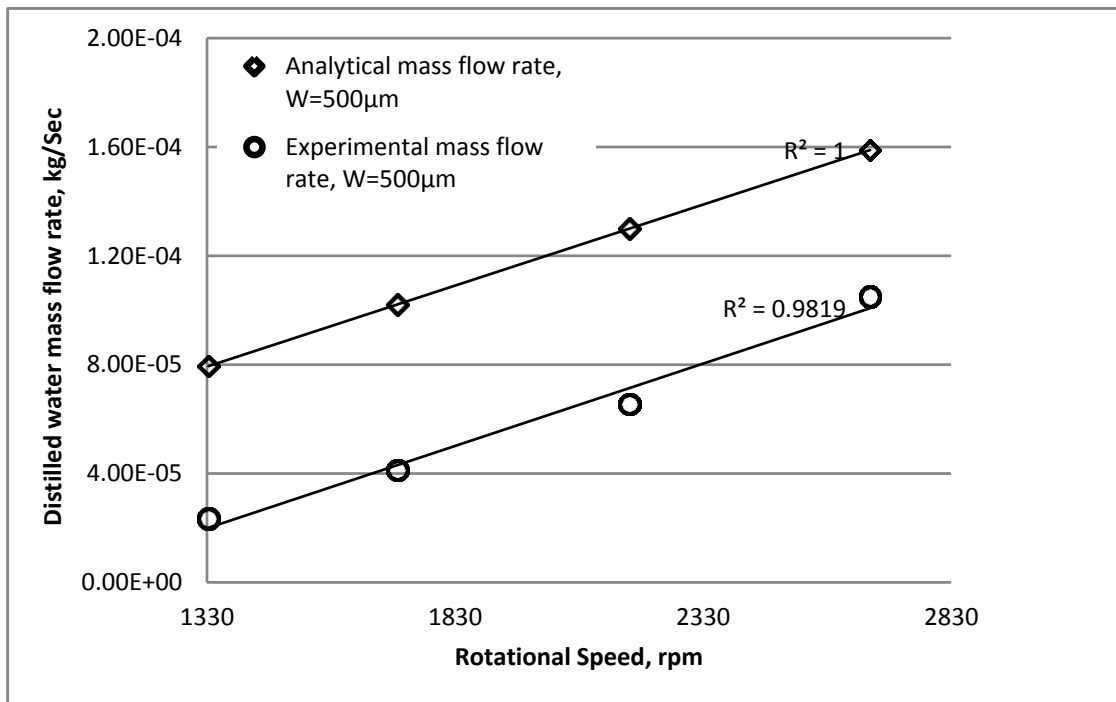


Fig. 5.8: Comparison between the analytical and experimental results for second spiral channel pump.

In figures 5.7 and 5.8 distilled water was used as a Newtonian working fluid, a large deviation between the analytical solution and the experimental results were observed, this deviation occurred due to the effect of viscous dissipation, to the effect of the cross flow in gap below the spiral wall. This cross flow is proportional to the net pressure difference between the inlet and the outlet ports i.e. the cross flow increases as the above indicated pressure difference increases. Another reason to the observed deviation of the experimental results from the analytical is that the fluid losses from the bearing side of the micropump the matter that will result the fact that some of the inlet amount of water will not go to the filling reservoir.

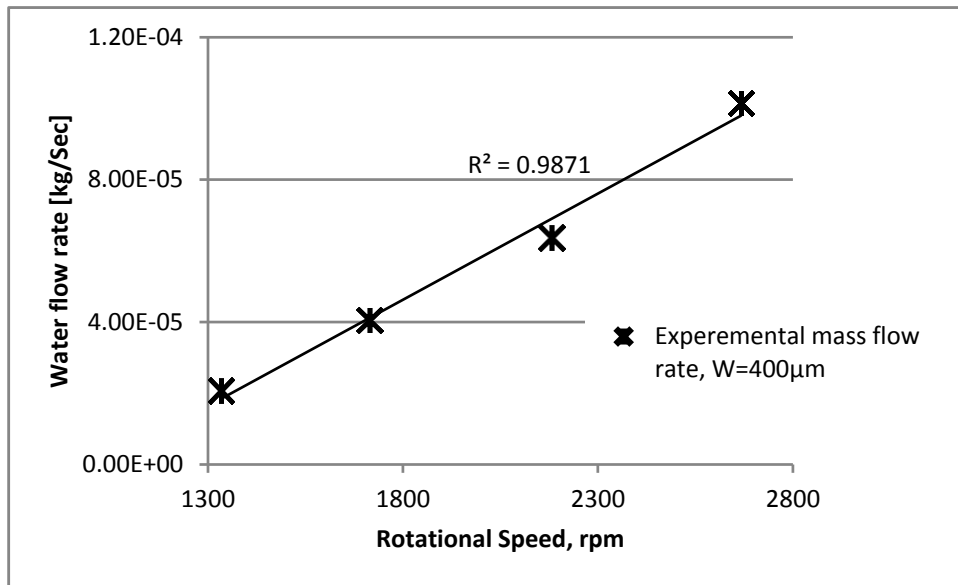


Fig. 5.9: Pump water flow rate .vs. rotational speed of first spiral micropump.

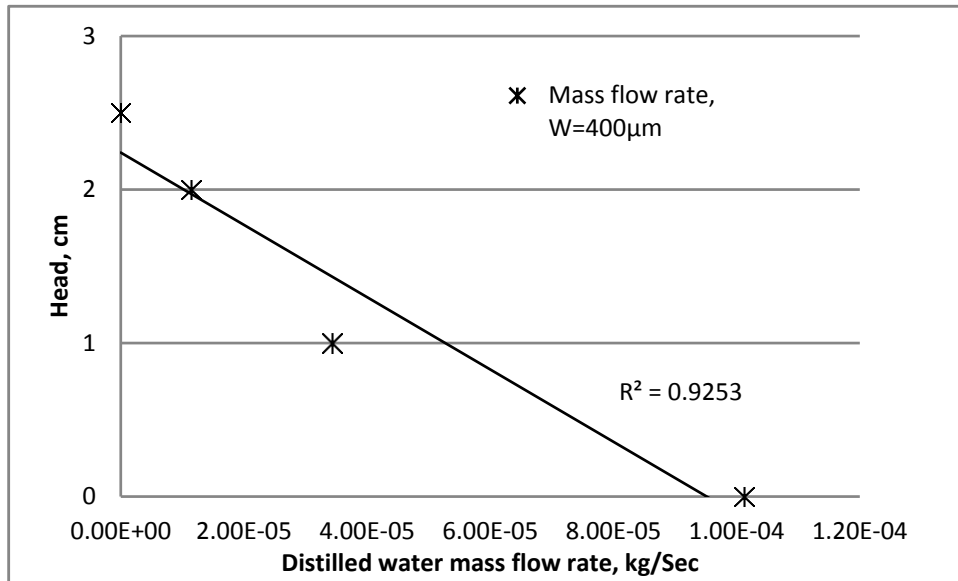


Fig. 5.10: Pump head vs. water mass flow rate for the first spiral micropump.

In figures 5.9 and 5.10 the characteristic curves of the 400 μm wide spiral pump are presented. In figure 5.9 the water flow rate is drawn versus the pump rotational speed. The results were in a good linearity as expected to have as the R-squared value is 0.987 the issue that implies that the measured mass flow rate has a good linearity with the rotational speed of the micropump. The linearity is also observed in figure 5.10 at which the pump head versus the water flow rate is shown but with a less R-squared value.

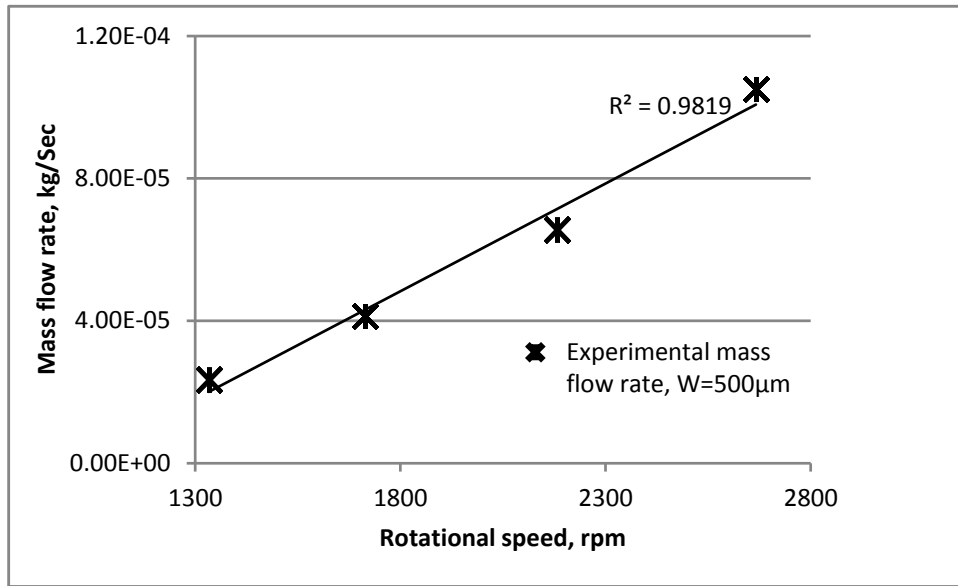


Fig. 5.11: Pump water flow rate .vs. rotational speed of second spiral micropump.

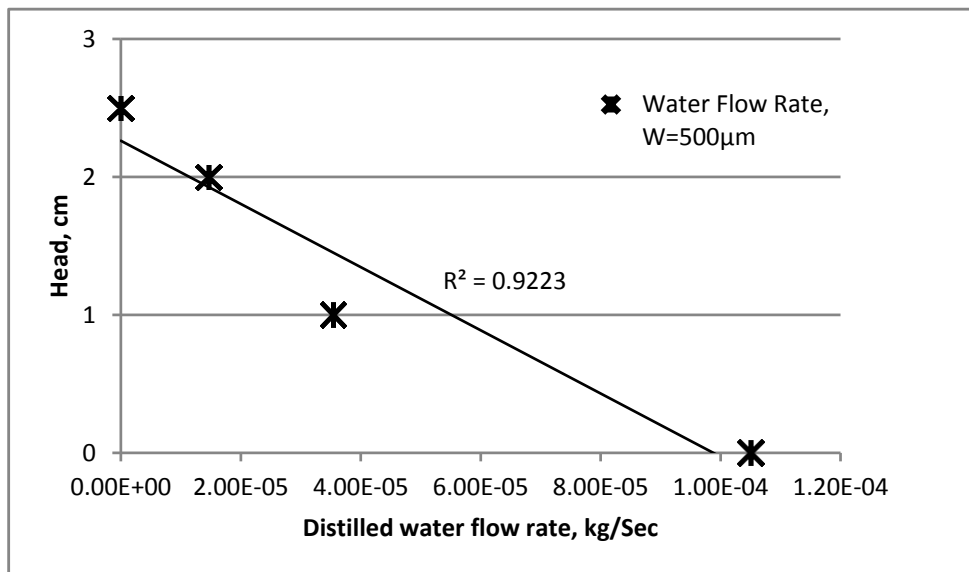


Fig. 5.12: Pump head vs. water mass flow rate for the second spiral micropump.

In figures 5.11 and 5.12 the characteristic curves of the 500 μm wide spiral pump are presented. In figure 5.11 the water flow rate is drawn versus the pump rotational speed. The results were also in a good linearity as expected to have as the R-squared value is 0.9819 the issue that implies that the measured mass flow rate has a good

linearity with the rotational speed of the micropump. The linearity is also observed in figure 5.12 at which the pump head versus the water flow rate is shown but with a R-squared value of 0.9223.

While comparing the two spiral microchannels having the distilled water as working fluid; it is noticed that the second micropump with the 500 μm channel width has values of flow rate higher than that of the 400 μm . This higher values are expected as this increase in width will increase higher aspect ratio and consequently higher flow rate.

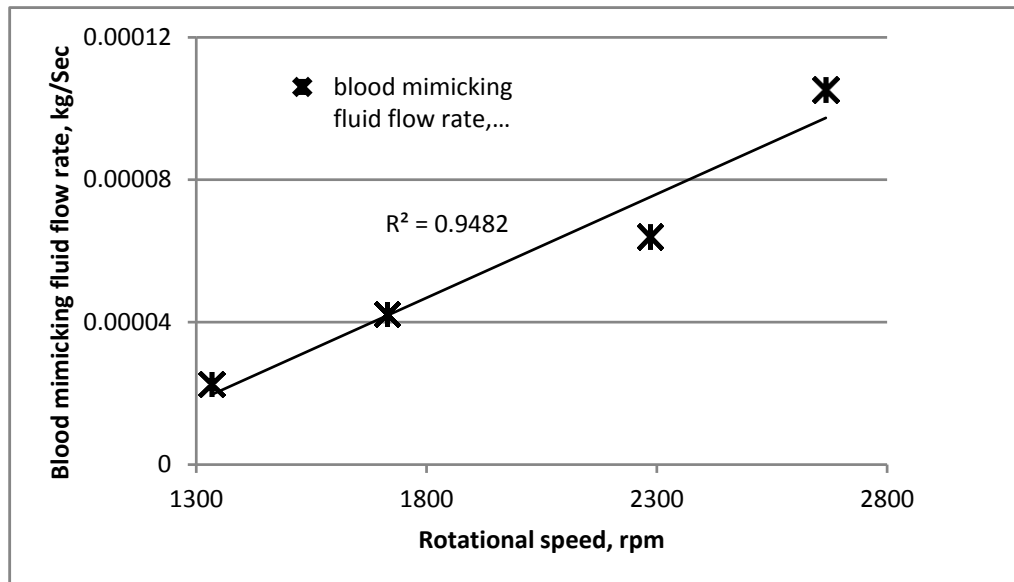


Fig. 5.13: Mass flow rate .vs. rotational speed of the micropump for the blood mimicking fluid operated in the first spiral micropump.

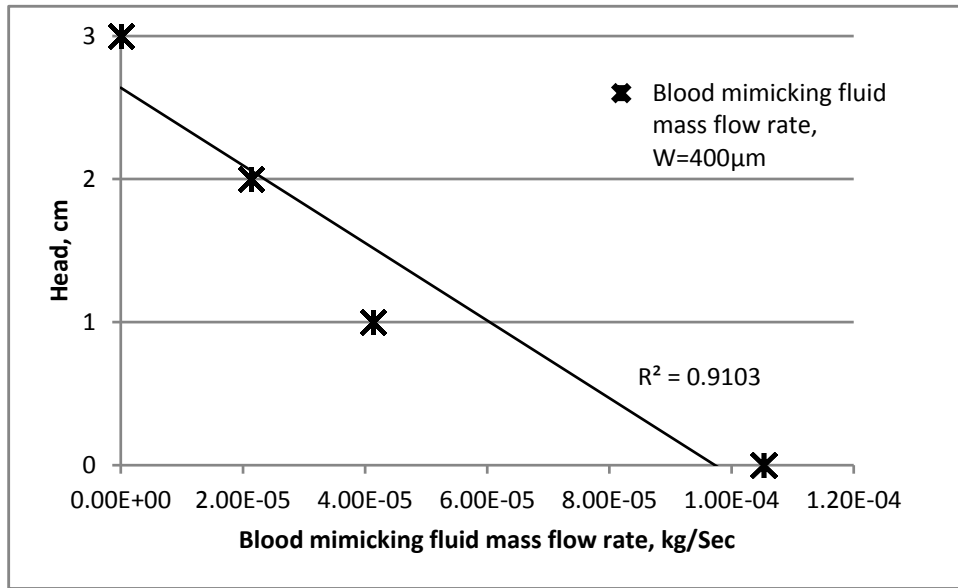


Fig. 5.14: Pump head .vs. mass flow rate of the micropump for the blood mimicking fluid operated in the first spiral micropump.

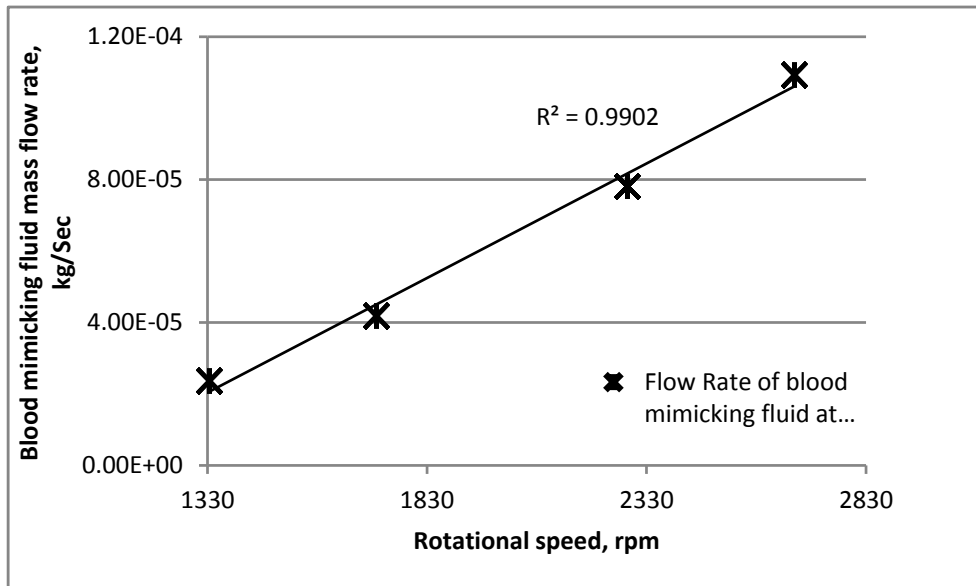


Fig. 5.15: Mass flow rate .vs. rotational speed of the micropump for the blood mimicking fluid operated in the second spiral micropump.

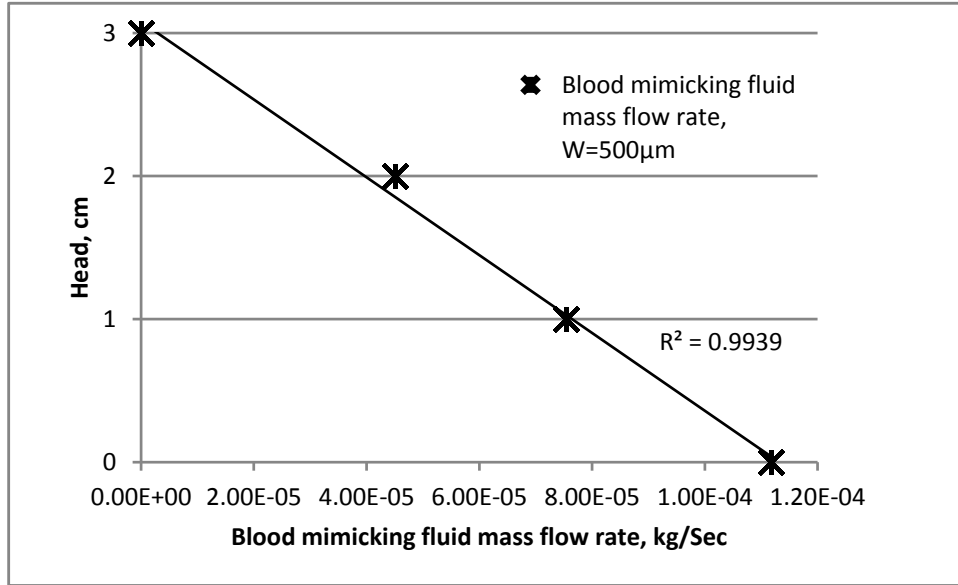


Fig. 5.16: Pump head .vs. mass flow rate of the micropump for the blood mimicking fluid operated in the second spiral micropump.

In figures 5.13 through 5.16 the characteristic curves of the same two spiral micropumps are illustrated, the same behavior is observed with a good linearity and R-squared values. One good observed issue is that the mass flow rate for the blood mimicking fluid is higher than that of the Newtonian working fluid; this is explained by the fact that the power law index of the blood mimicking fluid is lower than unity (shear thinning fluid) with the same operating conditions. This result also insures that the fluid flow in the experimental obtained results is in good agreement with the physical and theoretical expected results.

6.7 Experimental Uncertainty Analysis

In order to find the error encountered in the obtained results, a statistical uncertainty analysis will be performed. This statistical analysis includes finding out the mean, the standard deviation, using the student t-distribution tables and then finding out

the uncertainty as a margin of magnitudes plus or minus the calculated mean. The governing statistical equations of the above mentioned quantities are giving as the following:

The mean, \bar{x} :

$$\bar{x} = \frac{1}{N} \sum_{i=1}^N x_i \quad (5.2)$$

The standard deviation for small quantities ($N < 30$), σ_s :

$$\sigma_s = \left[\frac{1}{N-1} \sum_{i=1}^N (x_i - \bar{x})^2 \right]^{0.5} \quad (5.3)$$

Estimation of precision of error is given by:

$$\bar{x} \mp t_{\alpha/2} \frac{\sigma_s}{\sqrt{N}} \quad (5.4)$$

Where $t_{\alpha/2}$ is a constant taken from the student t-distribution table at a desired confidence interval. In this work the confidence interval is chosen to be 95% ; this means that $\alpha=0.05$, and $\alpha/2=0.025$. For the above α based on 5 degree of freedom; the value of t will be 2.571.

The certainty analysis was performed for the above mentioned figures and found to be about $\pm 0.2 \times 10^{-5}$ for most of the calculated results. Table 5.3 below shows a list of the measured mass flow rates for the two spiral channel micropumps and accompanied with the calculated uncertainty dedicated to each mass flow rate value, while tables 5.4 and 5.5 show the measured mass flow rates with their uncertainties at different outlet heads.

Table 5.3: Measured mass flow rates with their uncertainties .vs. the pump rotational speed:

Rotational Speed, rpm	Spiral Channel 1		Spiral Channel 2	
	Distilled water mass flow rate, kg/Sec	Blood mimicking fluid mass flow rate, kg/Sec	Distilled water mass flow rate, kg/Sec	Blood mimicking fluid mass flow rate, kg/Sec
<u>1333.3</u>	$(2.07 \mp 0.01) \times 10^{-5}$	$(2.25 \mp 0.33) \times 10^{-5}$	$(2.34 \mp 0.36) \times 10^{-5}$	$(2.38 \mp 0.12) \times 10^{-5}$
<u>1714.3</u>	$(4.06 \mp 0.11) \times 10^{-5}$	$(4.22 \mp 0.17) \times 10^{-5}$	$(4.13 \mp 0.12) \times 10^{-5}$	$(4.20 \mp 0.10) \times 10^{-5}$
<u>2285.7</u>	$(6.37 \mp 0.01) \times 10^{-5}$	$(6.40 \mp 0.26) \times 10^{-5}$	$(6.55 \mp 0.53) \times 10^{-5}$	$(7.82 \mp 0.14) \times 10^{-5}$
<u>2666.7</u>	$(10.1 \mp 0.15) \times 10^{-5}$	$(10.5 \mp 0.50) \times 10^{-5}$	$(10.5 \mp 0.78) \times 10^{-5}$	$(10.9 \mp 0.19) \times 10^{-5}$

Table 5.4: Measured mass flow rates with their uncertainties .vs. the outlet head for the distilled water as a working fluid.

Head, cm	Distilled Water	
	Mass flow rate for Spiral channel 1, kg/Sec	Mass flow rate for Spiral channel 2, kg/Sec
<u>2.5</u>	0	0
<u>2.0</u>	$(1.14 \mp 0.09) \times 10^{-5}$	$(1.46 \mp 0.38) \times 10^{-5}$
<u>1.0</u>	$(3.43 \mp 0.28) \times 10^{-5}$	$(3.54 \mp 0.55) \times 10^{-5}$
<u>0.0</u>	$(10.1 \mp 0.15) \times 10^{-5}$	$(10.5 \mp 0.50) \times 10^{-5}$

Table 5.5: Measured mass flow rates with their uncertainties .vs. the outlet head for the blood mimicking fluid.

Head, cm	Blood Mimicking Fluid	
	Mass flow rate for Spiral channel 1, kg/Sec	Mass flow rate for Spiral channel 2, kg/Sec
<u>3.0</u>	0	0
<u>2.0</u>	$(2.13 \mp 0.27) \times 10^{-5}$	$(4.51 \mp 0.46) \times 10^{-5}$
<u>1.0</u>	$(4.13 \mp 0.11) \times 10^{-5}$	$(7.54 \mp 0.30) \times 10^{-5}$
<u>0.0</u>	$(10.5 \mp 0.78) \times 10^{-5}$	$(10.9 \mp 0.19) \times 10^{-5}$

CHAPTER 6

RESULTS AND DISCUSSION

6.1. Introduction

In this chapter, the results obtained by the mathematical modeling and numerical simulations will be discussed. During the discussion; the validation of the current work along with the mesh optimization will be carried out as a first step to insure that the obtained results are accurate and showing the different aspects needed to be studied in a scientifically accepted way. The need to adopting the right model that presents the exact behavior of the selected fluid is illustrated by showing the variation of the flow rate values by changing power law indices i.e. going from Newtonian to different non-Newtonian fluids. Then the effect of the aspect ratio on the flow performance of the single disk, double disk and spiral micropumps will be illustrated. After that the micropumps performance curves for the three adopted types of micropumps will be established. In the last section, shear stress analysis will be performed in order to guarantee that no hemolysis (blood damage) will occur to the blood cells while flowing in the micropumps.

6.2. Validation of the current work, grid optimization and convergence criteria:

In order to verify the present work, both of the mathematical and numerical results were compared to the Newtonian analytical solution [8] as a special case of the present work. In order to convert the present work to Newtonian flow; the power law index (n) is set to be one and the yield stress (τ_0) is set to be zero.

The analytical solution is found by knowing the channel aspect ratio (α) and then finding out the values of both pressure and drag shape factors (F_D and F_P respectively) from the table listed in [8] and also finding out the value of the reduced Reynolds Euler number. After that, the above mentioned three values shall be substituted in the following formula:

$$q^* = \frac{1}{2}F_D - \frac{1}{12}\overline{ReEu}.F_P \quad (6.1)$$

Where q^* is the dimensionless volume flow rate and \overline{ReEu} is the Newtonian reduced Reynolds Euler number which is evaluated by:

$$\overline{ReEu} = \frac{h^2\Delta P}{\mu\bar{U}_{ch}L_o} \quad (6.2)$$

Where h , μ , \bar{U}_{ch} and L_o are the channel height, viscosity, average channel velocity and the pump length respectively. Moreover, the drag and pressure shape factors can be found from the following table:

Table 6.1: Effect of channel aspect ratio on drag and pressure shape factors

Aspect ratio, α	Analytical drag shape factor, F_D		Analytical pressure shape factor, F_P Moving and stationary walls
	Moving walls	Stationary walls	
2.0	1.7297	0.0703	0.1715
1.0	1.5003	0.4997	0.4217
0.5	1.2711	0.7289	0.6860
0.2	1.1107	0.8898	0.8739
0.1	1.0575	0.9425	0.9371

The results showed an excellent agreement with the analytical solution mentioned above. Table 6.2 below shows the obtained results at an aspect ratio of one and zero outlet pressure.

Table 6.2: A Comparison of both mathematical and numerical Newtonian results to the analytical solution [8] at $\alpha=1$, $m=3.5 \times 10^{-3}$ [Pa.Sec], $P_o=0.0$ [Pa], $n=1$ and $\tau_o=0.0$ [Pa].

	Analytical Solution	FDM Solution	% deviation of FDM from analytical solution	FVM Solution	% deviation of FDM from analytical solution
Spiral Micropump	7.52e8	7.43e-8	1.12%	7.56e-8	0.57%
Double Disk Micropump	4.96e-8	4.85e-8	2.11%	4.99e-8	0.62%
Single Disk Micropump	2.48e-8	2.4e-8	3.25%	2.89e-8	16.74%

From the table above, it can be easily figured out that the best results accuracy is for the spiral channel micropump, then the double disk becomes with less accuracy. The accuracy of the results obtained for the single disk micropumps are the lower between the three types of micropumps. Nevertheless, the accuracy of the results of the three obtained micropumps is still remains within the acceptable range. The reason behind this variation of obtained accuracy can be explained by the nature of the boundary conditions adopted for each type of micropumps, as we have three moving walls for the spiral channel micropump, two moving walls for the double disk micropump and one moving wall for the single disk micropump.

Several aspect ratios were studied under the Newtonian fluid consideration in order to verify both of the adopted solution methods (i.e. the FDM and the FVM) but only two aspect ratios were randomly selected to be viewed in this work in order to avoid the enormous number of drawings that show the same verifying principle. The adopted two aspect ratios for the three types of micropumps are one and one-fifth.

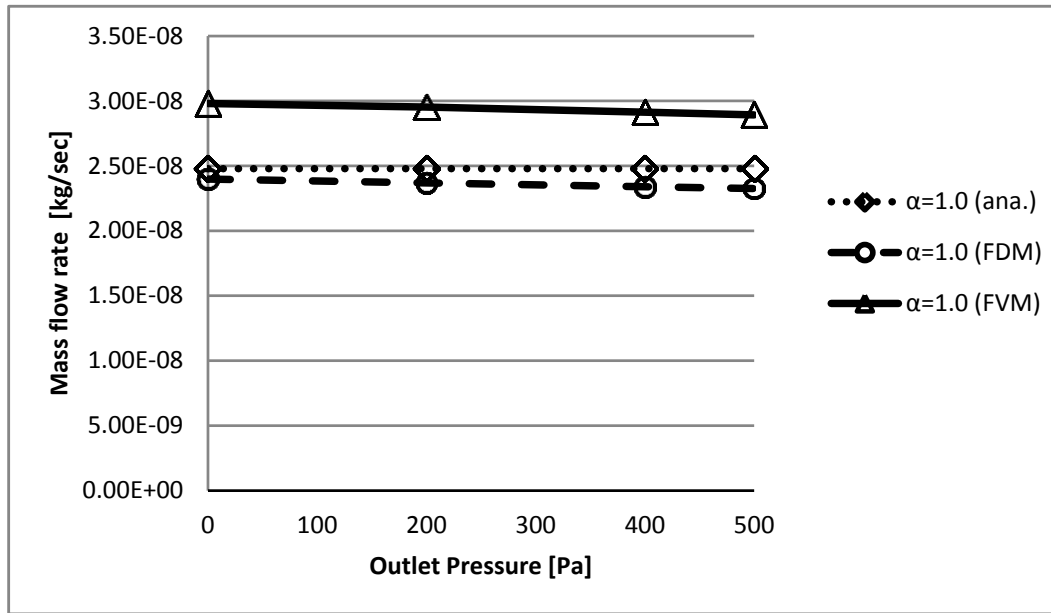


Fig 6.1: Mass flow rate .vs. outlet pressure for single disk micropump with Newtonian blood properties. $\alpha=1.0$, $m=3.5 \times 10^{-3}$ Pa.Sec, $n=1$ and $\tau_o=0.0$ [Pa].

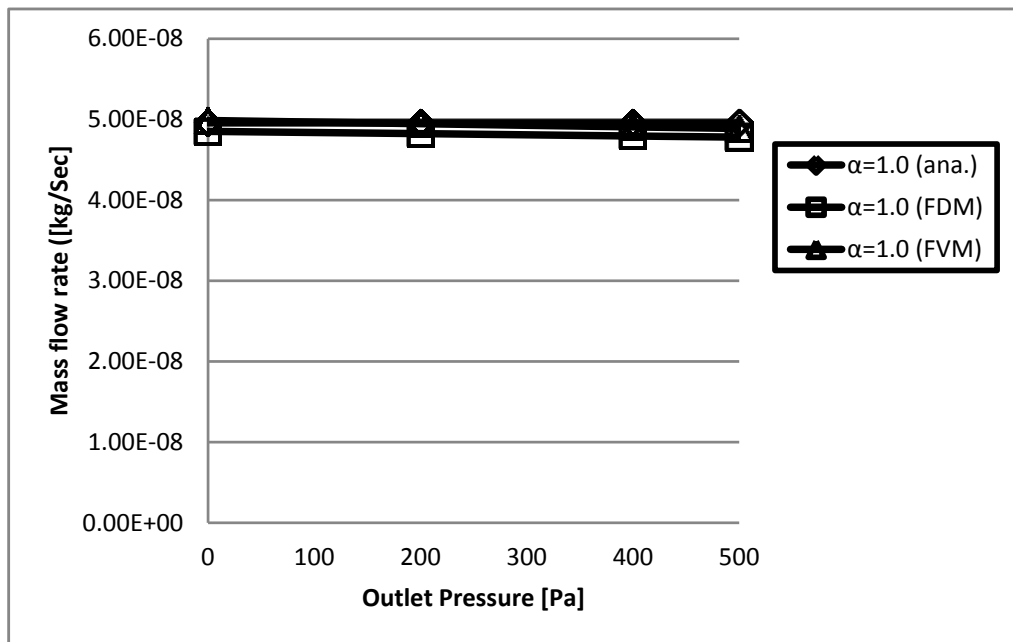


Fig 6.2: Mass flow rates .vs. outlet pressure for double disk micropump with Newtonian blood properties. $\alpha=1.0$, $m=3.5 \times 10^{-3}$ Pa.Sec, $n=1$ and $\tau_o=0.0$ [Pa].

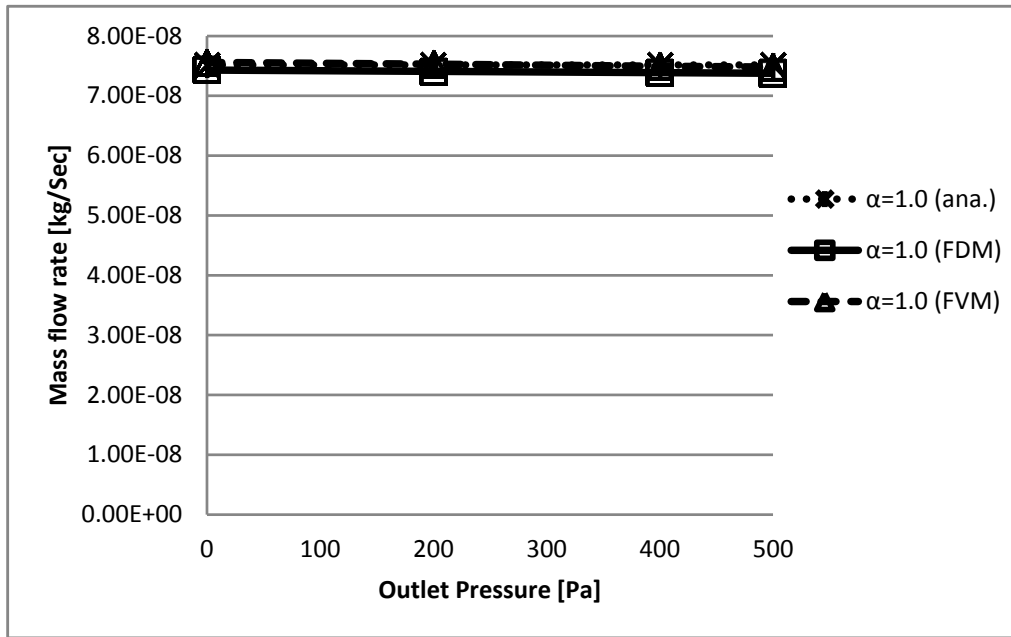


Fig 6.3: Mass flow rate .vs. outlet pressure for spiral micropump with Newtonian blood properties. $\alpha=1.0$, $m=3.5 \times 10^{-3}$ Pa.Sec, $n=1$ and $\tau_o=0.0$ [Pa].

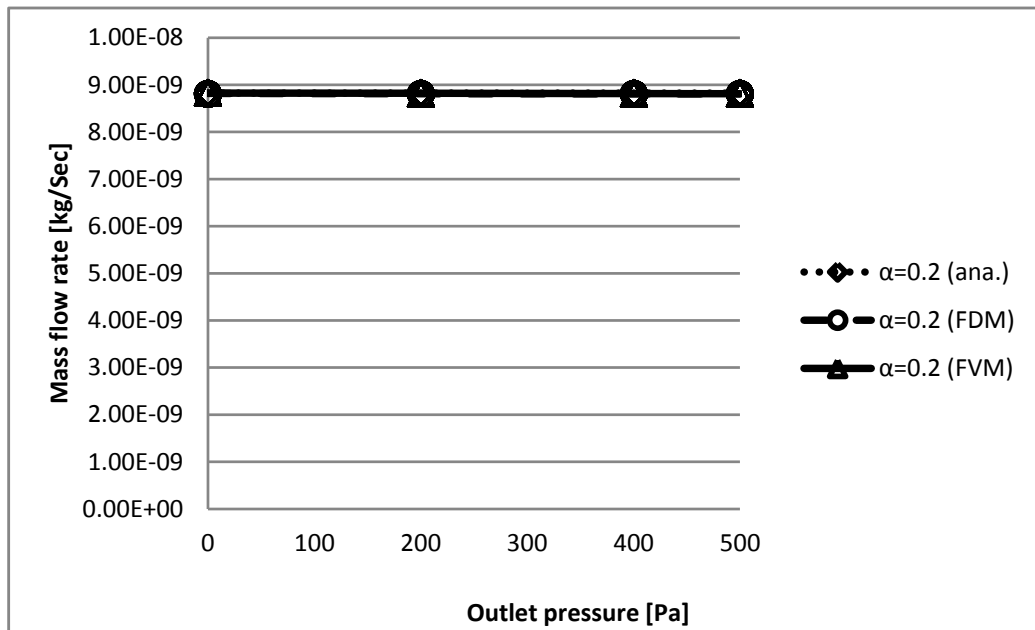


Fig 6.4: Mass flow rate .vs. outlet pressure for single disk micropump with Newtonian blood properties. $\alpha=0.2$, $m=3.5 \times 10^{-3}$ Pa.Sec, $n=1$ and $\tau_o=0.0$ [Pa].

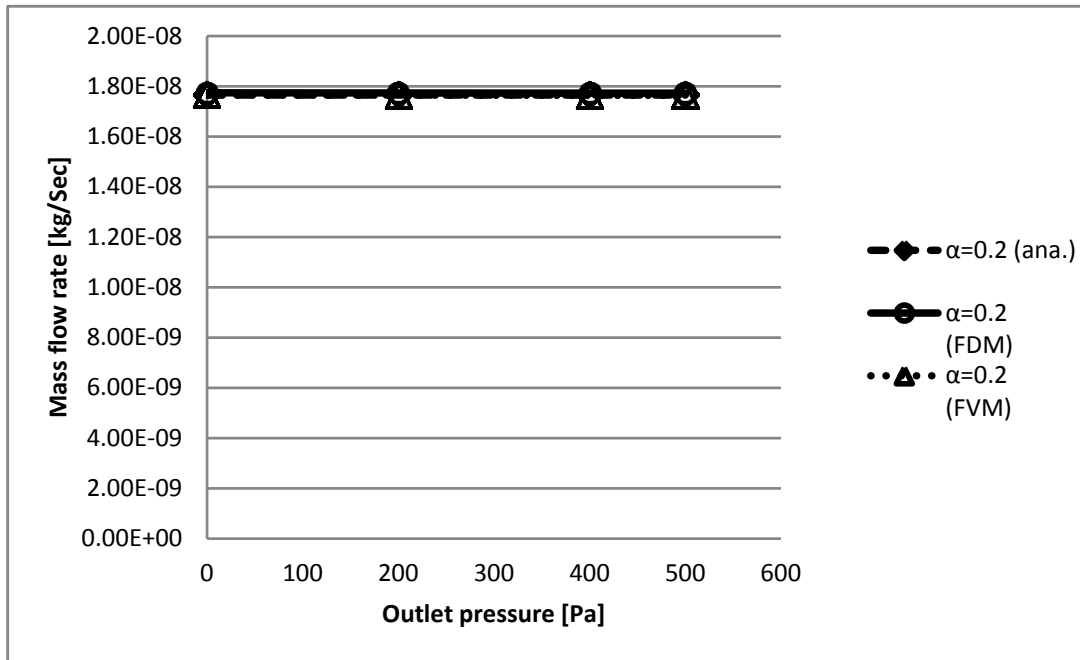


Fig 6.5: Mass flow rate .vs. outlet pressure for double disk micropump with Newtonian blood properties. $\alpha=0.2$, $m=3.5 \times 10^{-3}$ Pa.Sec, $n=1$ and $\tau_0=0.0$ [Pa].

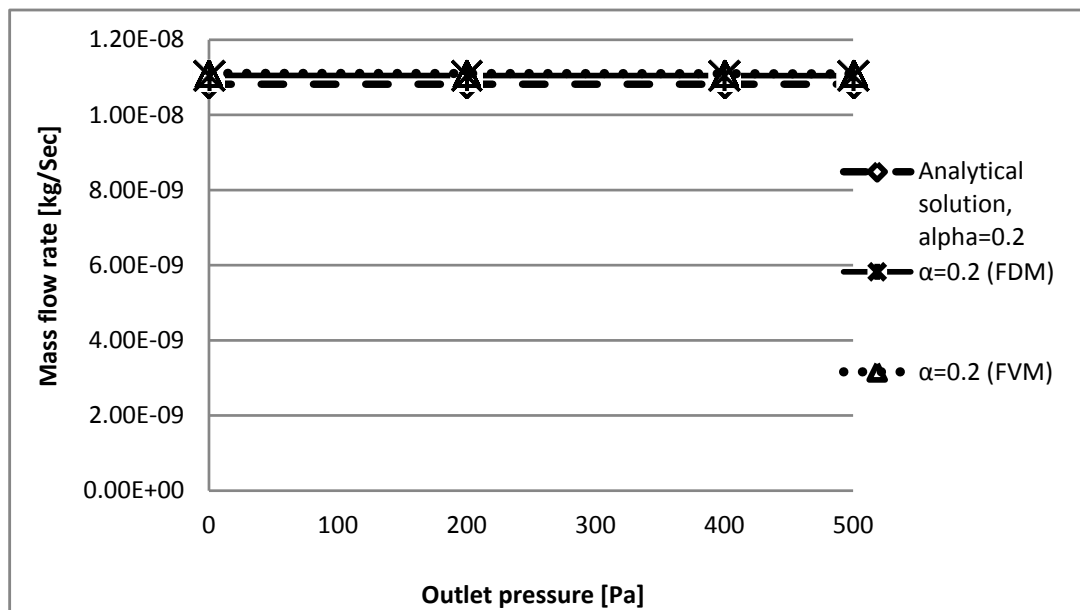


Fig 6.6: Mass flow rate .vs. outlet pressure for spiral micropump with Newtonian blood properties. $\alpha=0.2$, $m=3.5 \times 10^{-3}$ Pa.Sec, $n=1$ and $\tau_0=0.0$ [Pa].

As indicated in figures 6.1 through 6.6, an excellent agreement between the analytical solution[8] and the present work is achieved.

A number of mesh sizes in FLUENT software and step sizes in Matlab code were tested in order to obtain the mesh independent solution through the test procedure described in section 4.8. This test is done to obtain the optimum step and/or mesh size that will enable obtaining a very accurate solution with minimum number of calculations.

In the Matlab code where the study was dealing with obtaining the solution in dimensionless parameters; several step sizes were tested and reduced until grid independent solution and convergence are achieved in order to obtain the optimum step sizes for the different aspect ratios. The results were as in the table 6.3:

Table 6.3: Optimum step size for each aspect ratio used with the Matlab code obtaining the non-dimensional solution of the current problem.

Aspect ratio, α	Optimum step size
$\alpha \geq 5.0$	0.1
$\alpha = 5.0$	$0.5/\alpha$
$\alpha = 2.0$	$1.0/\alpha$
$\alpha \leq 1.0$	0.1α

Figure 6.7 shows the way the optimum size of the step size for the FDM solution obtained by the Matlab program. In this figure the solution was started from a harsh (Coarse) dimensionless step size which is 0.5 and then the step size was refined to a finer (smaller) step sizes (i.e. 0.2, 0.1 and 0.05). It is noted that the solution curves with the smallest step size were almost of the same values and a small difference in their values was noticed (the difference was in less than an order of 10^{-5}). As a result of that,

the one-tenth step size is considered the optimum step size in order to avoid time waste and unnecessary amount of calculations before attaining the required solution.

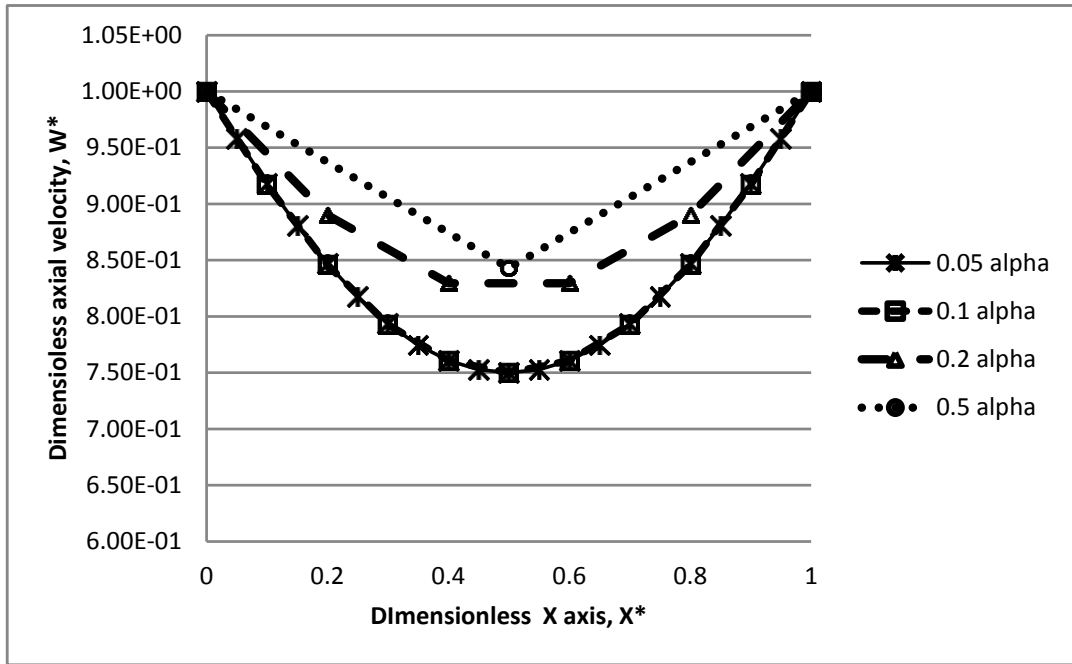


Fig. 6.7: Procedure for finding the optimum step size for the Matlab code. $\alpha=1$, $m=3.5 \times 10^{-5}$, $\tau_0=0.0$, $P_{in}=P_{out}=0.0$ and $n=1$.

In figure 6.7, it can be easily noticed that the solution with a step size equals (0.1α) equals the solution with the step size (0.05α) . Therefore the, optimum step size is taken to be one tenth the aspect ratio for $n \leq 1.0$.

The same is done with the FVM solution obtained by FLUENT; the mesh size was changed from coarser to finer sizes until the solution becomes independent of the mesh size. Furthermore, after reaching the optimum grid size, another check is done using the gradient adaption facility in the FLUENT program at which the mesh is refined by setting a small value of the refine threshold then the FLUENT run is restated. If the difference in the two solutions was within the accepted error then the attained

optimum step size is accepted. Figure 6.8 below shows the attained optimum grid size for the double disk micropump with a unity aspect ratio.

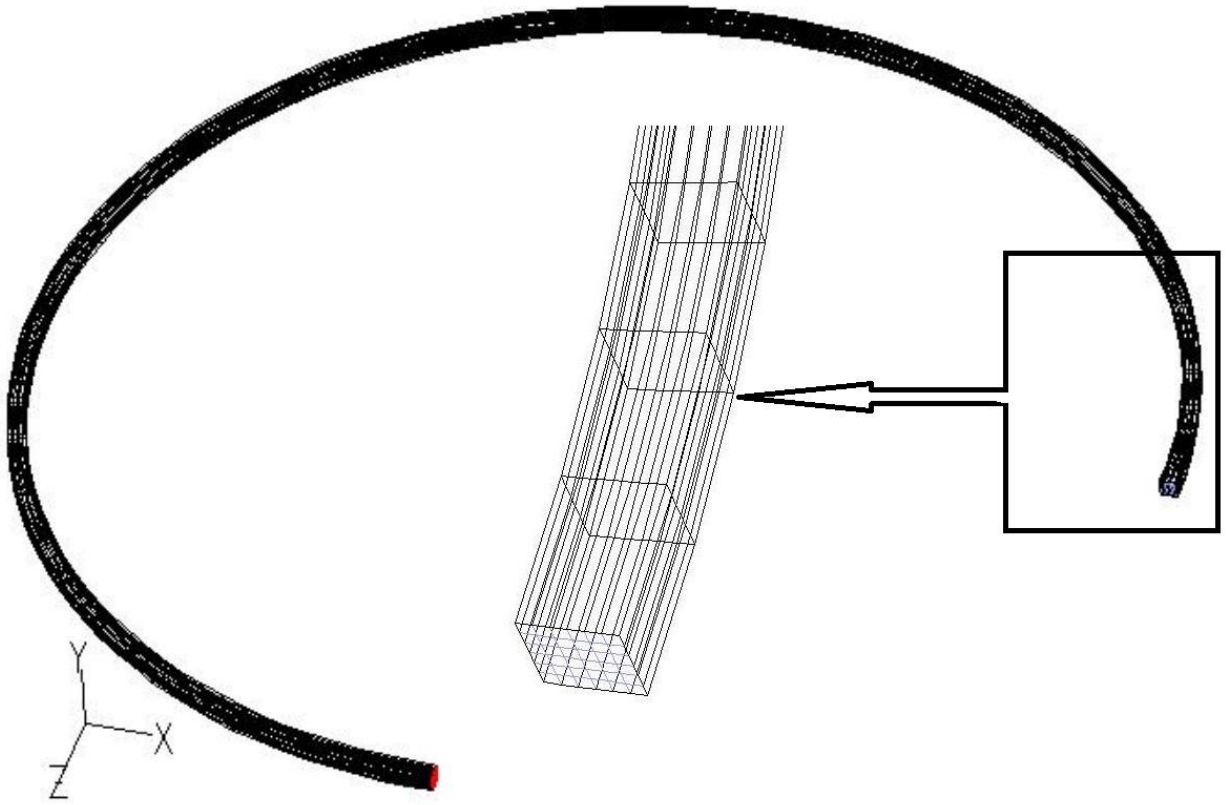


Fig. 6.8: Meshed double disk micropump. $L=30 \times 10^{-6} \text{m}$, $\alpha=1$, $R_{ave}=1010 \times 10^{-6} \text{m}$ and $\theta=270^\circ$.

For the convergence criteria, the convergence criteria are achieved by one of the following:

- I. The minimum residuals is less than or equal to 1×10^{-6} at which the solution became steady in the FLUENT.
- II. Obtaining a steady solution with low residuals in FLUENT, this is done by monitoring the residuals.

- III. Minimum velocity residuals in the Matlab code is less than or equal 1×10^{-6} or the number of iterations exceeded 10,000 iterations. Usually the solution is obtained at about 750 iterations.
- IV. Monitoring the difference between the inlet and outlet flow rates, this is done by reporting both inlet flow and outlet flow and having almost the same values for each when using the FLUENT program.

Figure 6.9 below shows the residuals obtained in one of the FLUENT runs.

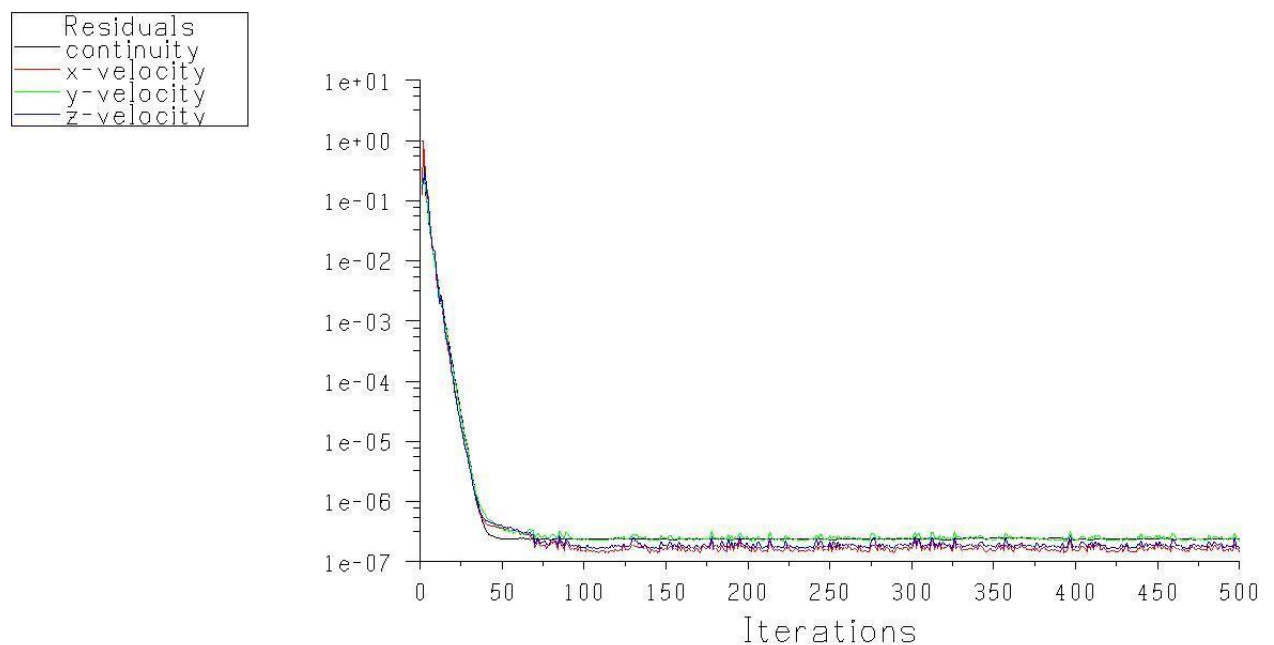


Fig. 6.9: Convergence criteria in FLUENT.

6.3 Effect of power index, n , on the fluid flow inside the micropumps

As discussed in chapter two, as the power index changes from values that are greater than one (i.e. shear thickening or dilatant) at which the fluid viscosity decreases with the increase of the shear rate to values of power index less than one (i.e. shear thinning) at which the fluid viscosity increases with the increase of the shear rate, the

velocity and the amount of flow rate changes with the same input conditions. This issue is carried out in this study and the results showed that as the value of power law index decreases, the mean velocity and the flow rate increase for the same duct cross section and input conditions. Figures 6.10 through 6.12 below show the effect of the power law index for the single disk , double disk and spiral channel micro pumps respectively.

In figure 6.10 which is for the single disk micro pump, the dimensionless axial velocity is shown at the mid-distance of the channel height, at which it is noticed that the magnitude of the dimensionless velocity was changed, for example, from 0.480 to 0.641 while going from Newtonian fluid with a unity power law index (i.e. $n=1$) to a shear thinning fluid with a power law index of 0.7. This means that the velocity at the center of the channel cross-section was increased by 30% as the fluid in the second case will be with a very low viscosity. Moreover, the magnitude of the velocity at the center of the channel cross-section was changed from 0.480 to 0.466 while going from a unity power law index to power law index of a value of two, this decrease in the dimensionless axial velocity is almost 3% less than the magnitude of the Newtonian fluid mid planer velocity.

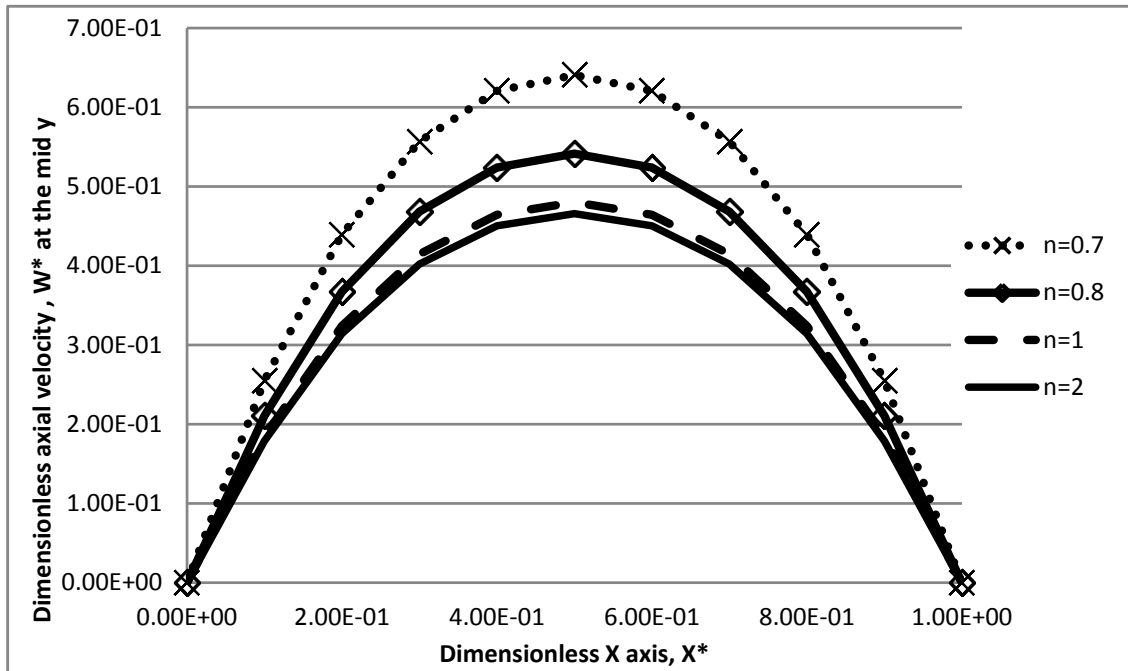


Fig. 6.10: The effect of power law index on the performance of single disk micropump. $\alpha=1$, $P_{in}=1000$ Pa, $P_{out}=0.0$, $\theta=270^\circ$, $\tau_0=3.15 \times 10^{-3}$ Pa, $m=7.95 \times 10^{-3}$ Pa.Secⁿ.

In figure 6.11 below which is for the double disk micro pump, the dimensionless axial velocity is also shown at the center of the channel height, the magnitude of the dimensionless velocity is noticed to be changed, for example, from 0.600 to 0.749 while going from Newtonian fluid with a unity power law index (i.e. $n=1$) to a shear thinning fluid with a power law index of 0.7. This means that the mid-plan velocity was increased by almost one-fourth.

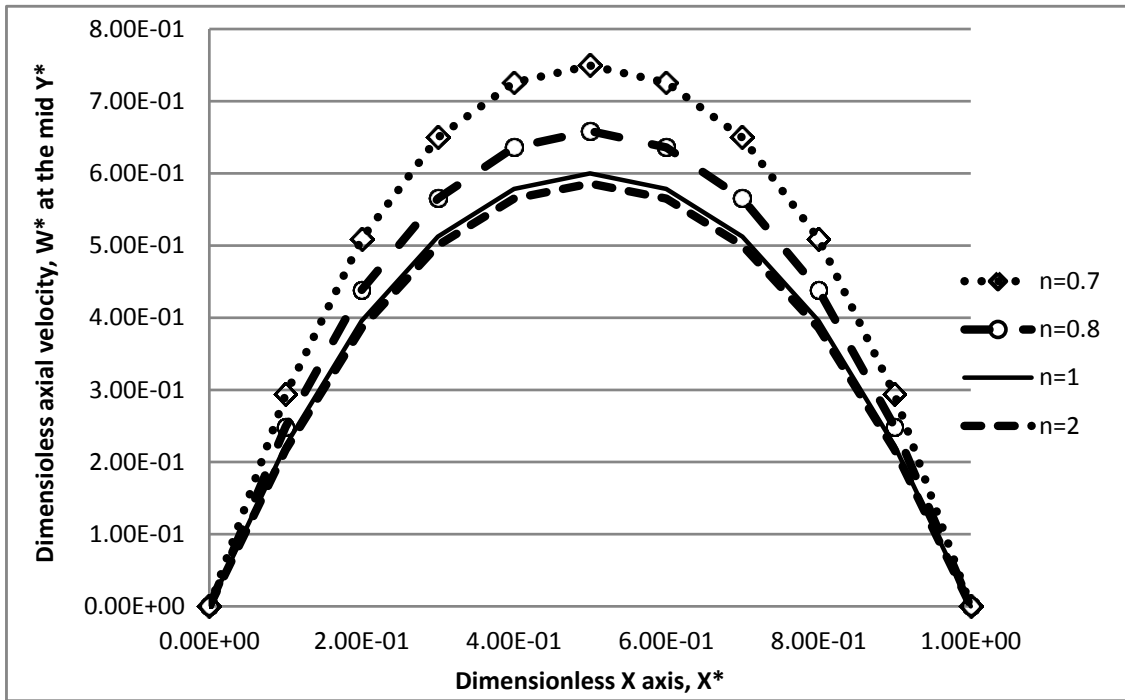


Fig. 6.11: The effect of power law index on the performance of double disk micropump. $\alpha=1$, $P_{in}=1000$ Pa, $P_{out}=0.0$, $\theta=270^\circ$, $\tau_0=3.15 \times 10^{-3}$ Pa, $m=7.95 \times 10^{-3}$ Pa \cdot Sec n .

Figure 6.12 shows the effect of power law index on the velocity along the channel's mid height, the magnitude of the dimensionless velocity is noticed to be changed, for example, from 0.545 to 0.658 while going from Newtonian fluid with a unity power law index (i.e. $n=1$) to a shear thinning fluid with a power law index of 0.7. This means that the mid-plan velocity was increased by almost 25% with the low power index value.

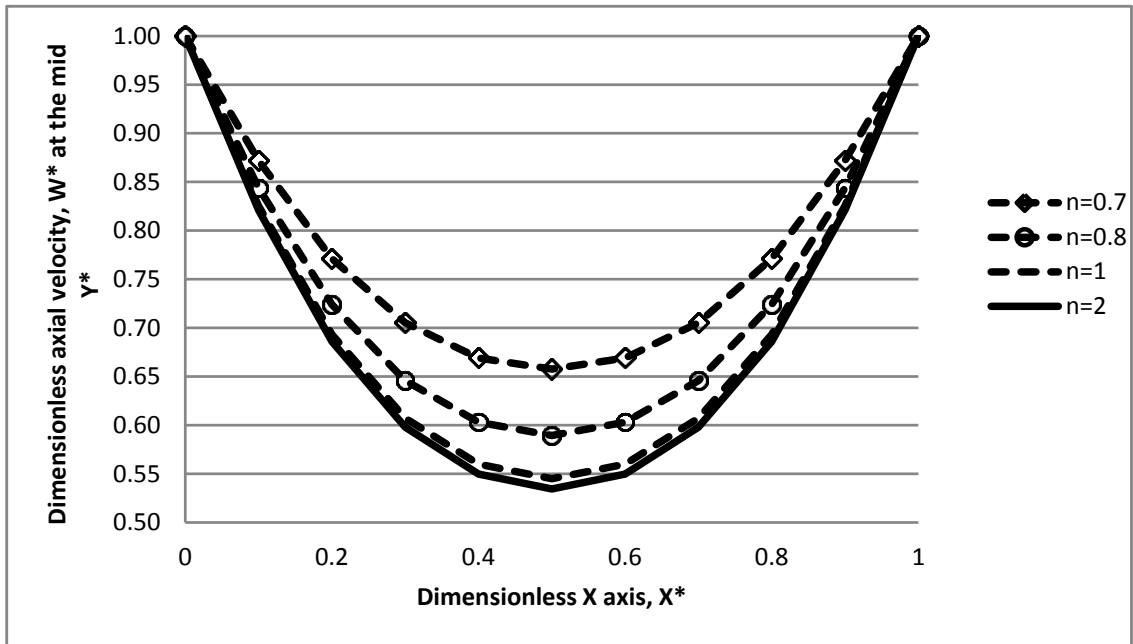


Fig. 6.12: The effect of power law index on the performance of spiral micropump. $\alpha=1$, $P_{in}=1000$ Pa, $P_{out}=0.0$, $\theta=270^\circ$, $\tau_o=3.15 \times 10^{-3}$ Pa, $m=7.95 \times 10^{-3}$ Pa.Secⁿ.

In order to have a clearer image of what the change in the power law index from Newtonian to non-Newtonian fluid flow can do, the average velocity at the mid-distance of the height is considered in table 6.4:

Table 6.4: The average dimensionless axial velocity for the three types of the micropumps at different power law index values.

Power law index, n	Single disk micropump average dimensionless axial velocity	% deviation from the Newtonian average dimensionless axial velocity	Double disk micropump average dimensionless axial velocity	% deviation from the Newtonian average dimensionless axial velocity	Spiral Channel micropump average dimensionless axial velocity	% deviation from the Newtonian average dimensionless axial velocity
n=0.7	0.3191	28.51%	0.5610	14.51%	0.7470	0.65%
n=0.8	0.2747	10.63%	0.5172	5.57%	0.7441	0.26%
n=1.0	0.2483	0.00%	0.4899	0.00%	0.7422	0.00%
n=2.0	0.2418	2.62%	0.4836	1.29%	0.7417	0.07%

The above table clarifies that if a single micropump is required to deliver a certain non-Newtonian fluid with a power law index of 0.7, for example, then the amount of the delivered non-Newtonian fluid will be 28.51% higher than that if the fluid is assumed to be Newtonian with the same operating conditions and pump input power. The same is applied for the other types of micropump if the fluids working in these micropumps were treated as Newtonian or non-Newtonian. This issue is so important especially if these pumps are used in such applications at which a high precision of fluid rate is required such as dosing a highly concentrated drug in human body for example.

6.4. Effect of Aspect Ratio on the Flow Performance of the Single Disk, Double disk and Spiral Channel Micropumps

In this section and the sections follow, the blood properties were introduced to both Matlab code and the FLUENT software, the adopted Non-Newtonian model is Herschel Bulkley model with the following model constants:

Table 6.5: Herschel Bulkley blood constants:

Property	Blood property value
Power law index, n	0.82
Yield shear stress, τ_0	$3.15 \times 10^{-3} \text{Pa}$
Consistency constant, m	$7.95 \times 10^{-3} \text{Pa} \cdot \text{Sec}^n$

Then the effect of changing the aspect ratio on the performance of the single disk, double disk and the spiral micropumps is studied by showing this effect on both the dimensionless speed at both mid-distance of the dimensionless channel height and

the three quarters of the dimensionless channel height. The results are shown in the following figures:

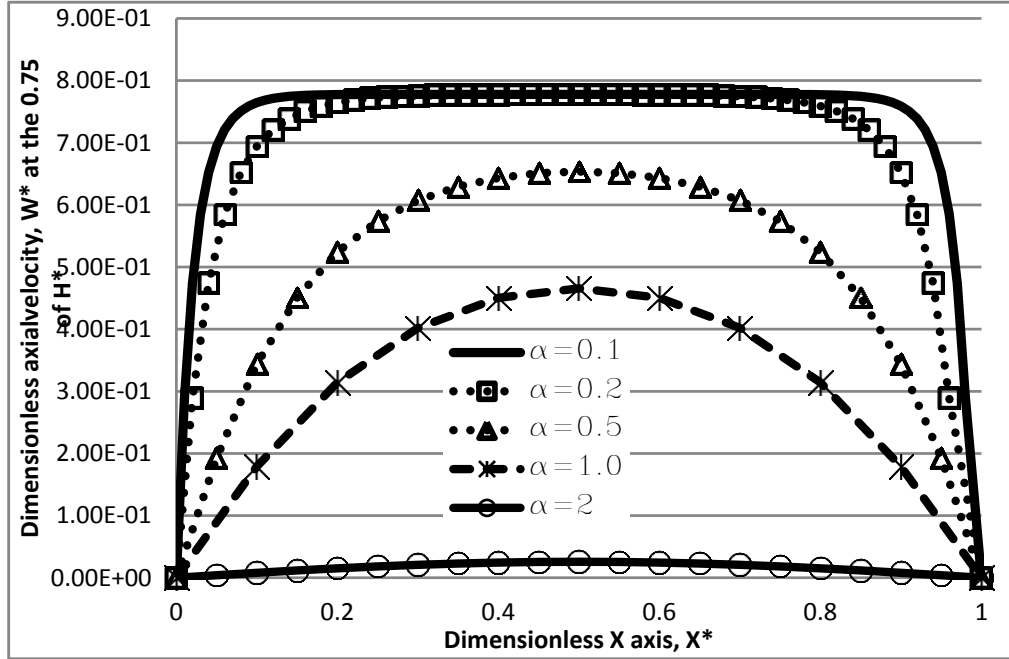


Fig. 6.13: The effect of changing the aspect ratio on the dimensionless axial velocity in a single disk micropump, W^* at the three-fourth of the dimensionless channel height. $\theta=270^\circ$, $P_{in}=P_{out}=0.0$ Pa, $\omega=1000$ rpm.

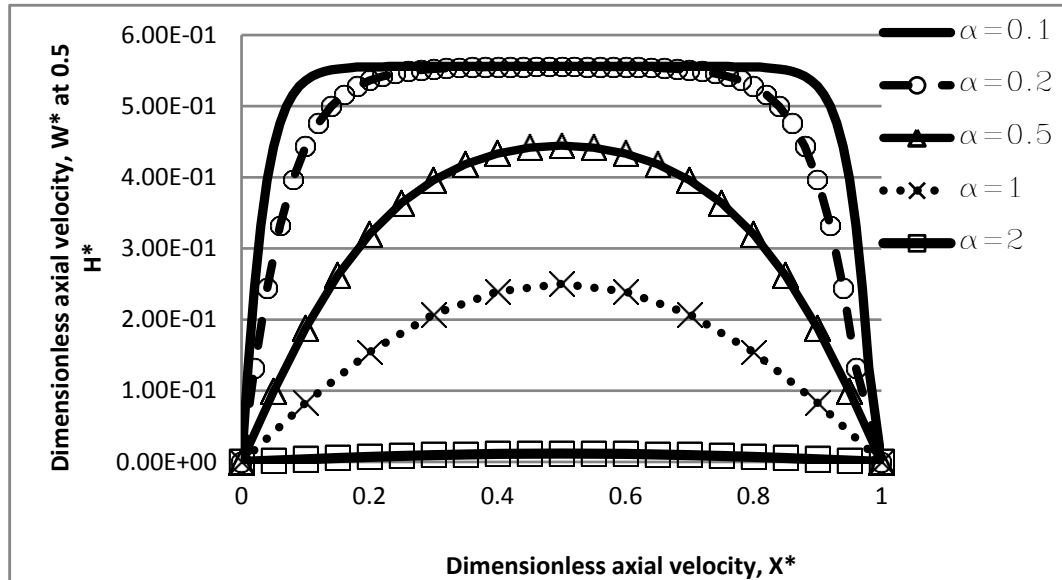


Fig. 6.14: The effect of changing the aspect ratio on the dimensionless axial velocity in a single disk micropump, W^* at the one half of the dimensionless channel height. $\theta=270^\circ$, $P_{in}=P_{out}=0.0$ Pa, $\omega=1000$ rpm.

In figures 6.13 and 6.14 above, it can be seen easily that the dimensionless axial velocities at the three-fourth distance of the dimensionless height in the single disk micropump is larger than their corresponding velocities at the mid-distance of the dimensionless height, the reason behind this is simply the fact that the dimensionless velocities in the first case are closer to the moving wall than those in the mid distance. For the double disk and spiral channel micropumps in figures 6.15-18.

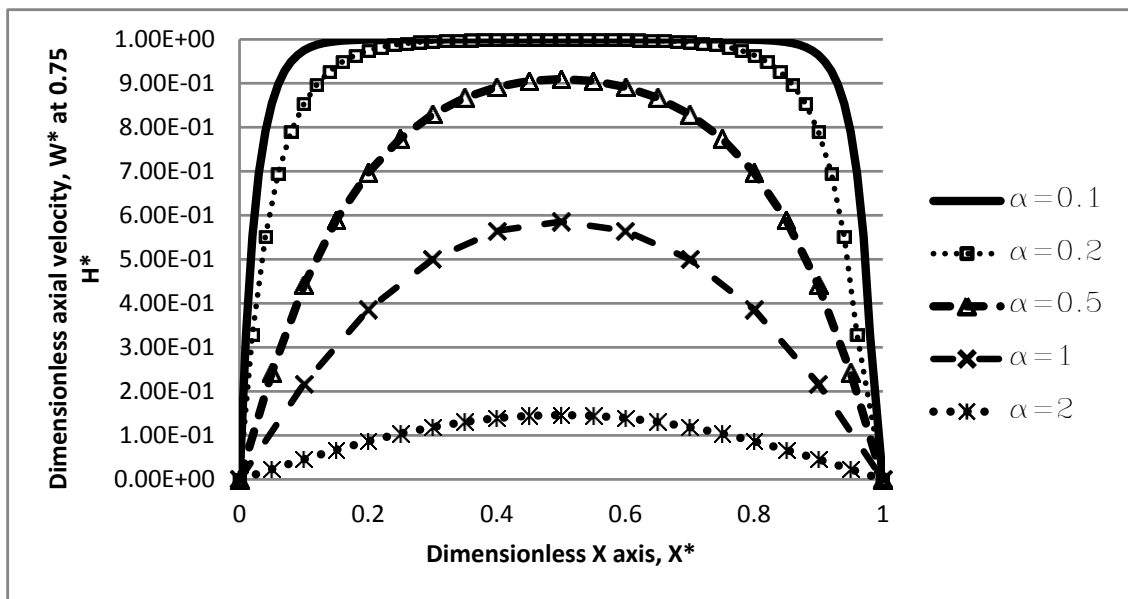


Fig. 6.15: The effect of changing the aspect ratio on the dimensionless axial velocity in a double disk micropump, W^* at the three fourth of the dimensionless channel height. $\theta=270^\circ$, $P_{in}=P_{out}=0.0$ Pa, $\omega=1000$ rpm.

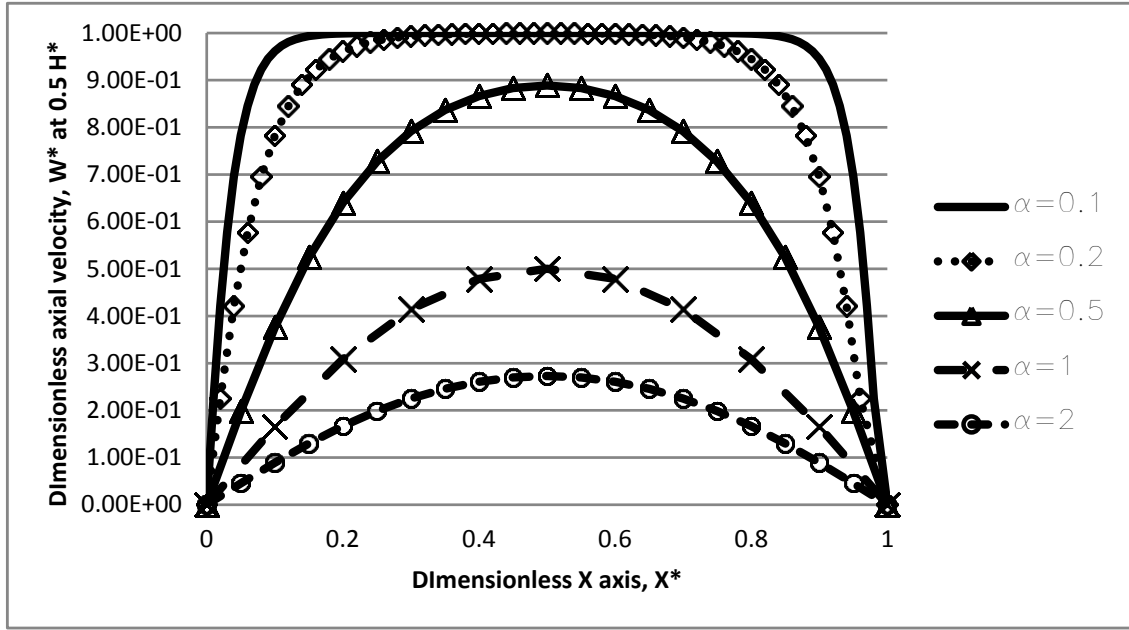


Fig. 6.16: The effect of changing the aspect ratio on the dimensionless axial velocity in a double disk micropump, W^* at the one half of the dimensionless channel height. $\theta=270^\circ$, $P_{in}=P_{out}=0.0$ Pa, $\omega=1000$ rpm.

When comparing the dimensionless axial velocities of the single disk micropumps with those velocities of these double disk micropumps it can be found that the magnitude of the dimensionless velocities of the double disk micropumps is almost double of those of the single disk micropumps. The reason behind this issue is that, in the double disk micropumps it is assumed that there are two moving walls; one is at the surface of the micro pump and the other is at the top surface of the micropump. This issue is not valid in single disk micropumps with aspect ratios greater than two as it is noticed that the fluid flow far of the moving top wall is almost not affected by the movement of the top wall. This can be explained by the fact that the flow at a far distance from the moving wall is located outside the boundary layer thickness and so is not affected by the moving wall, this issue is much less observed in the double disk

micropumps as there is a double effect of the moving two walls and then the fluid particles is always located within the hydraulic boundary layers.

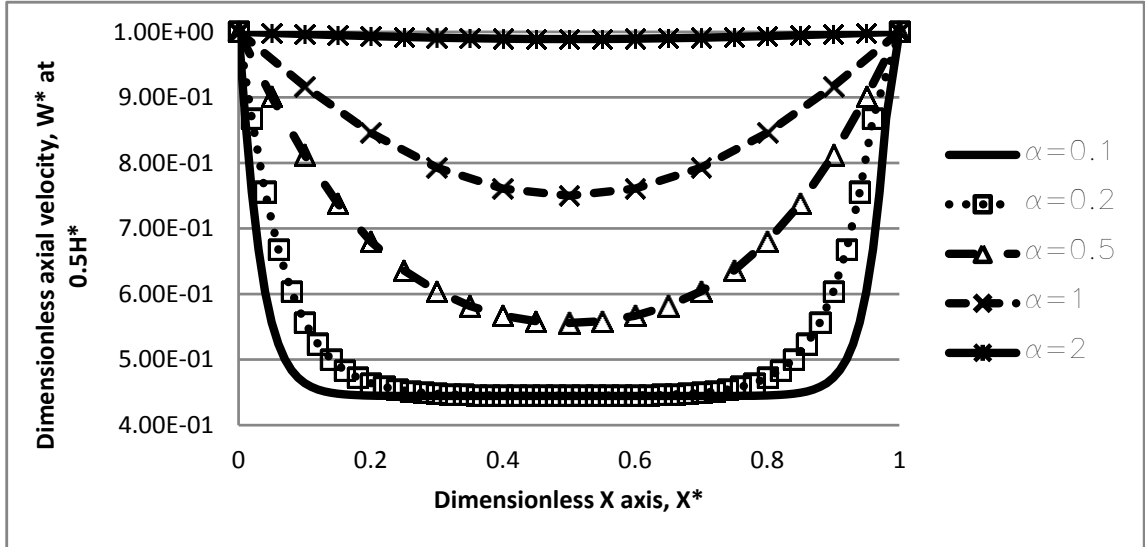


Fig. 6.17: The effect of changing the aspect ratio on the dimensionless axial velocity in spiral micropump, W^* at the one half of the dimensionless channel height. $\theta=270^\circ$, $P_{in}=P_{out}=0.0$ Pa, $\omega=1000$ rpm.

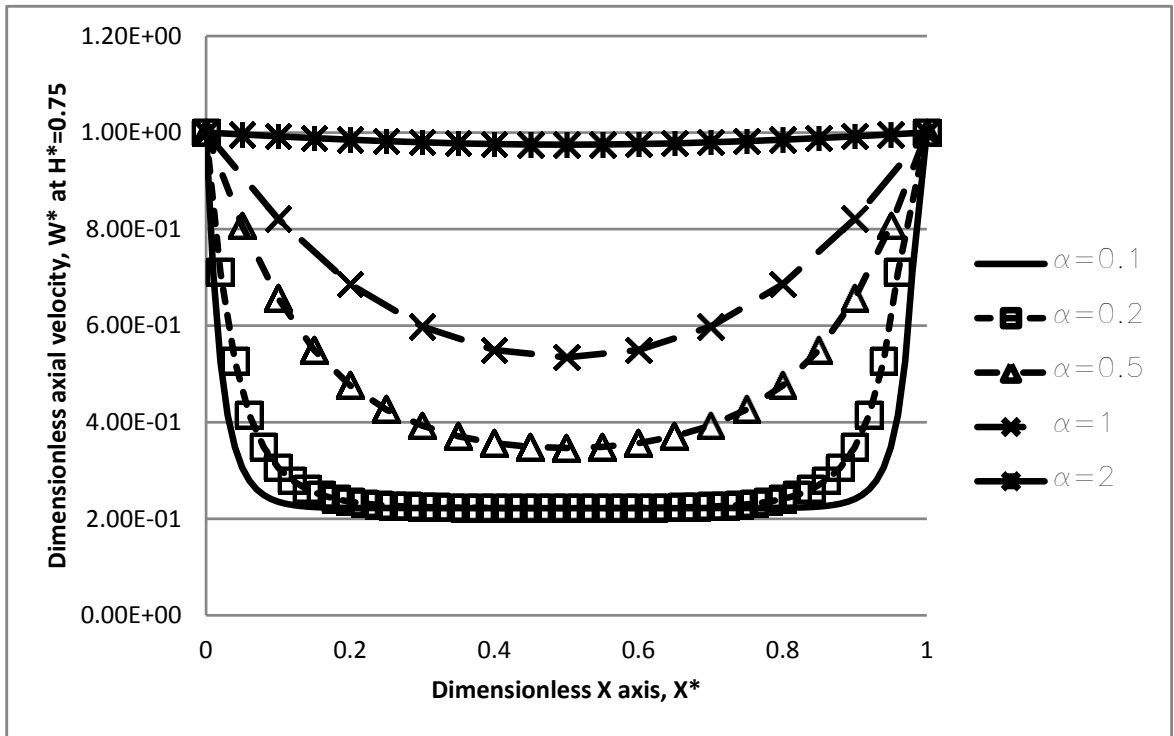


Fig. 6.18: The effect of changing the aspect ratio on the dimensionless axial velocity in spiral micropump, W^* at the one three-fourth of the dimensionless channel height. $\theta=270^\circ$, $P_{in}=P_{out}=0.0$ Pa, $\omega=1000$ rpm.

In figures 6.17 and 6.18 the velocity profile behavior of the spiral channel micropumps is shown. Due to the assumptions of the three moving walls in the spiral channel micropump the velocities of the spiral channel micropumps are larger than the corresponding velocities in the single and double disk micropumps.

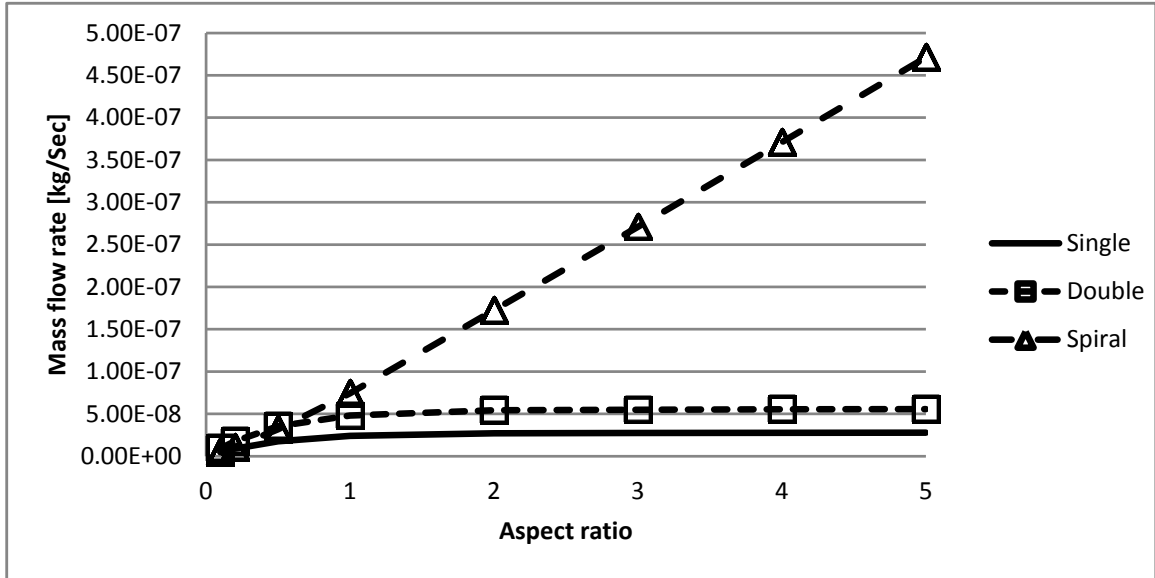


Fig. 6.19: The mass flow rate [kg/Sec] at different aspect ratios for the three types of micro pumps. $L=30 \times 10^{-6} \text{m}$, $P_{in}=P_{out}=0$.

In figure 6.19 the mass flow rate is shown at different aspect ratios to show the performance of the three adopted types of micro pumps, the results show that the optimum aspect ratio of both the single and double disk micro pumps is about two, and for values greater than two, the flow rate increase becomes almost unchanged. While this is not the case for the spiral micropumps as the mass flow rate keeps increasing even for aspect ratios more than five; this phenomenon can be explained by the following: at aspect ratios bigger than two, the fluid near the cross sectional center -in both single disk and double disk micropumps- becomes far from the walls and the effect of the moving walls doesn't affect the above mentioned region of fluid this is very close to the boundary layer theory at which the flow outside the boundary layer is not affected by the forces exerted by the moving walls for example. As a result of having three moving in the spiral channel micropump, the third wall almost cancels the existence of

such areas at which the fluid is far from the moving walls effect. Figures 6.20-22 shows in details the phenomenon mentioned above:

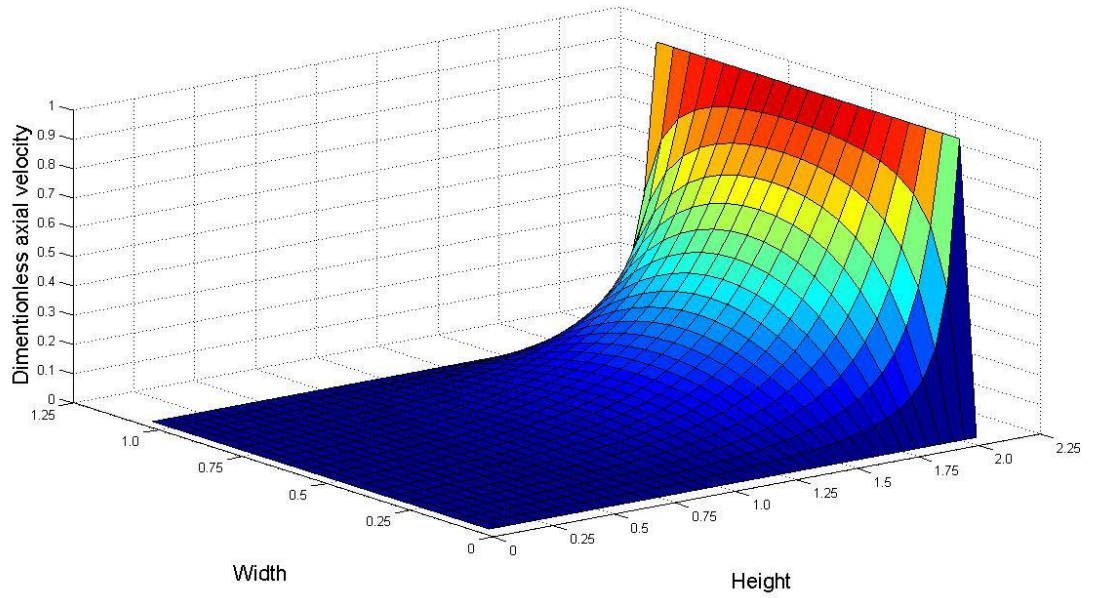


Fig 6.20: Dimensionless axial velocity at $\alpha=2$ for single disk micropump, $\Delta P=0$ Pa.

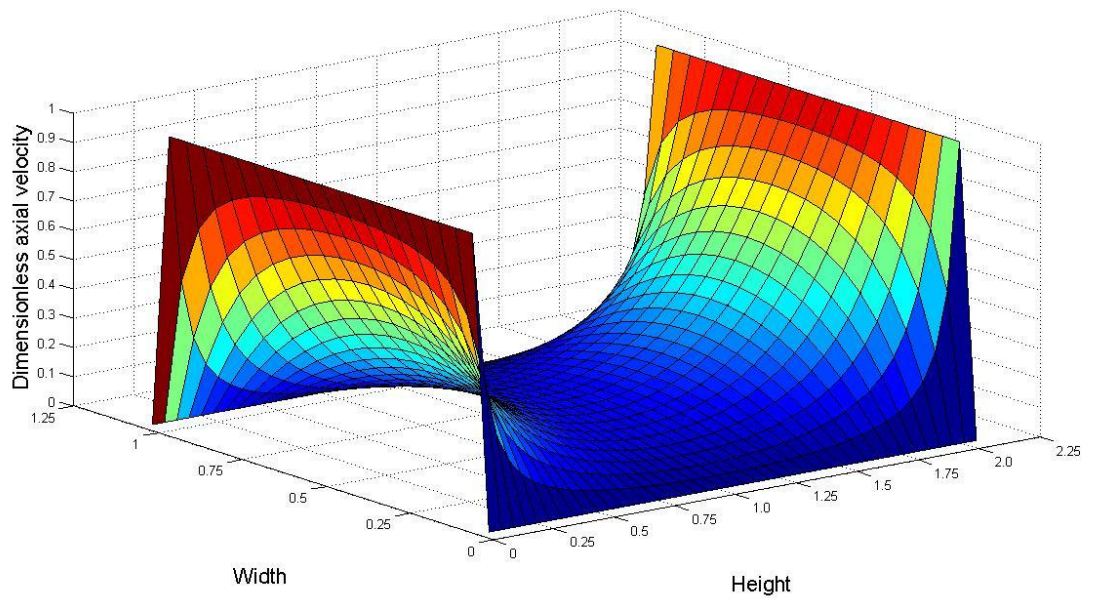


Fig 6.21: Dimensionless axial velocity at $\alpha=2$ for double disk micropump, $\Delta P=0$ Pa.

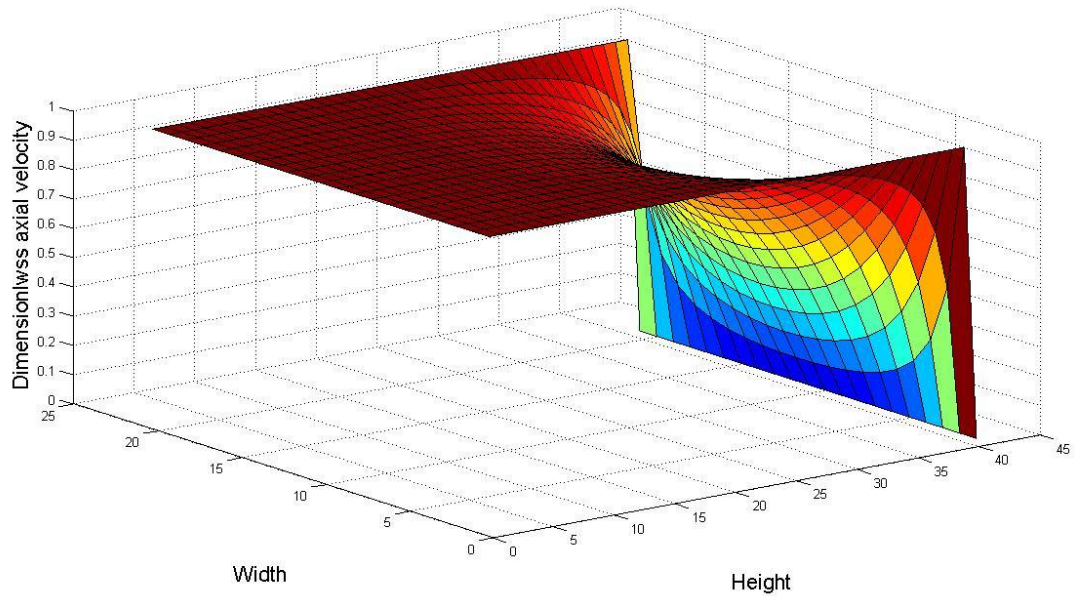


Fig 6.22: Dimensionless axial velocity at $\alpha=2$ for Spiral channel micropump, $\Delta P=0$ Pa.

The dimensionless axial velocities, W^* in the lateral dimensionless X and Y axes for the single disk, double disk and spiral micropumps at a unity aspect ratio are shown in the flowing figures that are resulted by the FDM solution:

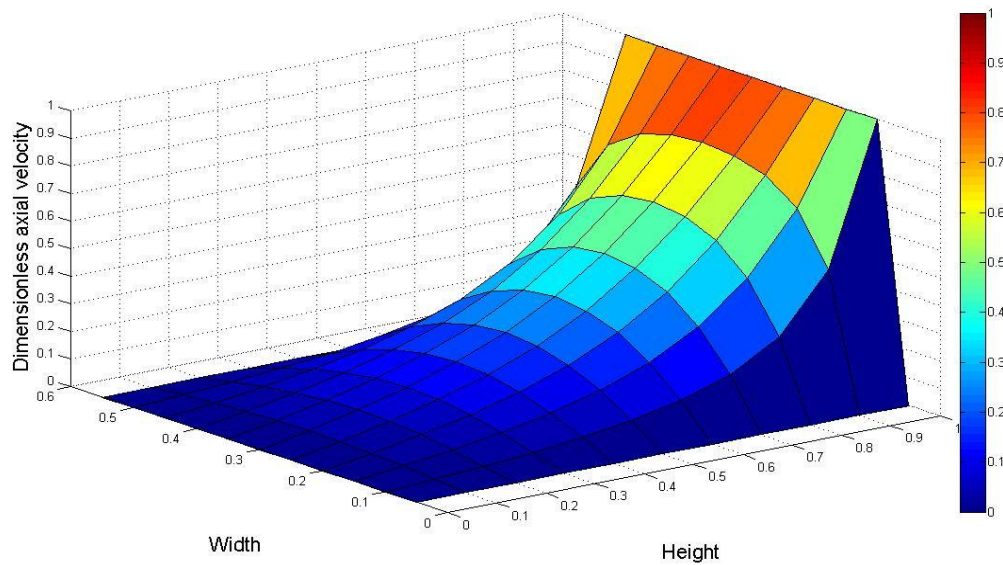


Fig. 6.23: The dimensionless axial velocity in the dimensionless X and Y axes for a single disk micropump. $\alpha=1.0$, $P_{in}=P_{out}=0.0$ Pa, $\omega=1000$ rpm, $\theta=270=270^\circ$.

Figure 6.23 above shows the flow behavior of the fluid through the single disk microchannel. In this walls are kept at zero dimensionless velocity (fixed) while the fourth wall is moving at a unity dimensionless axial velocity.

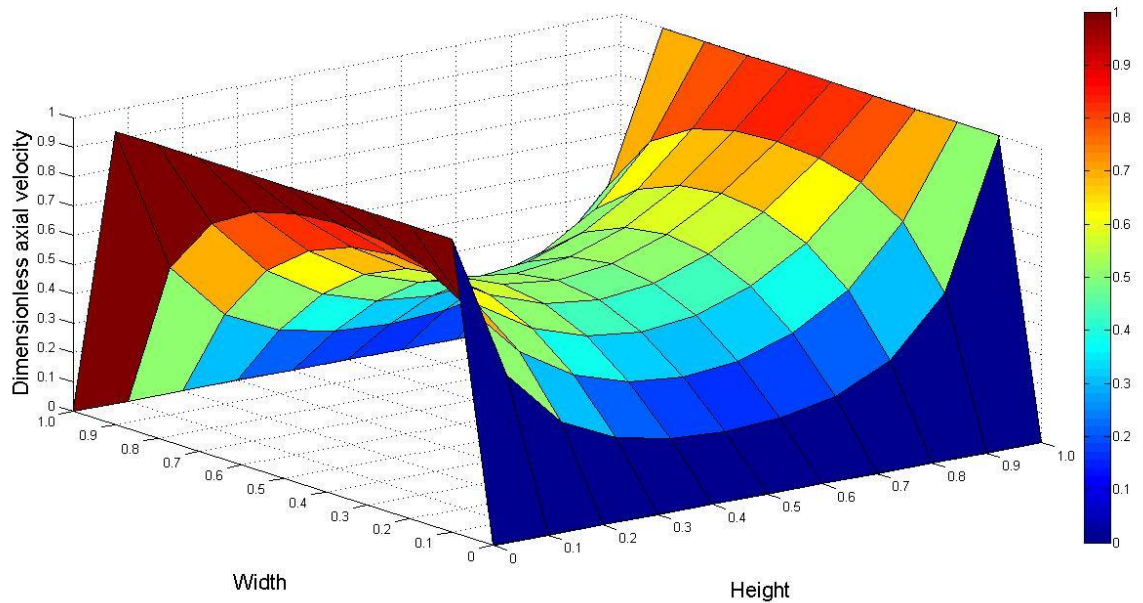


Fig. 6.24: The dimensionless axial velocity in the dimensionless X and Y axes for a double disk micropump. $\alpha=1.0$, $P_{in}=P_{out}=0.0$ Pa, $\omega=1000$ rpm, $\theta=270=270^\circ$.

In figure 6.24 above, the flow behavior of the fluid through the double disk microchannel is illustrated. In this figure, the two moving walls are at a unity dimensionless axial velocity while the other two walls are stationary (fixed).

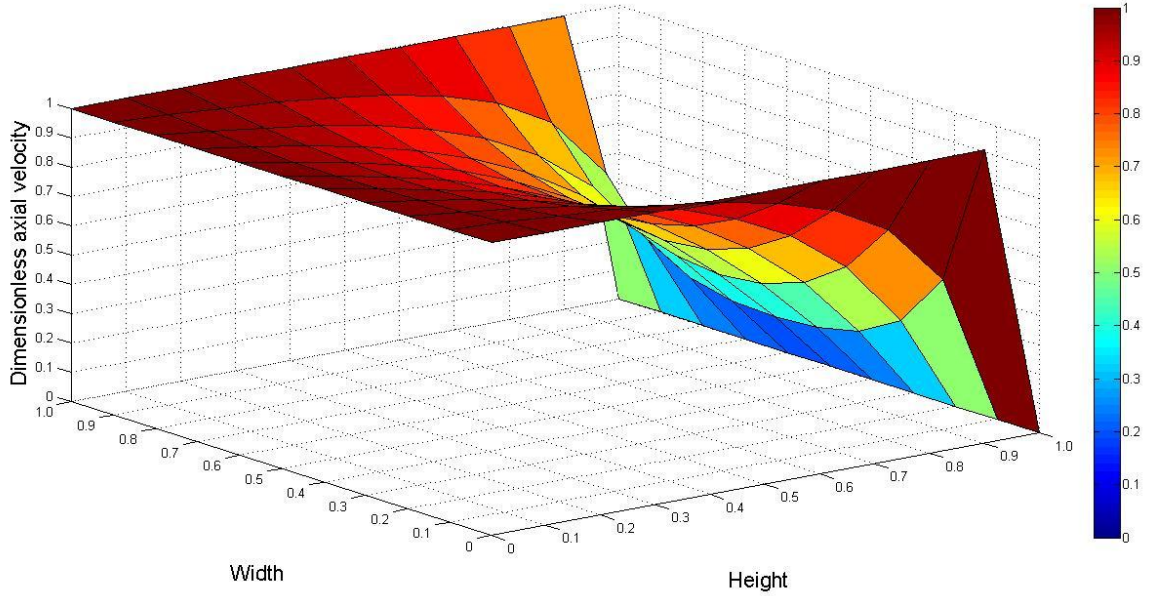


Fig. 6.25: The dimensionless axial velocity in the dimensionless X and Y axes for a spiral micropump. $\alpha=1.0$, $P_{in}=P_{out}=0.0$ Pa, $\omega=1000$ rpm, $\theta=270=270^\circ$.

While in figure 6.25, the flow behavior of the fluid through the spiral microchannel is illustrated. In this figure, the three moving walls are at a unity dimensionless axial velocity and the fourth wall of the spiral microchannel is stationary.

The transverse velocities in both dimensionless X and Y axes were investigated and found to be of order of 10^{-8} and the axial velocity is of order of one, the issue that clarifies the deletion of the transverse velocities when dealing with the impermeable wall boundary conditions. Below are the figures of the dimensionless velocities in the dimensionless X and Y axes respectively for the spiral micropump at a unity aspect ratio (See figures 6.26 and 6.27 below):

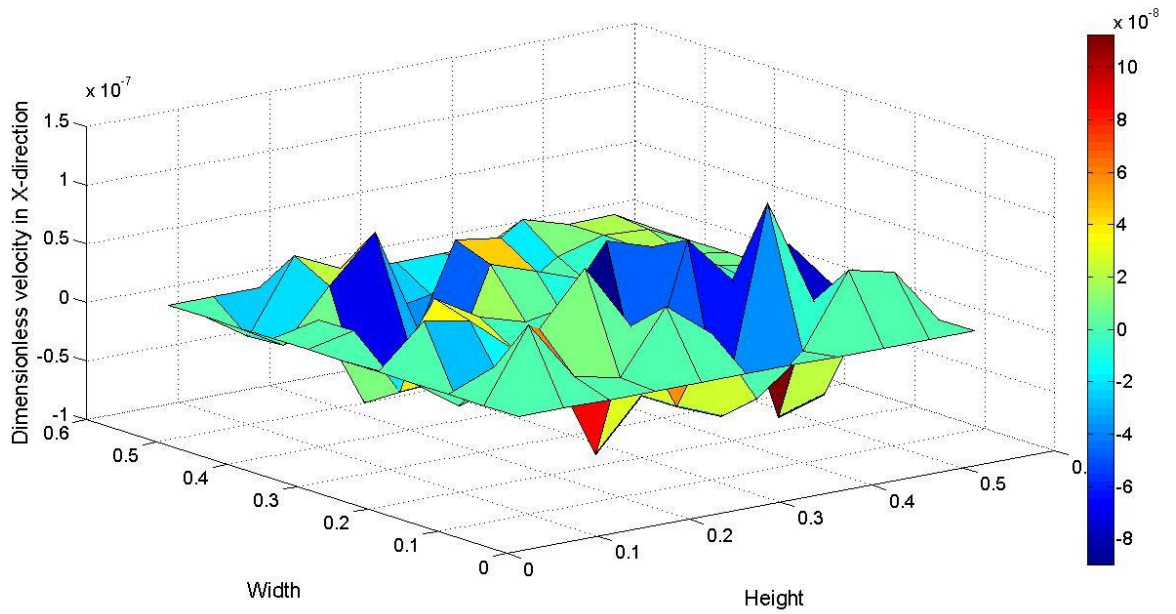


Fig. 6.26: The dimensionless velocity in X direction in the dimensionless X and Y axes for a spiral micropump. $\alpha=1.0$, $P_{in}=P_{out}=0.0$ Pa, $\omega=1000$ rpm, $\theta=270=270^\circ$.

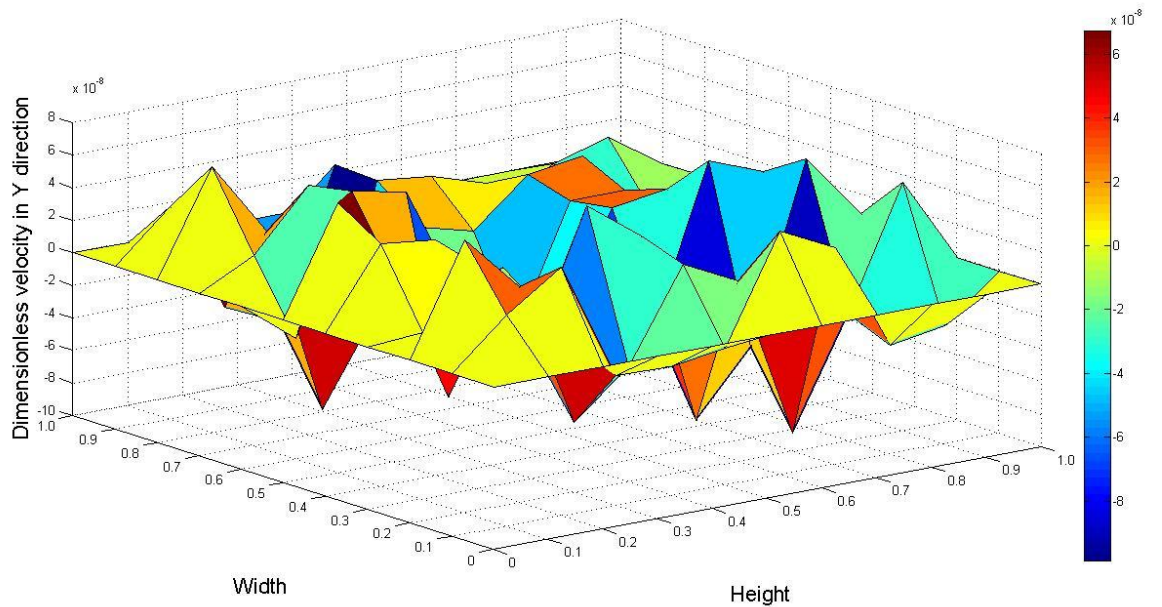


Fig. 6.27: The dimensionless velocity in Y direction in the dimensionless X and Y axes for a spiral micropump. $\alpha=1.0$, $P_{in}=P_{out}=0.0$ Pa, $\omega=1000$ rpm, $\theta=270=270^\circ$.

6.5. Single Disk, Double Disk and Spiral Channel Micropumps Performance

Curves

During the investigation of the three types of micropumps adopted in this study, it is found that the non-Newtonian blood dimensionless velocity behaves linearly when drawn with respect to the reduced Reynolds Euler, \overline{ReEu} . This parameter was firstly investigated [8] in order to show the spiral pump performance curves in the dimensionless format for Newtonian fluid at which it is found that the dimensionless velocity is a function of geometrical and pressure factors F_D and F_P respectively.

In this study it was found that the pump performance curves for the Herschel Bulkley fluid have a linear relationship when drawn with the Reynolds Euler, \overline{ReEu} which is given by the following equation:

$$\overline{ReEu} = \frac{h^{n+1}}{kW_{ave}^n} \times \frac{\partial P}{\partial Z} \quad (6.2)$$

The figures below shows the linear relationship of these performance curves for the three types of pumps:

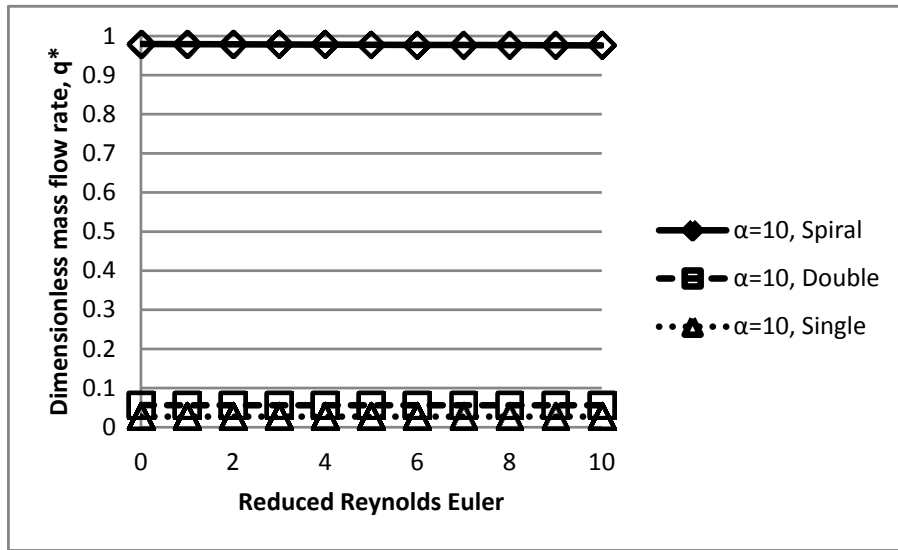


Fig. 6.28: Performance curves of the single disk, double disk and spiral micropumps represented by plotting the dimensionless flow rate .vs. the reduced Reynolds Euler number at an aspect ratio of ten.

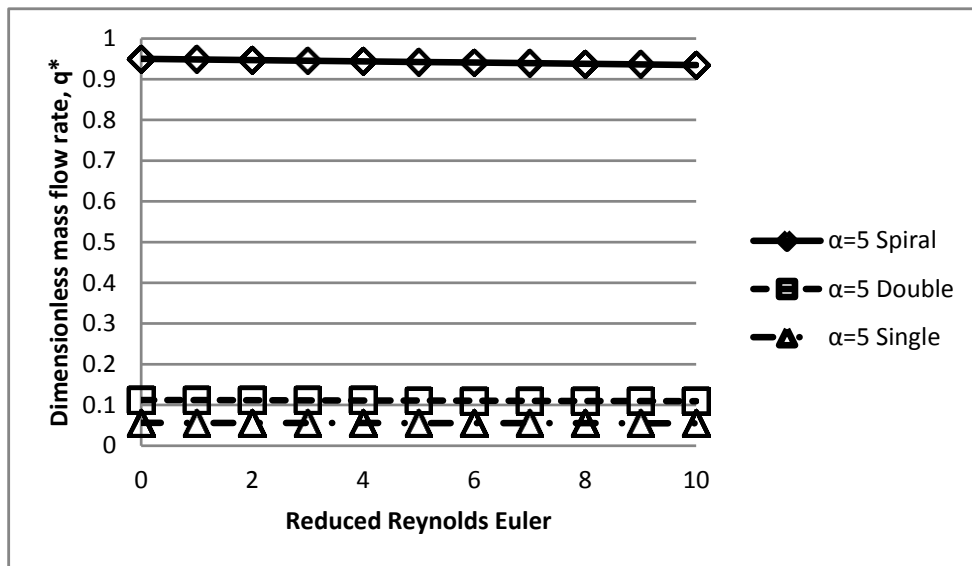


Fig. 6.29: Performance curves of the three types of micropumps .vs. the reduced Reynolds Euler number at $\alpha=5$.

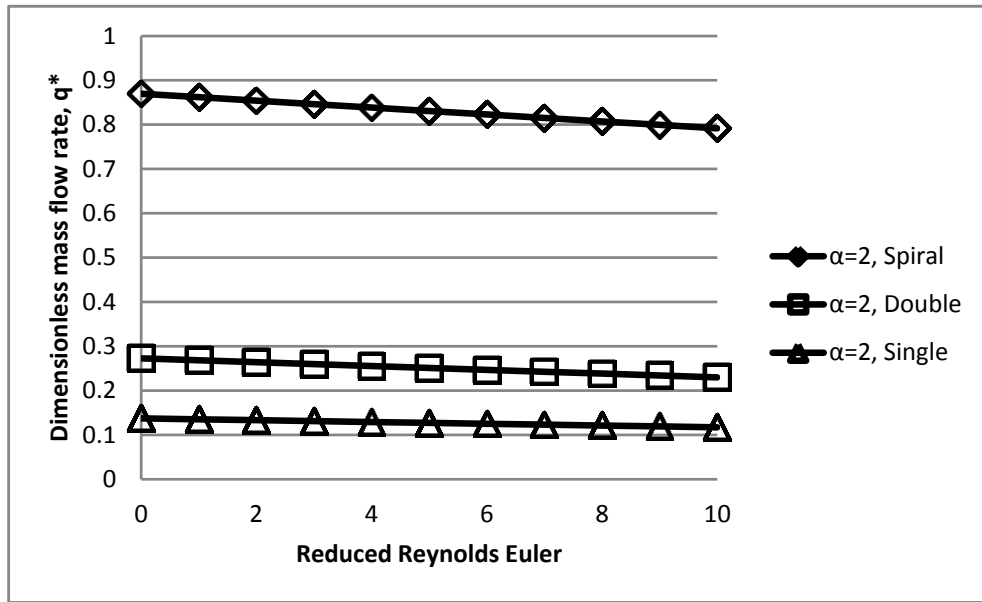


Fig. 6.30: Performance curves of the three types of micropumps .vs. the reduced Reynolds Euler number at $\alpha=2$.

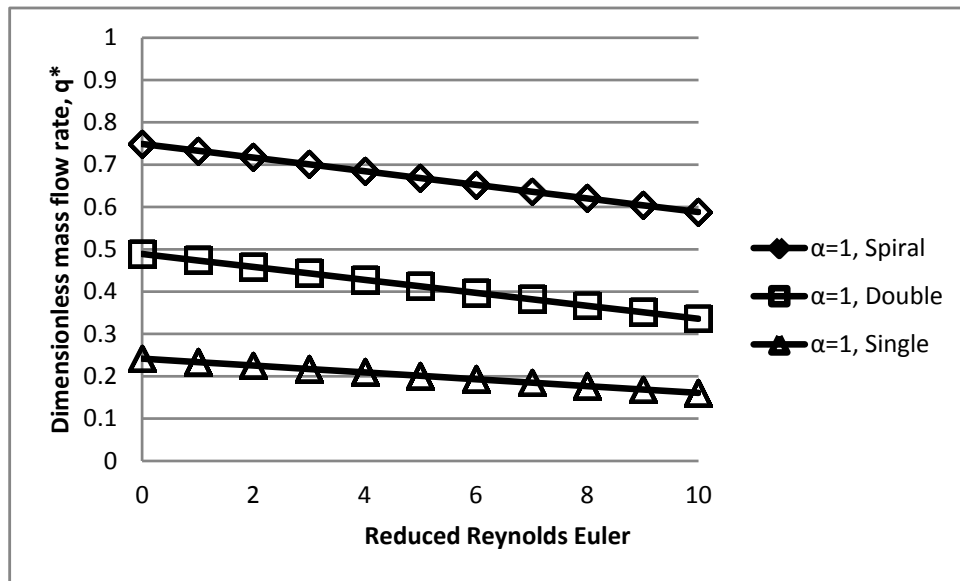


Fig. 6.31: Performance curves of the three types of micropumps .vs. the reduced Reynolds Euler number at $\alpha=1$.

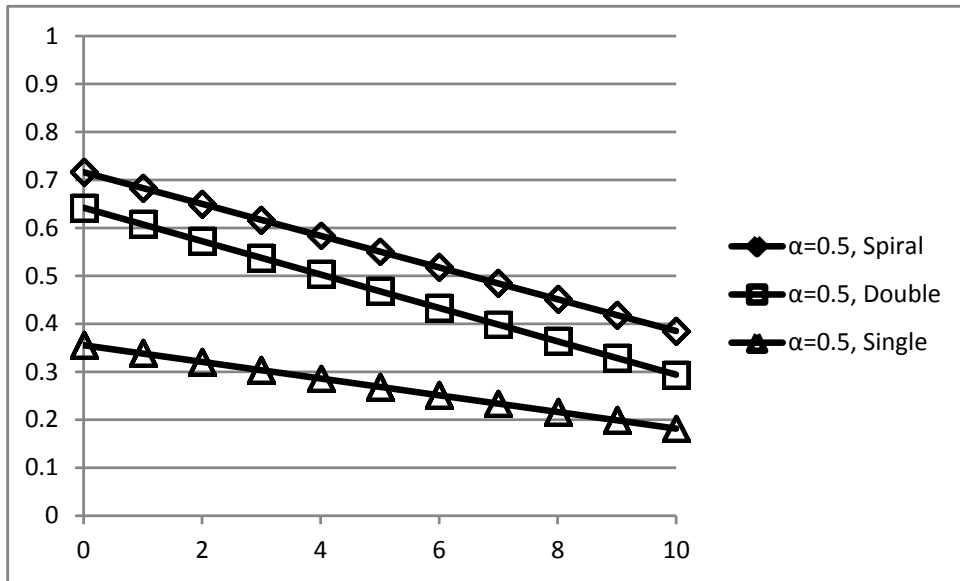


Fig. 6.32: performance curves of the three types of micropumps .vs. the reduced Reynolds Euler number at $\alpha=0.5$.

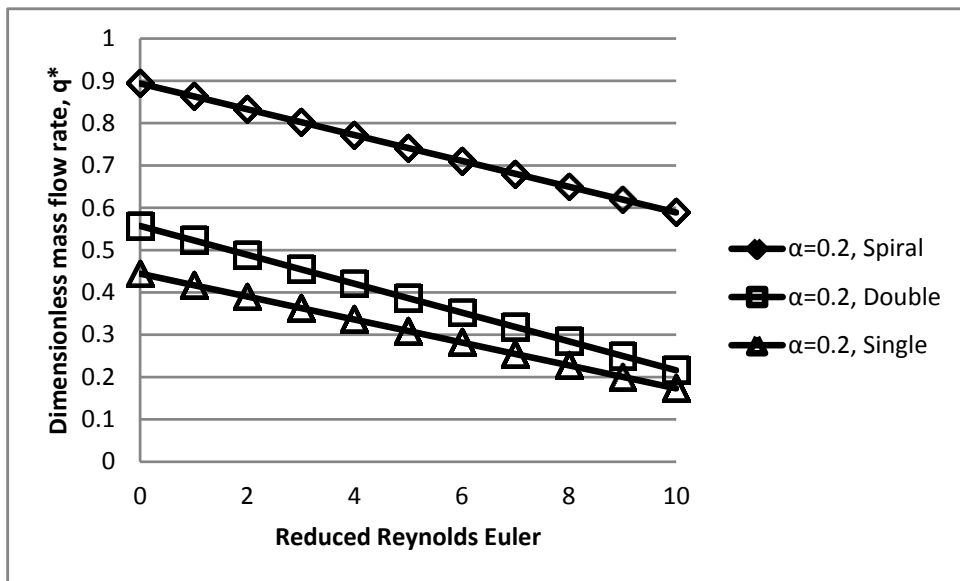


Fig. 6.33: Performance curves of the three types of micropumps .vs. the reduced Reynolds Euler number at $\alpha=0.2$.

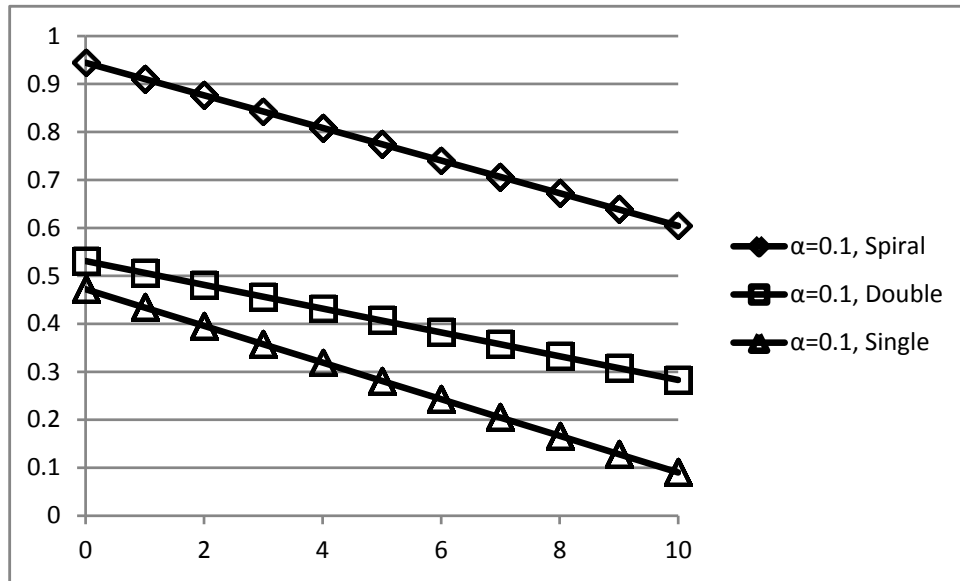


Fig. 6.34: Performance curves of the three types of micropumps .vs. the reduced Reynolds Euler number at $\alpha=0.1$.

In the figures from 6.28-34, it is really great to find a linear relationship that might be in future really helpful in establishing empirical linear formulas for the several non-Newtonian micropumps depending on their power law index, type of spiral micropump, and the consistency coefficient.

The Table below gives numerical values for the dimensionless mass flow rates shown in the figures above at different values of of generalized reduced Reynolds Euler number.

Table 6.6: Numerical values of the dimensionless mass flow rates .vs. generalized reduced Reynolds Euler number.

		Generalized Reduced Reynolds Euler Number, \overline{ReEu}						
		0	2	4	6	8	10	
Aspect Ratio, α	10	Spiral Channel	0.9797	0.9789	0.9781	0.9773	0.9765	0.9757
		Double Disk	0.0563	0.0562	0.0561	0.0561	0.0560	0.0559
		Single Disk	0.0272	0.0272	0.0272	0.0271	0.0271	0.0271
	5	Spiral Channel	0.9499	0.9469	0.9439	0.9409	0.9379	0.9349
		Double Disk	0.1122	0.1116	0.1110	0.1104	0.1098	0.1092
		Single Disk	0.0561	0.0559	0.0557	0.0555	0.0553	0.0551
	2	Spiral Channel	0.8697	0.8541	0.8385	0.8229	0.8073	0.7917
		Double Disk	0.2726	0.2640	0.2554	0.2468	0.2382	0.2296
		Single Disk	0.1371	0.1331	0.1291	0.1251	0.1211	0.1171
	1	Spiral Channel	0.7490	0.7168	0.6846	0.6524	0.6202	0.5880
		Double Disk	0.4890	0.4584	0.4278	0.3972	0.3666	0.3360
		Single Disk	0.2416	0.2254	0.2092	0.1930	0.1768	0.1606
	0.5	Spiral Channel	0.7161	0.6499	0.5837	0.5175	0.4513	0.3851
		Double Disk	0.6420	0.5724	0.5028	0.4332	0.3636	0.2940
		Single Disk	0.3556	0.3208	0.2860	0.2512	0.2164	0.1816
	0.2	Spiral Channel	0.8939	0.8329	0.7719	0.7109	0.6499	0.5889
		Double Disk	0.5571	0.4889	0.4207	0.3525	0.2843	0.2161
		Single Disk	0.4444	0.3902	0.3360	0.2818	0.2276	0.1734
	0.1	Spiral Channel	0.9444	0.8764	0.8084	0.7404	0.6724	0.6044
		Double Disk	0.5309	0.4813	0.4317	0.3821	0.3325	0.2829
		Single Disk	0.4722	0.3958	0.3194	0.2430	0.1666	0.0902

6.6. Shear stress analysis:

In this section, shear stress affecting the blood cells especially the red blood cells will be considered. During this study, the critical shear stresses that will cause damage to the blood cells will be listed. And finding whether the blood cells may reach that critical stress or not.

To start with the shear stress observed on the blood cells; the stress exposure time shall be calculated first. In order to find that time, the average fluid velocity will be divided on the channel length:

$$\text{Exposure time} = \frac{\text{Spiral channle length}}{\text{Average fluid velocity}} \quad (6.3)$$

In the following data, the radii of the different micropumps are of the same magnitude which is 0.001m, the rotational speed is 1000rpm and the angle of the spiral pumps is 3π . The following table summarizes shear stresses data applied on the blood cells:

Table 6.7: Wall shear stress for the currently studied micropumps at different aspect ratios, with the time needed for the fluid particle to travel through the micropump.

Wall Shear Stress, Pa				
α	Single Disk	Double Disk	Spiral Channel	Exposure Time, Sec
0.1	994.4923	993.4581	1.00E+03	9.43E-03
0.2	563.3336	562.7348	567.9416	9.43E-03
0.5	265.7326	265.4971	267.8913	9.43E-03
1	150.5047	150.1862	151.6405	9.43E-03

As I known the blood cell damage is a function of both wall shear stresses and the time at which these stresses are exerting on the blood cells. For the time above (which is about 1×10^{-2}) the needed stress to drive the blood cells to damage (i.e. the threshold level of RBC damage) is 5000 dynes/cm^2 which is equivalent to 500 Pa [55]. By considering this threshold level, the red blood cells might experience a damage in aspect ratio smaller than 0.2.

At last, to show the behavior of the wall shear stress, the dimensionless wall shear stress will be presented for the double disk micropump:

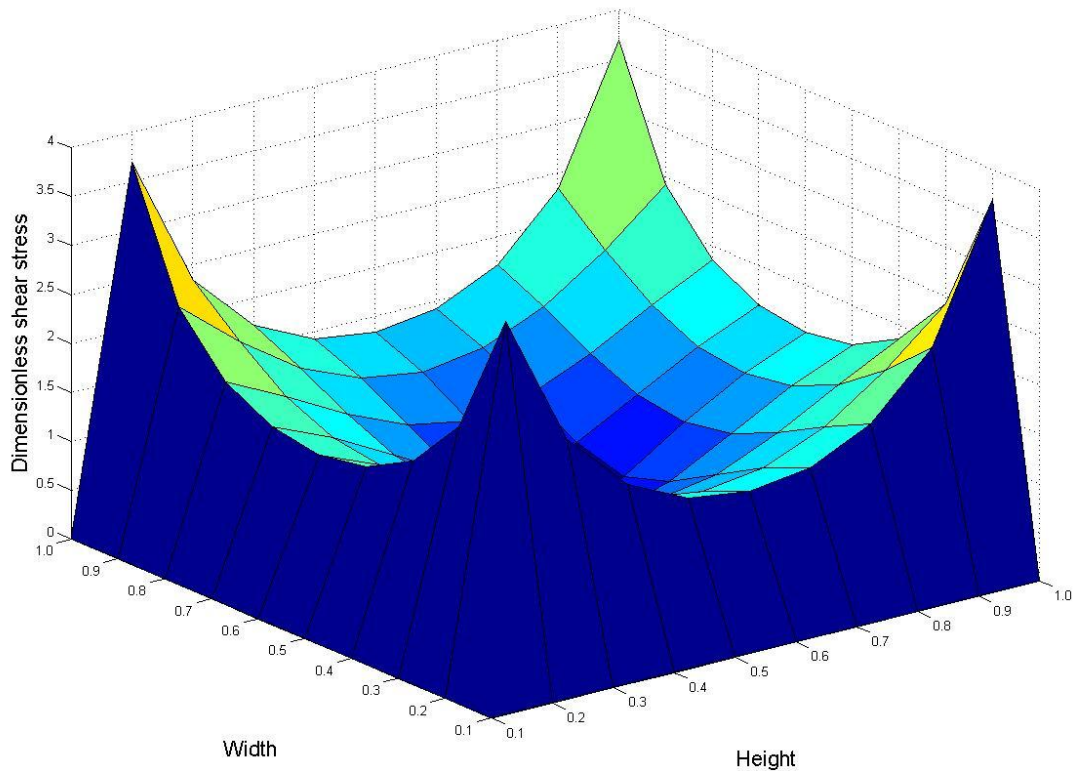


Fig.6.35: Dimensionless shear stress in double disk micropump through the channel cross sectional area, $\alpha=1$, $\Delta P=500 \text{ Pa}$, $R=1000 \times 10^{-6} \text{ m}$, $\theta=3\pi$.

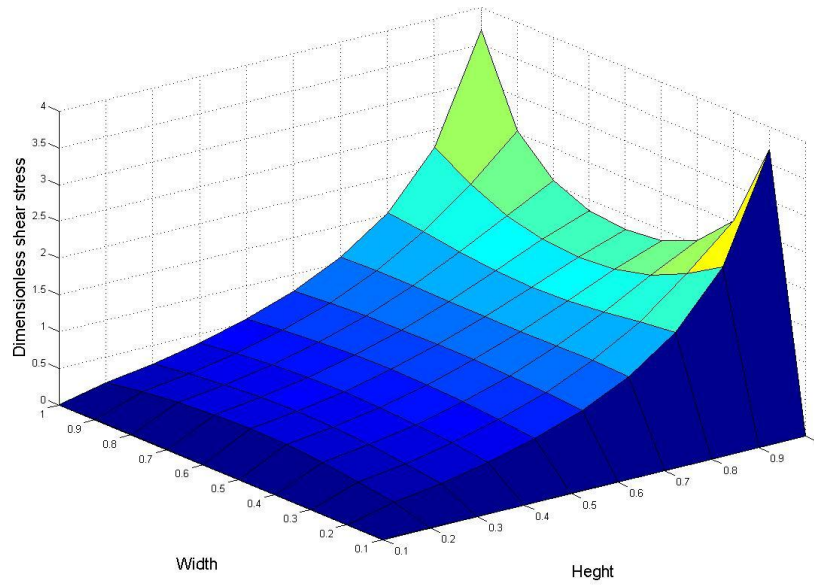


Fig.6.36: Dimensionless shear stress in Single disk micropump through the channel cross sectional area, $\alpha=1$, $\Delta P=500$ Pa, $R=1000 \times 10^{-6}$ m, $\theta=3\pi$.

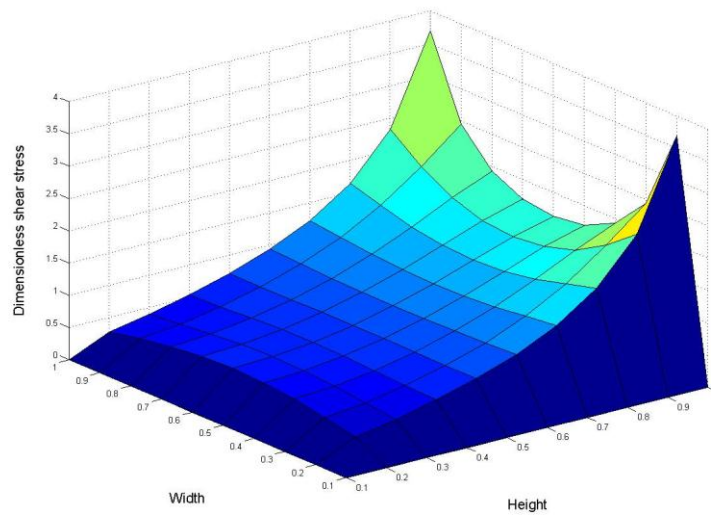


Fig.6.37: Dimensionless shear stress in spiral channel micropump through the channel cross sectional area, $\alpha=1$, $\Delta P=500$ Pa, $R=1000 \times 10^{-6}$ m, $\theta=3\pi$.

As shown figure 6.35, the double disk micropump has four regions of maximum wall shear stress and this is because of the fact that the double disk micropump has four

corners at which a moving wall is adjacent to a stationary wall. While both of the spiral channel micropump and the single disk micropump have two spots of maximum wall shear stress. From the above figure it can be figured easily that the quantity that might be damaged in the double disk micropumps is twice of that might be damaged in either single disk or spiral channel micropumps.

CHAPTER 7

Conclusions and Recommendations

7.1. Conclusions

With the growing importance of genomics, proteomics, and the discovery of new drugs, controlled transport of fluids in microscale becomes an important and crucial task. This controlled transport of the fluid includes a well study of the used type of micropump and implementing the exact accurate fluid flow model that is related to the working fluid going to be transported in such type of micropumps. Accordingly, the main core of this work was comparing three types of the commonly used micropumps in the biomedical applications and then implementing the Herschel-Bulkley non-Newtonian fluid flow model in order to accurately simulate the exact nature of blood flow through these pumps.

In this work, a literature survey to the previous related works is discussed in chapter two. This is followed by clarifying several mathematical and numerical theories that will deeply help solving the current problem. The mathematical modeling and the governing equations were derived in the third chapter. In order to reach to this stage of the fully derived equations; number of assumptions such as having a fully developed steady incompressible flow and assuming that the fluid flow behaves as a Herschel Bulkley non-Newtonian fluid flow. Then the results were illustrated through using both finite difference method FDM at which a dedicated MATLAB code was written to the present problem and finite volume method FVM at which the geometry of the studied cases was drawn and meshed using the GAMBIT and then the problem was solved in

FLUENT software after introducing the boundary conditions and other needed constants.

In order to ensure that both of methods of solution that were based on FDM and FVM are providing good accurate results; results from both methods were compared to the Newtonian analytical solution as a special case of the present work of course these results were compared after attaining the optimum mesh size or what is called mesh independent solution. While investigating these results it was noted that the Newtonian runs of the present work were in a very good matching the analytical solution. After that the effect of changing the power law index was investigated, and it is found that as the flow goes from shear thinning at which the value of the power law index is lower than one through shear thickening at which the power law value is more than one passing through the Newtonian fluid flow at which we have a unity power law index value; it was noted that the dimensionless axial velocity has an inverse proportionality with the power law index, in another way, the mass flow rate pumped with a fluid with lower power law index value is higher than that pumped with the fluid with higher power law index value. For example, the mass flow rate was increased with about 25% between using a fluid with a unity power law index, such as Newtonian fluids, and fluids with power law index of 0.7 values. This also means, if we are dealing with a fluid that is non-Newtonian -Such as the blood in the present work- and assuming that the blood is Newtonian then we will end up with an access amount of pumped blood as we are entering extra power to overcome the extra amount of viscosity that is assumed by adopting the Newtonian fluid flow assumption while in the truth, the real viscosity is less than that. Noting that the importance of knowing the exact values of the power law indices and the real behavior of the fluid is of a great importance especially in the

applications at which the mass flow rate is needed to be very precise such as the micro and nano-scale fluid flow applications. Furthermore, the effect of aspect ratio on fluid flow was investigated side by side finding out the performance curves of the micropumps that were under investigation.

An experimental study was performed on two spiral channel micropumps at which the obtained results were good but not that accurate due to the observed losses during running the experiment. A statistical uncertainty analysis was performed on the obtained experimental data and found that the readings are almost about $\pm 0.2 \times 10^{-6}$ accurate while the readings are of order 10^{-5} , i.e the error in readings is in the first decimal digit; the matter that is found to be accepted. The experimental results were used to provide extra validating methodology to the present work at which the behavior of the obtained experimental results show a very good agreement with the expected flow behavior for both Newtonian and non-Newtonian fluids as for example the mass flow rate of the blood mimicking fluid (non-Newtonian fluid with power law index less than one) is noticed to be bigger than that obtained for distilled water at the same operating conditions.

Finally, the shear stress analysis was performed on the cases considered in this study and found that the blood might strongly experience RBC damage in the three types of micropumps when the aspect ratio equals or below 0.2. Furthermore, it is noticed that the values of the damaged blood might be the double of single disk and spiral channel micropumps if we were using a double disk micropump, the reason behind that is explained by the fact that the double disk micropumps have four spots of

maximum wall shear stress while having only two spots of maximum shear stress in both single disk and spiral channel micropumps.

After observing the performance of the three adopted types of micropumps and the Herschel-Bulkley fluid flow model the following can be concluded:

- It is necessary to adopt the exact model of the fluid flow in order to exactly predict the amount of low rate. This issue will give the following benefits:
 1. Using less power to drive the micropump: by this, smaller batteries will be required to be installed in the devices to do the same function.
 2. Fewer controllers are needed: knowing the exact flow behavior of the fluid flow will result less number of controllers to be installed on the device to control the flow becomes less.
 3. Smaller device sizes: smaller sizes for the devices will be manufactured as the number of the controllers become fewer and the power source become smaller.
 4. Cheaper devices: the devices will become cheaper also due to the fewer number of controllers and the smaller power source.
- It is noted that the spiral micropump is of the best performance characteristics as the fluid flow can be controlled much better than the other two adopted types of micropumps with minimum spots of maximum wall shear stress.

7.2. Recommendations

One of the marvelous results observed in this study is that when studying the relationship between the reduced Reynolds Euler numbers while adopting the generalized Reynolds number gave a linear relationship with the dimensionless mass flow rate. Actually a good and a strong effort shall be done in the future work in order to study this issue in more details and finding out several empirical formulas that will govern this type of non-Newtonian fluid flow .

References

1. Yun Kwang-Seok and Yoon Euisik (2005), Micropumps for MEMS/NEMS and Microfluidic Systems. **MEMS/NEMS Handbook**, Springer.
2. Al-Halhouli A., "Numerical Simulation of the Flow Field in A Spiral Micropump" **PhD Thesis, University of Jordan**, May 2007.
3. Gravesen, P., Brandebjerg, J. and Sondergard Jensen J.(1993). Microfluidics-a review. **Journal of Micromechanics and Microengineering** , 3, 168-182.
4. Olsson, A.(1998). Valve-Less Diffuser Pumps for Liquids. TRITA-IL-9603, **Licentiate of Engineering**. Royal Institute of Technology.
5. Gad-el-Hak, M.(1999). The fluid mechanics of microdevices-the Freeman scholar lecture. **Journal of fluids engineering**, 121, 5-33.
6. Kilani, M. I., Galambos, P. C., Haik, Y. S. and Chen, C. J. (2003). Design and analysis of a surface micromachined spiral-channel viscous pump.
7. **Journal of Fluids Engineering**, Transactions of the ASME, 125, 339-344.
8. Kilani M. I., Al-Halhouli A. T. , Al-Salaymeh A., and Büttgenbach S., “Viscous micropumps_A review,” **International Conference on Biotechnology: Future Prospects**, Emirates, Al Ain, UAE, 2006.
9. Kilani M. I., Al-Salaymeh A., and Al-Halhouli A. T.i, “Effect of channel aspect ratio on the flow performance of a spiral-channel viscous micropump,” **Journal of Fluids Engineering**, Transactions of the ASME, Vol. 128, pp. 618-627, 2006.
10. Al-Halhouli A. T., Kilani M. I., Al-Salaymeh A., and Büttgenbach S., “Influence of geometrical design parameters on the flow performance of a spiral channel viscous micropump,” **WSEAS Transactions on Fluid Mechanics**, Vol. 1, No. 6, pp. 601-606, 2006.
11. Al-Halhouli A. T., Al-Salaymeh A., Kilani M. I., and Büttgenbach S, “Numerical investigation of the effect of spiral curvature on the flow field in a spiral-channel viscous micropumps,” **Microfluidics Nanofluidics**, Vol. 3, pp. 537-546, 2007.
12. Al-Halhouli A. T., Kilani M. I., Al-Salaymeh A., and Büttgenbach S., “Investigation of the influence of design parameters on the flow performance of single and double disk viscous micropumps,” **Microsystem Technologies**, Vol. 13, pp. 677-687, 2007.

13. Blanchard D., Ligrani P., and Gale B., "Single-disk and double-disk viscous micropumps," **Sensors and Actuators A**, Vol. 122, pp. 149-158, 2005.
14. Blanchard D., Ligrani P., and Gale B and Harvey I., "Micro-structure mechanical failure characterization using rotating Couette flow in a small gap," **Journal of Micromechanics and Micro-engineering**, Vol. 15, pp. 792-801, 2005b.
15. Blanchard D. and Ligrani P., "Comparisons of different viscous pumps based on physical behavior," **Sensors and Actuators A**, Vol. 126, pp. 83-92, 2006.
16. Blanchard D. and Ligrani P., "Micro-scale and millimeter-scale rotating disk Couette flows, experiments and analysis," **Experiments in Fluids**, Vol. 41, pp. 893-903, 2006b.
17. Blanchard D. and Ligrani P., "Microscale disk-induced gas displacement with and without slip," **Journal of Micromechanics and Micro-engineering**, Vol. 17, pp. 2108-2117, 2007.
18. Al-Halhouli A. T., Kilani M. I., Al-Salaymeh A., and Büttgenbach S., "Numerical investigation of the effect of spiral curvature on the flow field in a spiral-channel viscous micropumps," **Microfluidics Nanofluidics**, Vol. 3, pp. 537-546, 2007.
19. Sen M., Wajerski D., and Gad-El-Hak M., "A novel pump for MEMS applications," **Journal of Fluids Engineering, Transactions of the ASME**, Vol. 118, No. 3, pp. 624-627, 1996.
20. Day, R. and Stone, H. (2000). Lubrication analysis and boundary integral simulations of a viscous micropump. **Journal of Fluid Mechanics**, 416, 197-216.
21. DeCourtye, D., Sen, M., and Gad-el-Hak, M. (1998). Analysis of viscous micropumps and microturbines. **International Journal of Computational Fluid Dynamics**, 10, 13-25.
22. Abdelgawad, M., Hassan, I., and Esmail, N. (2004). Transient behavior of the viscous micropump. **Microscale Thermophysical Engineering**, 8, 361-381.
23. Phutthavong, P., and Hassan, I. (2004). Transient performance of flow over a rotating object placed eccentrically inside a microchannel numerical study. **Microfluid Nanofluid**, 71-85.
24. Abdelgawad, M., Hassan, I., Esmail, N. and Phutthavong, P. (2005). Numerical investigation of multistage viscous micropump configurations. **Journal of Fluids Engineering**, 734-742.

25. Shah, R.K., and Bhatti, M.S. (1987) "Laminar Convective Heat Transfer in Ducts," in **Handbook of Single Phase Convective Heat Transfer** (S. Kakac, R.K. Shah, and W. Aung, Eds.), Chapter 3, John Wiley & Sons, New York.
26. Arkilic, E. B. & Breuer, K. S. 1993 Gaseous flow in microchannels. AIAA Paper 93-3270.
27. Arkilic, E. B., Schmidt, M. A. & Breuer, K. S. 2001 Slip flows and tangential momentum accommodation in micromachined channels. **J. Fluid Mech.** 437, 29–43.
28. Gad-el-Hak, M. (1999). The fluid mechanics of microdevices- the freeman scholar lecture. **Journal of Fluids Engineering**, Transactions of the ASME, 121:5-33. Gonzalez, U. (2001). Modeling and simulating MEMS devices using finite volume analysis. **Proceedings of 2001 ASME International Mechanical Engineering Congress and Exposition**. New York, USA.
29. McDonald, D.A., 1974, Blood flow in Arteries, 2nd Ed., Arnold, London.
30. Liepsch, D. and Morvec, S 1984, "Pulsatile flow of non-Newtonian blood flow at the aortic bifurcation", **J. of Biomechanics**, 26, 37-49.
31. Ku, D.N. and Liepsch D., 1986, "The effect of non-Newtonian viscoelasticity and wall elasticity on flow at a 90 degree bifurcation", **Biorheology**, 23, 359-370.
32. Theodorou, G. Bellet, D., 1986 "Laminar flows of a non-Newtonian fluid in mild stenosis", **Comp. Meth. Appl. Mech. Eng.** 54, 111–123.
33. Nakamura, M, Swada, T., 1988, "Numerical study on the flow of a non-Newtonian fluid through an axisymmetric stenosis", **J. Biomech. Eng. Trans ASME**, 110, 137–143.
34. Pak, B., Young Y.I., and Choi, S.U.S., 1990, "Separation and re-attachment of non-Newtonian fluid flows in a sudden expansion pipe", **J. Non-Newtonian Fluid. Mech.** 37 175–199.
35. Das, B., Johnson, P.C., and Popel, A.S., 1998, "Effect of nonaxisymmetric hematocrit distribution on non-Newtonian blood flow in small tubes", **Biorheology** 35, 69–87.
36. Gijzen, F.J.H., van de Vosse, and F.N., Janssen, J.D., 1999, "The influence of the non-newtonian properties of blood on the flow in large arteries: steady flow in a carotid bifurcation model", **Journal of Biomechanics** 32, 601–608.
37. Gijzen, F.J.H., van de Vosse, F.N., and Janssen, J.D., 1999, "The influence of the non-Newtonian properties of blood on the flow in large arteries: unsteady flow in a 90° curved tube", **Journal of Biomechanics** 32, 705–713.

38. Hussain M.A., Subir Kar and Puniyani, R.R., 1999, "Relationship Between Power Law Coefficients And Major Blood Constituents Affecting The Whole Blood Viscosity", **J. of Biosciences**, Vol. 24, No.3, 329-337.
39. Buchanan Jr. J.R., Kleinstreuer C., and Comer J.K., 2000, "Rheological effects on pulsatile hemodynamics in a stenosed tube", **Computers & Fluids**, Vol. 29, 695-724.
40. Shalman, E., Rosenfeld, M., Dgany, E., and Einav. S., 2001, "Numerical modeling of the flow in stenosed coronary artery. The relationship between main hemodynamic parameters", **Computers in Biology and Medicine**, 32, 329-344.
41. Neofytou, P. and Drikakis, D., 2003, "Non-Newtonian flow instability in a channel with a sudden expansion", **J. of Non-Newtonian Fluid Mechanics**, 111, 127-150.
42. Chen, J., Lu, X.Y., 2004, "Numerical investigation of the non-Newtonian blood flow in a bifurcation model with a non-planar branch", **Journal of Biomechanics**, 37, 1899-1911.
43. Mandal P.K., 2005, "An unsteady analysis of non-Newtonian blood flow through tapered arteries with a stenosis", **Int. J. of Non-Linear Mechanics**, 40, 151-164.
44. Beebe DJ, Mensing GA, Walker GM. Physics and applications of microfluidics in biology. **Ann Rev Biomed Eng.** 2002a; 4:261–286.
45. Ho, C. M. & Tai, Y. C. 1998 Micro-electro-mechanical systems (MEMS) and fluid flows. **A. Rev. Fluid Mech.** 30, 1-33.
46. Hetsroni, G., Mosyak, A., Pogrebnyak, E. and L.P. Yarin, L.P., 2005, Heat Transfer in Micro-Channels: Comparison of Experiments with Theory and Numerical Results, **Int. J. Heat Mass Transfer**, 48, 5580-5601.
47. Bahrami, M., Yovanovich, M.M., Culham, J.R., 2005, Pressure drop of laminar, fully developed flow in rough microtubes, **ASME Journal of Fluids Engineering** 128, 632-637.
48. Syrjälä, S., "Laminar flow of viscoelastic fluids in rectangular ducts with heat transfer: A finite element analysis," **Int. Commun. Heat Mass Transfer**, 25, 191–204_1998.
49. Syrjälä, S., "Numerical Study of Fully developed non-Newtonian Fluid Flow and heat Transfer in a Rectangular Channel with Moving Walls", **Int. Commun. Heat Mass Transfer**, 24, 11-25.
50. Patankar. V, Pratavp. S. & Spaldngd, B. 1974 Prediction of laminar flow and heat transfer in helically coiled pipes. **J. Fluid Mech.** 62, 539-551.
51. Patankar, S.V. (1980). Numerical Heat Transfer and Fluid Flow, McGraw-Hill Book Company, New York.

52. Harlow, F., and Welch, J., 1965. "Numerical calculation of time-dependent viscous incompressible flow of fluid with a free surface". **The physics of fluids**, 8, 2128.
53. Büttgenbach, S., Balck, A., Demming, S., Lesche, C., Michalzik, M., and Al-Halhouli A.T., "Development of on Chip Devices for Life Science Applications", **International Journal of Engineering**, 2009, 1-11.
54. Al-Halhouli A.T., Recent Advances in On-disk Viscous Micropumps, Journal of International Microelectronics And Packaging Society, 2010, 6, 1-9.
55. Leverett L.B., HELLUMS J.D., ALFREY C.P. and LYNCH E.C., Red Blood Cell Damage by Shear Stress, **Biophysical Journal**, 1972, 12, 257-273.
56. Anderson J, JR, Computational Fluid Dynamics, McGraw-Hill, 1995.
57. Qayum S., "Modeling of blood flow in a time varying shape passage" M.Sc. Thesis, King Fahd University of Petroleum and Mineral, April 2005.

Appendix

```

clear
%%%%%%%%%%%%%%%%%%%%%%%%%%%%%%%%%%%%%%%%%%%%%%%%%%%%%%%%%%%%%%%%%%%%%%%%
%Solving for SPIRAL DISK micropump, while considering the pressure
% velocity coupling.
%%%%%%%%%%%%%%%%%%%%%%%%%%%%%%%%%%%%%%%%%%%%%%%%%%%%%%%%%%%%%%%%%%%%%%%%
% The input parameters
%%%%%%%%%%%%%%%%%%%%%%%%%%%%%%%%%%%%%%%%%%%%%%%%%%%%%%%%%%%%%%%%%%%%%%%%
%
L=30e-6;% Width of the channel in meter
alpha=1.0; % Aspect ratio
rpm=1000; % The dimensional motor rotational speed in rpm.
Pout=500; % The dimensional outlet pressure in Pa.
Pin=0.0; % The Dimensional inlet pressure
Angle=44/7; % Angle of the channel in rad.
Rin=1000e-6; % Inlet radius of the channel in m.
Rout=1020e-6;% Outlet radius of the channel in m.
Minerror=1e-7; % Convergence criteria (min. error).
%
%%%%%%%%%%%%%%%%%%%%%%%%%%%%%%%%%%%%%%%%%%%%%%%%%%%%%%%%%%%%%%%%%%%%%%%%
% These parameters are necessary for solution and defined by computer
% DON'T CHANGE ANY THING BELOW
%%%%%%%%%%%%%%%%%%%%%%%%%%%%%%%%%%%%%%%%%%%%%%%%%%%%%%%%%%%%%%%%%%%%%%%%
%
% For the channel x-section
Lx=1.0; h=0.1*alpha*Lx; Ly=alpha*Lx;
% For gridding purposes
Nx=Lx/h; Ny=Ly/h; Nx=round(Nx); Ny=round(Ny);
% Blood properties
n=0.82; tau0=3.15e-3; rho=1052; m=7.95e-3;
% For Iteration purposes
SOR=0.25;
% For the panelt folmulation
kappa=1e9;
% Numbers evaluated from the inputs
Ra=(Rout+Rin)/2; % Average radius of rotation.
le=Angle*Ra; % Length of the channel in m.
w0=rpm*(44/7)*Ra/60; % Average channel velocity in m/sec.
tawd=tau0/(m*(w0/L)^n); % Amended Hesrchel Bulkley yield stress (see
deriv.)
Poutstar=(Pout*L^n)/(m*(w0^n)); %Dimensionless outlet pressure.
Pinstar=(Pin*L^n)/(m*(w0^n)); %Dimensionless inlet pressure.
lestar=le/L; % Dimensionless channel length.
dPmdz=(Pout-Pin)/le; % Dimensional axial pressure gradient.
dPmdzstar=(dPmdz*L^(n+1))/(m*w0^n);
Wstar=1.0; % Dimensionless average channel velocity.
%
%%%%%%%%%%%%%%%%%%%%%%%%%%%%%%%%%%%%%%%%%%%%%%%%%%%%%%%%%%%%%%%%%%%%%%%%
% Defining sizes of the used matrices
%%%%%%%%%%%%%%%%%%%%%%%%%%%%%%%%%%%%%%%%%%%%%%%%%%%%%%%%%%%%%%%%%%%%%%%%
%
OW=zeros(Nx+1,Ny+1); % For old values of W*
NW=zeros(Nx+1,Ny+1); % For new values of W*
OU=zeros(Nx+1,Ny+1); % For old values of U*
NU=zeros(Nx+1,Ny+1); % For new values of U*
OV=zeros(Nx+1,Ny+1); % For old values of V*
NV=zeros(Nx+1,Ny+1); % For new values of V*

```

```

gammadotstar=zeros (Nx,Ny); % To Evaluating the dimensionless strain
rate
mue=zeros (Nx,Ny); % For the dimensionless viscosity matrix.
Error1=zeros (Nx,Ny); % To find the error in W*.
Error2=zeros (Nx,Ny); % To find the error in U*.
Error3=zeros (Nx,Ny); % To find the error in V*.
Aveerror1=zeros (Nx,Ny); % To find the total average error of the
velocities
dW=zeros (Nx,Ny);
dU=zeros (Nx,Ny);
dV=zeros (Nx,Ny);
%
%%%%%%%%%%%%%%%%%%%%%%%%%%%%%%%%%%%%%%%%%%%%%%%%%%%%%%%%%%%%%%%%%%%%%%%%
% Defining the boundary conditions and the initial guessed
dimensionless velocities. U*, V* and W*
%%%%%%%%%%%%%%%%%%%%%%%%%%%%%%%%%%%%%%%%%%%%%%%%%%%%%%%%%%%%%%%%%%%%%%%%
%
for j=2:Ny
    for i=2:Nx
        % For the W*.
        OW(1,j)=Wstar; % Left edge of the channel.
        OW(Nx+1,j)=Wstar; % Right edge of the channel.
        OW(i,1)=Wstar; % Bottom edge of the channel.
        OW(i,Ny+1)=0; % Top edge of the channel.
        OW(Nx+1,Ny+1)=0; % Top right corner.
        OW(1,Ny+1)=0; % Top Left corner.
        OW(1,1)=Wstar; % Bottom left corner.
        OW(Nx+1,1)=Wstar; % Bottom right corner.
        OW(i,j)=Wstar+1e-5;%Initial guessed value DON'T CHANGE
        % For the U*
        OU(1,j)=0; % Left edge of the channel.
        OU(Nx+1,j)=0; % Right edge of the channel.
        OU(i,1)=0; % Bottom edge of the channel.
        OU(i,Ny+1)=0; % Top edge of the channel.
        OU(Nx+1,Ny+1)=0; % Top right corner.
        OU(1,Ny+1)=0; % To Left corner.
        OU(1,1)=0; % Bottom left corner.
        OU(Nx+1,1)=0; % Bottom right corner.
        OU(i,j)=Wstar+1e-5;%Initial guessed value DON'T CHANGE
        % For the V*
        OV(1,j)=0; % Left edge of the channel.
        OV(Nx+1,j)=0; % Right edge of the channel.
        OV(i,1)=0; % Bottom edge of the channel.
        OV(i,Ny+1)=0; % Top edge of the channel.
        OV(Nx+1,Ny+1)=0; % Top right corner.
        OV(1,Ny+1)=0; % To Left corner.
        OV(1,1)=0; % Bottom left corner.
        OV(Nx+1,1)=0; % Bottom right corner.
        OV(i,j)=Wstar+1e-5;%Initial guessed value DON'T CHANGE
    end
end
%
%%%%%%%%%%%%%%%%%%%%%%%%%%%%%%%%%%%%%%%%%%%%%%%%%%%%%%%%%%%%%%%%%%%%%%%%
% Starting the proble programming
%
%%%%%%%%%%%%%%%%%%%%%%%%%%%%%%%%%%%%%%%%%%%%%%%%%%%%%%%%%%%%%%%%%%%%%%%%
%
iteration=0; % For Counting the neede number of iterations.

```

```

Aveerror=100;% Random value which is grater thn the min. error
while (Aveerror>=Minerror & iteration<=7e3)
    iteration=iteration+1;
%%%%%%%%%%%%%%%%%%%%%%%%%%%%%%%%%%%%%%%%%%%%%%%%%%%%%%%%%%%%%%%%%%%%%%%%
    % To evaluate the viscosity matris at an earlier stage.
%%%%%%%%%%%%%%%%%%%%%%%%%%%%%%%%%%%%%%%%%%%%%%%%%%%%%%%%%%%%%%%%%%%%%%%%
    %
    for j=2:Ny
        for i=2:Nx
            %
            % Evaluating the stain rate
            %
            gammadotstar(i,j)=(1/(2*h))*(2*(OU(i+1,j)-OU(i-
1,j))^2)+(2*(OV(i,j+1)-OV(i,j-1))^2)...
                +((OU(i,j+1)-OU(i,j-1)+OV(i+1,j)-OV(i-1,j))^2)...
                +((OW(i+1,j)-OW(i-1,j))^2)+((OW(i,j+1)-OW(i,j-
1))^2))^0.5;
            if gammadotstar(i,j)==0.0
                gammadotstar(i,j)=1e-5;
            end
            %
            % Evaluating the viscous term.
            %
            mue(i,j)=((gammadotstar(i,j))^(n-
1))+tawd/gammadotstar(i,j);
        end
    end
%%%%%%%%%%%%%%%%%%%%%%%%%%%%%%%%%%%%%%%%%%%%%%%%%%%%%%%%%%%%%%%%%%%%%%%%
    % To find the new velocity values
%%%%%%%%%%%%%%%%%%%%%%%%%%%%%%%%%%%%%%%%%%%%%%%%%%%%%%%%%%%%%%%%%%%%%%%%
    %
    for j=2:Ny
        for i=2:Nx
            %
            if mue(i,j)==0.0
                mue(i,j)=1e-6;
            end
        end
    end
%%%%%%%%%%%%%%%%%%%%%%%%%%%%%%%%%%%%%%%%%%%%%%%%%%%%%%%%%%%%%%%%%%%%%%%%
    % To Evaluate NW
%%%%%%%%%%%%%%%%%%%%%%%%%%%%%%%%%%%%%%%%%%%%%%%%%%%%%%%%%%%%%%%%%%%%%%%%

    NW(i,j)=0.25*(OW(i+1,j)+OW(i-1,j)+OW(i,j+1)+OW(i,j-1))...
        -(h^2/(4*mue(i,j)))*dPmdzstar;

%%%%%%%%%%%%%%%%%%%%%%%%%%%%%%%%%%%%%%%%%%%%%%%%%%%%%%%%%%%%%%%%%%%%%%%%
    % To Evaluate NU
%%%%%%%%%%%%%%%%%%%%%%%%%%%%%%%%%%%%%%%%%%%%%%%%%%%%%%%%%%%%%%%%%%%%%%%%

A1=(2*mue(i,j)+kappa*mue(i,j))/(6*mue(i,j)+2*kappa*mue(i,j));
A2=mue(i,j)/(6*mue(i,j)+2*kappa*mue(i,j));

A3=(mue(i,j)+kappa*mue(i,j))/(4*(6*mue(i,j)+2*kappa*mue(i,j)));
NU(i,j)=A1*(OU(i+1,j)-OU(i-1,j))...
    +A2*(OU(i,j+1)-OU(i,j-1))...
    +A3*(OV(i+1,j+1)-OV(i+1,j-1)-OV(i-1,j+1)+OV(i-1,j-1));

```

```

%%%%%%%%%%%%%%%%%%%%%%%%%%%%%%%%%%%%%%%%%%%%%%%%%%%%%%%%%%%%%%%%%%%%%%%%
% To evaluate NV
%%%%%%%%%%%%%%%%%%%%%%%%%%%%%%%%%%%%%%%%%%%%%%%%%%%%%%%%%%%%%%%%%%%%%%%%
%
NV(i,j)=A1*(OV(i,j+1)-OV(i,j-1))...
+A2*(OV(i+1,j)-OV(i-1,j))...
+A3*(OU(i+1,j+1)+OU(i-1,j-1)-OU(i+1,j-1)-OU(i-1,j+1));
%

%%%%%%%%%%%%%%%%%%%%%%%%%%%%%%%%%%%%%%%%%%%%%%%%%%%%%%%%%%%%%%%%%%%%%%%%
% To find the differences between the new and old
velocities and the avarage error
%

%%%%%%%%%%%%%%%%%%%%%%%%%%%%%%%%%%%%%%%%%%%%%%%%%%%%%%%%%%%%%%%%%%%%%%%%
dW(i,j)=NW(i,j)-OW(i,j);
dU(i,j)=NU(i,j)-OU(i,j);
dV(i,j)=NV(i,j)-OV(i,j);
AW=dW(i,j); AU=dU(i,j); AV=dV(i,j);
if abs(AW)>=Minerror
    Error1(i,j)=abs(AW);
    OW(i,j)=OW(i,j)+SOR*dW(i,j); % instantaneous changing
for the old matrix values.
end
if abs(AU)>=Minerror
    Error2(i,j)=abs(AU);
    OU(i,j)=OU(i,j)+SOR*dU(i,j); % instantaneous changing
for the old matrix values.
end
if abs(AV)>=Minerror
    Error3(i,j)=abs(AV);
    OV(i,j)=OV(i,j)+SOR*dV(i,j); % instantaneous changing
for the old matrix values.
end
Aveerror1(i,j)=(Error1(i,j)+Error2(i,j)+Error3(i,j))/3;
end
end
Aveerror2=mean(Aveerror1);
Aveerror=mean(Aveerror2);
end
%
%%%%%%%%%%%%%%%%%%%%%%%%%%%%%%%%%%%%%%%%%%%%%%%%%%%%%%%%%%%%%%%%%%%%%%%%
% Defining dimensionless velocities at the walls for the new
velocities
%%%%%%%%%%%%%%%%%%%%%%%%%%%%%%%%%%%%%%%%%%%%%%%%%%%%%%%%%%%%%%%%%%%%%%%%
%
for j=2:Ny
    for i=2:Nx
        % For the W*.
        NW(1,j)=Wstar; % Left edge of the channel.
        NW(Nx+1,j)=Wstar; % Right edge of the channel.
        NW(i,1)=Wstar; % Bottom edge of the channel.
        NW(i,Ny+1)=0; % Top edge of the channel.
        NW(Nx+1,Ny+1)=0; % Top right corner.
        NW(1,Ny+1)=0; % Top Left corner.
        NW(1,1)=Wstar; % Bottom left corner.
        NW(Nx+1,1)=Wstar; % Bottom right corner.
    end
end

```



```

% For the U*
NU(1,j)=0; % Left edge of the channel.
NU(Nx+1,j)=0; % Right edge of the channel.
NU(i,1)=0; % Bottom edge of the channel.
NU(i,Ny+1)=0; % Top edge of the channel.
NU(Nx+1,Ny+1)=0; % Top right corner.
NU(1,Ny+1)=0; % To Left corner.
NU(1,1)=0; % Bottom left corner.
NU(Nx+1,1)=0; % Bottom right corner.
% For the V*
NV(1,j)=0; % Left edge of the channel.
NV(Nx+1,j)=0; % Right edge of the channel.
NV(i,1)=0; % Bottom edge of the channel.
NV(i,Ny+1)=0; % Top edge of the channel.
NV(Nx+1,Ny+1)=0; % Top right corner.
NV(1,Ny+1)=0; % To Left corner.
NV(1,1)=0; % Bottom left corner.
NV(Nx+1,1)=0; % Bottom right corner.
end
end
%
%%%%%%%%%%%%%%%%%%%%%%%%%%%%%%%%%%%%%%%%%%%%%%%%%%%%%%%%%%%%%%%%%%%%%%%%
% Finding the avarage dimensionless velocities
%%%%%%%%%%%%%%%%%%%%%%%%%%%%%%%%%%%%%%%%%%%%%%%%%%%%%%%%%%%%%%%%%%%%%%%%
%
Wlmean=mean(NW);
NWmeanstar=mean(Wlmean);
Ulmean=mean(NU);
NUmeanstar=mean(Ulmean);
Vlmean=mean(NV);
NVmeanstar=mean(Vlmean);
Averagevelocitystar=( (NWmeanstar^2)+(NUmeanstar^2)+(NVmeanstar^2) ) ^0.5
figure
surf(NW)
Averagevelocity=Averagevelocitystar*w0;
Flowrate=Averagevelocity*alpha*L^2*rho
iteration
Aveerror

```

المحاكاة الرقمية و التجارب العملية لمجال الجريان مع وجود جسيمات مُعلقة في مضخات منفردة دقيقة الأبعاد للاستخدامات البيو- طبية.

عزيز عبد الحافظ شاهين المحتسب

المشرف الرئيسي:

الدكتور أحمد السلايمة

المشرف المشارك:

الدكتور علاء الدين الحلولي

الملخص

تمثل هذه الدراسة محاكاة عددية تتم من خلالها اجراء مقارنة لعدة انواع من المضخات دقيقة الأبعاد (مضخات احادية القرص دقيقة الأبعاد, مضخات مزدوجة القرص دقيقة الأبعاد و مضخات ذات شكل حلزوني للقناة). حيث يتم اعتماد سائل غير نيوتوني (Non-Newtonian Fluid) و دراسة الاختلاف في الاداء بين هذا السائل و السائل النيوتوني (Newtonian Fluid) عند تغيير العديد من الظروف التشغيلية.

تم حل المسألة عن طريق الاشتقاق الرياضي و تبسيط المسألة بالاعتماد على عدة فرضيات تحدد الظروف التشغيلية للمضخات المتعددة مثل التشغيل في مرحلة الثبات الزمني (Steady state solution) و غيرها من الفرضيات. تم بعدها كتابة كودة خاصة بالمسألة باستخدام برنامج الماتلاب.

باستخدام برمجيات علوم ميكانيكا المواقع التي تم تطويرها مؤخرا، تم بناء أشكال ثلاثية الأبعاد تمثل مجال الجريان في المضخة وتم محاكاتها عدديا. للتعبير عن مختلف المتغيرات. تم التحقق من النتائج المستخلصة عن طريق مقارنة النتائج هذه مع الحل التحليلي للسائل النيوتوني. ومن ثم تمت دراسة عدة متغيرات و تمثيلها عن طريق الجداول استخدام هذه المؤثرات الشكلية في تعريف حلا نظريا يعبر عن تأثير هذه العوامل مشتراة وقد تم إثبات صحتها عدديا. تم إجراء تجارب عملية على مضختين حلزونيتين وفحصها وتركيبها في دائرة يمكن خلالها قياس كمية جريان السائل وضغطه. وجد فرق بين التجارب العملية و النظرية وذلك بسبب وجود تسرب للسائل بين حلقات المجرى الحلزوني بالإضافة إلى تغير حرارة السائل المستخدم أثناء عملية الفحص.